Applications of optical parametric downconversion: I. Self-phase locking; II. Generation of entangled photon pairs in periodically-poled lithium niobate

by

Elliott J. Mason, III

Submitted to the Department of Electrical Engineering and Computer Science
in partial fulfillment of the requirements for the degree of

Doctor of Philosophy in Electrical Engineering and Computer Science

at the

MASSACHUSETTS INSTITUTE OF TECHNOLOGY

June 2002

Author ....
Department of Electrical Engineering and Computer Science
May 17, 2002

Certified by... .....
Dr. Franco N. C. Wong
Principal Research Scientist
Thesis Supervisor

Accepted by .....
Arthur C. Smith
Chairman, Department Committee on Graduate Students

Applications of optical parametric downconversion: I. Self-phase locking; II. Generation of entangled photon pairs in periodically-poled lithium niobate

by

Elliott J. Mason, III

Submitted to the Department of Electrical Engineering and Computer Science
on May 17, 2002, in partial fulfillment of the
requirements for the degree of
Doctor of Philosophy in Electrical Engineering and Computer Science

Abstract

Nonlinear optics plays a key role in many applications not only as a means of frequency synthesis and control, but also as a source of twin photons and other nonclassical states of light. Advances in nonlinear materials, including engineered nonlinear interactions through the use of quasi-phase matching, have increased the flexibility and performance of many nonlinear optical devices. One of the devices presented in this thesis is a 2:1 frequency divider based on self-phase locking in a type-II phase matched optical parametric oscillator. This device is investigated both theoretically and experimentally. Results are also presented on fabrication of periodically-poled nonlinear crystals for quasi-phase matching in lithium niobate and barium magnesium fluoride. Finally, a high-efficiency frequency-nondegenerate twin photon source is implemented in periodically-poled lithium niobate.

Thesis Supervisor: Dr. Franco N. C. Wong
Title: Principal Research Scientist

Acknowledgments

I am grateful to my thesis supervisor Dr. Franco Wong for advising me and supporting me over the past eight years. His guidance and insight have been a valuable resource for me, and it has been a pleasure to work under his leadership. I have also been fortunate to have as members of my thesis committee Prof. Jeff Shapiro and Prof. Erich Ippen. I have learned much from both of them over the years.

I would also like to acknowledge the programs that have provided my financial support. I started my research with three years of support under a National Science Foundation Minority Graduate Fellowship. I have also obtained support from both the Army Research Office and the Air Force Office of Scientific Research through two DoD Multidisciplinary University Research Initiative (MURI) programs. Much of my work on electric-field poling was done with support from the M.I.T. Lincoln Laboratory Advanced Concept Program. I am grateful for the use of the Lincoln Laboratory facilities as well as the help and support from members of group 83: Skip Hoyt, Kevin Ray, Bob Bailey, Leo Missaggia, Chris Harris, Jeannie Porter, and from members of group 82: John Daneu, Scott Buchter, T. Y. Fan, and Antonio Sanchez.

I have also been supported by the fellow members of the Optical Communications group here at R.L.E. I want to express my heartfelt thanks to Marius Albota who put in many long nights with me in a cold lab looking for photon pairs. I want to thank Chris Kuklewicz for his valuable help with G programming for the poling and the data acquisition, and I want to thank Frieder Koenig who is continuing work on the photon pair generation experiment. I also appreciate the former members of our group that have given me support, friendship and advice over the years: Eser Keskiner, Phil Nee, Joe Teja, Reggie Brothers, and Dicky Lee.

As my stay at M.I.T. comes to a close I have to acknowledge my family who has been there for me showing me love and encouraging me every step of the way. My parents and grandparents have always kept me aware of their love and their prayers. My wife Jessica has constantly supported me and shown patience and understanding throughout unexpected turns and delays. Finally, God has kept me aware of his

constant presence and provision in all the details of my life and has renewed my strength each day.

Contents

1 Introduction **12**

1.1 Background 12

1.2 Parametric Downconversion 14

1.3 Applications and contributions of this research 16

1.4 Thesis organization 20

2 Self-phase locked optical parametric oscillator **21**

2.1 Theoretical analysis of a SPLOPO 22

2.1.1 Basic Equations 22

2.1.2 Tuning Behavior 27

2.2 Observation of two distinct phase states 35

3 Periodically-poled nonlinear materials **41**

3.1 Device fabrication 44

3.1.1 QPM grating design 44

3.1.2 Lithography and sample preparation 46

3.1.3 Electric-field poling 51

3.2 Periodically-poled $BaMgF_4$ for VUV generation 57

3.2.1 Material Properties 57

3.2.2 Periodic-poling of BMF 59

3.3 Application of PPLN to frequency-nondegenerate entanglement source 63

3.3.1 PPLN Characterization 64

3.3.2 Coincidence counting 70

4 Conclusion **76**

4.1 Summary 76

4.2 Future Work 77

A Grating Mask Specification and Generation **83**

A.1 Mask design parameters 83

A.2 AutoLisp Code 85

A.2.1 Mask specification files 86

A.2.2 Setup code library 90

A.2.3 Device drawing code library 95

A.2.4 Area calculation code library 101

A.2.5 Auxiliary code library 105

List of Figures

2-1 Plot of thresholds normalized to $\kappa_1\kappa_2/\chi^2$ over the locking range for no coupling ($\epsilon_0 = 0$), weak coupling ($\epsilon_0 = 0.3$), and strong coupling ($\epsilon_0 = 1$). The two threshold branches for the two coupled cases correspond to the higher-threshold (solid) and the lower-threshold (dashed) self-phase locked states. ϵ_0 is normalized to $\sqrt{\kappa_1\kappa_2}$ and $\sqrt{\Delta_1\Delta_2} = 0.4\sqrt{\kappa_1\kappa_2}$. 28

2-2 Plot of the minimum threshold $\left[(e_p^2)_{th}\right]_{min}$ normalized to $\kappa_1\kappa_2/\chi^2$ as a function of the normalized cavity detuning $\sqrt{\Delta_1\Delta_2/\kappa_1\kappa_2}$ for two different values of $\epsilon_0/\sqrt{\kappa_1\kappa_2}$: (a) 0.2, and (b) 0.5. 30

2-3 Contour plots of the total output powers for (a) the lower-threshold SPLOPO state and (b) the higher-threshold state under the condition of weak coupling $\epsilon_0/\sqrt{\kappa_1\kappa_2} = 0.3$. The output power is scaled by $\kappa_1\kappa_2/2\chi^2$. 32

2-4 Contour plots of the total output powers for (a) the lower-threshold SPLOPO state and (b) the higher-threshold state under the condition of strong coupling $\epsilon_0/\sqrt{\kappa_1\kappa_2} = 1$. The output power is scaled by $\kappa_1\kappa_2/2\chi^2$. 33

2-5 Plot of the signal-idler phase difference $\varphi_1 - \varphi_2$ as a function of the normalized cavity detunings for the two SPLOPO states. The range of one state is from 0 to π (top half) while the other state spans from 0 to $-\pi$ (bottom half). The two states have the same phase difference of 0 (heavy line A) and π (modulus 2π, heavy lines B) at the two ends of the locking range. $\epsilon_0/\sqrt{\kappa_1\kappa_2} = 0.5$ and $\theta = 0$. 34

2-6 Schematic of the experimental setup. SHG, second-harmonic generator; PZT, piezoelectric transducer. See text for other definitions. . . . 36

2-7 LO-signal interference under self-phase locked conditions ($\psi_q = 2°$, $\psi_h = 0°$) for (a) the p state, (b) the p state with a π phase shift in both ϕ_1 and ϕ_2, and (c) the n state. 38

2-8 Outputs at detectors D1 and D2 ($\psi_q = 1°$, $\psi_h = 103°$) for (a) p state and (b) n state. At $\psi_h = 103°$ the D1 interference of the p state was maximized. 39

3-1 Schematic of lithium niobate sample after preparation with deposited NiCr and insulating layers of fused silica and photoresist. Arrows indicate directions of domains after poling is completed. 51

3-2 The lithium niobate sample is shown here in the fixture which connects to the high voltage circuit. The chamber in the plexiglas is filled with liquid electrolyte that makes electrical contact between the circuit leads and the crystal surfaces. 52

3-3 Simplified circuit schematic for poling of PPLN device. V_{mon} and I_{mon} are voltage and current monitors which are fed back to control the total charge transfer. The high voltage amplifier has a gain $G = 2000$. The diode prevents back-flow of current. 53

3-4 Traces of the voltage and current monitors out of the Trek 20/20 high voltage amplifier. LabVIEW^{TM} is used to integrate the current and turn off the voltage when the total charge transferred reaches its target value. In this ideal case the current turns on and off sharply. 54

3-5 More traces of the voltage and current monitors out of the Trek 20/20 high voltage amplifier. In this case the poling current started early and stopped late due to uncertainty in the turn-on poling voltage. 55

3-6 Top (left panel) and bottom (right panel) etched surfaces of PPLN grating with a 22.4 μm period. The grating is only slightly over-poled with a 55% duty cycle. 56

3-7 Plots of the unpolarized optical transmission for two crystal lengths and the resulting inferred absorption coefficient. 58
3-8 Period of QPM grating needed to generate 157 nm with sum frequency generation. Plot versus shorter wavelength, for d_{33} (dashed) and d_{32} (solid). 60
3-9 Voltage and current of 19 pulses used to pole the BMF grating. . . . 61
3-10 Image of $+z$-face of periodically-poled BMF using an environmental scanning electron microscope. The grating period is 19.2 μm and the white scale bar corresponds to 50 μm. 62
3-11 Experimental setup for the DFG measurements taken to evaluate the poled crystals. A Si PIN photodiode and a lock-in amplifier was used to detect the generated light. The LP filter is a long-pass filter with cut-off frequency ~700 nm. 66
3-12 DFG conversion efficiency of the 3rd-order 22.1 μm period grating as a function of temperature with FWHM of 1.3°C. 68
3-13 DFG conversion efficiency of the 1st-order 7.5 μm period grating as a function of temperature with FWHM of 1.6°C. 69
3-14 Wavelength vs. temperature tuning curve for 21.6 μm period grating of PPLN. 70
3-15 DFG conversion efficiency of the 3rd-order 21.6 μm period grating of PPLN as a function of wavelength with FWHM of 1.26 nm. 71
3-16 Setup for coincidence counting of generated photon pairs. 72
3-17 Timing of conditional coincidence counting. 73
3-18 Conditional detection probability of idler photons given a signal photon is detected. Normalized histogram of counts in 2-ns time bins over a 20-ns window. 75

4-1 Dual coherently-pumped downconverter setup. The signal outputs are combined in one PBS and the idler outputs are combined in another PBS. Coincidence counting is performed as before, with HWPs and polarizers to project the outputs onto an arbitrary linear polarization basis. 78

4-2 Conditional coincidence counts normalized to give the probability of detecting an idler photon, given a signal photon has been detected. Plotted for various HWP angles from 0° to 90°. The maximum value at a HWP angle of 45° corresponds to rotation of the idler polarization by 90° such that the orthogonal state is detected. 79

A-1 Shown here are the definitions of the parameters specified when designing a QPM grating device with contact pads, and the corresponding device with contact pads only. 84

List of Tables

3.1 Measured DFG conversion efficiency and comparison with theory based on nominal value of $d_{33} = 27.2$ pm/V. Different focussing where reduction factors $h_m = 0.47$ (A) and $h_m = 0.08$ (B) were used. 67

Chapter 1

Introduction

1.1 Background

In a linear medium electromagnetic fields of different frequencies propagate without interacting with each other. Expressed in terms of input-output relations between electromagnetic fields, the total output can always be expressed as a linear combination of the individual output fields corresponding to different input frequencies. For any particular frequency the presence or absence of fields at other frequencies does not affect the evolution of the field. In optical materials the simplest (and strongest) form of nonlinearity is the second-order nonlinearity described by the second-rank nonlinear susceptibility tensor $\chi^{(2)}$. The lowest order nonlinearity in isotropic media such as glass is third-order since those of second-order only exists in media lacking inversion symmetry. There are many noncentrosymmetric crystals which possess a second-order nonlinearity by which an electric field induces a polarization proportional to the square of the field. This gives rise to an exchange of energy among fields of different frequencies, and is referred to as three-wave mixing.

The first known direct observations of the effects of the second-order nonlinearity are in the experiments of Pockels in 1893. One of the interacting fields was a static field giving rise to what is known as the electro-optic effect. The DC electric field strengths attainable were high enough to observe an induced birefringence experienced by an optical field propagating in the medium. Before this, experiments may have

been performed to attempt to observe optical nonlinearity as suggested by the words of Isaac Newton in his *Opticks* [1] in 1704: "when one sort of Ray hath been well parted from those of other kinds, it hath afterwards obstinately retained its colours, notwithstanding utmost endeavours to change it".

It was the discovery of the laser or the 'optical maser' [2] that was the key to enabling true nonlinear optical frequency mixing. The field of nonlinear optics has continued to flourish for most of over four decades since the demonstration of the first lasers. The first milestone was the observation of second harmonic generation by Franken *et al.* [3] in 1961. 694-nm light from a pulsed ruby laser was sent through a quartz crystal to generate 347-nm light. Closely following this was a demonstration of sum frequency generation [4]. These experiments suffered from the effects of dispersion which caused the interacting fields to have different phase velocities in the material, thus limiting the efficiency of the power transfer.

The importance of phase matching was pointed out independently by scientists from Bell Laboratories [5] and Ford Motor Company [6] who demonstrated that material birefringence could be used to cancel the effects of dispersion. This is known as birefringent phase matching. Another means of phase matching was suggested by Armstrong *et al.* [7] which involved compensating for the dispersion by periodically changing the sign of the nonlinear coefficient in the material to reset the relative phases after they have slipped 180 degrees out of phase. However, no practical means existed to accomplish this technique, now known as quasi-phase matching (QPM), so birefringent phase matching remained dominant for the following few decades. Over the years there have been improvements in the quality and availability of nonlinear materials and laser sources to extend the wavelength range of birefringent phase matching. There were also new techniques developed contributing to the advance of the field of nonlinear optics including Q-switching, optical parametric oscillation, and nonlinear interactions in waveguides. Nonlinear optics has been used for frequency converters, amplifiers, tunable sources, and important applications in fields such as frequency metrology and quantum optics.

In the mid-1990s QPM interactions began to be used in many experiments and de-

vices. Though QPM had been demonstrated before, the methods used had limitations that made it impractical. When electric field poling with a periodic metal electrode was demonstrated by Yamada, *et al.* [8] in 1993 many experiments followed that firmly established this method as a powerful technique for phase matching. Now, instead of finding a particular angle for a set of wavelengths that could be phase matched in a particular material, any wavelengths in the transparency range could be matched as long as a suitable electrode grating could be fabricated. Lithium niobate, already a widely available material used for its electro-optic and acousto-optic properties, became a popular material for QPM because of its high nonlinear coefficient and wide transparency range. Details of QPM and fabrication of periodically-poled lithium niobate (PPLN) are covered in chapter 3.

1.2 Parametric Downconversion

Energy conservation for any three-wave mixing interaction requires that the frequencies of the three interacting fields be related by

$$\omega_p = \omega_s + \omega_i \tag{1.1}$$

where the subscripts refer to the pump ('p'), signal ('s') and idler ('i') fields. These labels correspond to the process known as optical parametric amplification (OPA) where energy is transferred from a strong 'pump' field to amplify a weak 'signal' field. In addition to the requirement on the frequencies in (1.1), energy conservation also requires that energy will flow into a third 'idler' field. Equation (1.1) can also be interpreted according to the photon interactions by noting that every pump photon created (destroyed) requires that one signal and one idler photon be destroyed (created).

In an interaction where a new frequency is generated from fields at two input frequencies there are two standard three-wave mixing schemes. One is sum frequency generation (SFG) where fields at frequencies ω_s and ω_i mix to generate a field at a

higher frequency $\omega_p = \omega_s + \omega_i$. The other is difference frequency generation (DFG) where fields at frequencies ω_p and ω_s mix to generate a field at $\omega_i = \omega_p - \omega_s$. As explained above, this is also called optical parametric amplification when the process is used to amplify a weak input field at ω_s.

The two main applications demonstrated in this thesis make use of the process known as spontaneous parametric downconversion (SPDC). Unlike OPA, it only requires one input field. Classically, a single monochromatic input field does not undergo downconversion in a $\chi^{(2)}$. However, according to quantum theory, there is a nonzero probability that an 'input photon' at ω_p undergoes SPDC into two 'output photons' at ω_s and ω_i. This process is known as parametric fluorescence. Parametric amplification of single signal or idler 'noise' photons by a pump field is also known as parametric superfluorescence [9]. This type of interaction is useful for generating pairs of signal and idler photons that are entangled in energy and momentum. In this work we use SPDC in a PPLN crystal to achieve highly efficient, tunable, frequency-nondegenerate entangled photon pair generation.

When one or both of the downconverted fields are resonated in an optical cavity the parametric gain and optical feedback enable oscillation to occur. The parametric gain increases with pump power. The oscillation threshold occurs when the round trip gain and loss are equal. When pumped above threshold the SPDC seeds the conversion such that the circulating fields build up to a steady-state value. In steady state the gain remains clamped at this value and increased pump power above threshold increases the signal and idler outputs. This is known as an optical parametric oscillator (OPO). When only one field is resonated in a singly-resonant OPO (SRO) the frequency with the largest gain and smallest loss, such that the oscillation condition is met, determines the signal and idler frequencies within the broad phase-matching bandwidth. There exists such a frequency for every cavity length. A doubly-resonant OPO (DRO) requires both fields to be resonant which places an extra constraint on the frequencies such that it only oscillates in a discrete set of longitudinal cavity modes. Both SROs and DROs have been used extensively as sources of continuous-wave (cw) or pulsed light. They enable high-power frequency conversion and expand

the ranges of frequency, power, and tunability that can be achieved over conventional laser sources. In this work we demonstrate a new application of an OPO: a 2:1 frequency divider based on a self-phase-locked cw DRO.

1.3 Applications and contributions of this research

CW OPOs have properties which make them useful sources of light for a wide range of applications. They have played important roles as tunable sources for high-resolution spectroscopy, and as fixed stable sources for precision measurements and optical frequency metrology. Progress in nonlinear materials (including periodically-poled crystals), and stable solid-state pump lasers have contributed to the interest in cw OPOs as practical tools. Tunability over broad operating ranges of tens to hundreds of nm have been achieved with techniques such as the use of broadband high-reflection mirrors [10] and novel grating designs [11]. For spectroscopy OPOs can provide substantial amounts of power, with narrow linewidths and large continuous (mode-hop-free) tunability. Continuous tuning of both SROs and DROs have been demonstrated. An implementation of molecular spectroscopy was demonstrated using a pump-resonant SRO [12] with a tuning range of over 1 GHz. Due to their discrete longitudinal cavity modes, DROs require a servo to lock onto a single cavity mode. Nevertheless, continuous tuning in DROs has also been demonstrated using pump tuning (over a range of 8 GHz) [13], or using a dual-cavity design (over a range of 900 MHz) [14].

In some situations it is desirable to remove this degree of tunability freedom and fix the output frequencies. For example, the subharmonics of an OPO can be tuned and locked to precisely known ratios of the pump frequency. Such devices are known as optical frequency dividers [15, 16]. Used in conjunction with optical frequency comb generators they played an important role in optical frequency metrology in the implementation of optical-to-microwave frequency chains [17]. More recently, the role of optical frequency dividers has been dramatically reduced by breakthroughs that utilized octave-spanning optical frequency combs generated from modelocked lasers [18, 19]. They can still provide an important function of precisely dividing an

input frequency by two or some other predetermined ratios.

Graham and Haken first investigated the quantum noise characteristics of OPOs. They showed that the sum of the signal and idler phases follows the phase of the pump, and the difference of the signal and idler phases undergoes a phase diffusion process from interaction of the signal and idler modes with vacuum fluctuations [20]. Thus, in order to achieve phase-coherent frequency division the signal and idler waves must be phase locked. One method used to achieve a stable phase locked output is by means of an external phase-locked loop [21]. This method is limited by the electronic servo bandwidth. An alternative method is an internal all-optical method: self-phase locking. This was first observed in a 2:1 frequency divider based on a type-I phase matched DRO [22]. When tuned to frequency degeneracy the co-polarized signal and idler experience strong mutual coupling and they become phase locked to the pump with either a zero or π relative phase. In contrast, the signal and idler fields in a type-II phase matched DRO are orthogonally polarized and can be smoothly tuned through frequency degeneracy with no locking occurring. In this thesis I show that it is possible to obtain self-phase locking in a type-II phase-matched DRO and that its characteristics are very different from that of a type-I phase-matched DRO. By inserting an intracavity waveplate to rotate and thereby couple the orthogonally polarized fields self-phase locking occurs at frequency degeneracy [23]. A theoretical analysis [24] of this device shows that this mutual signal-idler coupling leads to two steady-state oscillation modes, both of which we observed experimentally. This thesis covers both the theoretical analysis and the experimental demonstration of the self-phase locked type-II phase matched DRO.

Based on the results of our work, Lee *et al.* demonstrated self-phase locking in a 3:1 frequency divider based on a type-I phase matched DRO through the use of nonlinear signal-idler coupling [25]. A dual grating PPLN crystal was used to provide one grating section for the downconverter and a second grating section to phase match mixing between the signal and idler which were in a 2:1 ratio. Theoretical analysis of this type of device has also been done investigating the resonant $\chi^{(2)} : \chi^{(2)}$ cascaded second order nonlinearity and the resulting self-phase locking behavior [26].

Quantum optics is another area where cw OPOs have played an important role as nonclassical light sources. Many experiments have been performed demonstrating squeezing when pumped below threshold (as a cavity-enhanced OPA), and sources of intensity-correlated twin-beams when pumped above threshold. It was a correlation measurement using a cw OPO that provided the first experimental demonstration [27] of the original Einstein-Podolsky-Rosen paradox utilizing continuous quantum variables where quadrature-phase amplitudes played the role of the canonical position and momentum variables. The European Union has a consortium [28] of universities in Germany, France, UK, and Denmark focusing on the use of continuous quantum variables in quantum communications. A primary goal is quantum teleportation of continuous quantum variables using various sources of "bright quantum light." One of the sources utilizes the same configuration as the type-II self-phase locked OPO first demonstrated in this work. They propose "...to operate a type II OPA in the frequency degenerate regime by injecting it with an external field, or by 'self injection' (coupling of the two orthogonally polarised fields inside the cavity). By separating of the two outgoing polarisations, one expects to produce beams with entangled quadrature phase amplitudes."

A large area of research is devoted to sources of entangled pairs of photons produced via SPDC in a nonlinear crystal. Entangled photon pairs are a key element in many systems that rely on quantum information. The goals of such systems are implementation of quantum communications, quantum computational algorithms, or quantum cryptography. Many particular applications such as teleportation [29] make use of polarization-entangled photons. One of the main goals of many experiments is to demonstrate practical "bright" entangled sources with a high pair production rate [30]. One way to boost the production rate is to place the crystal in a cavity for the pump field, thus increasing the efficiency of the SPDC [31].

One recently proposed quantum communication system [32] aims to achieve long-distance high-fidelity teleportation making use of polarization-entangled photons and trapped-atom quantum memories [33]. The polarization state of the photons can be transferred to the long-lived hyperfine levels of ultra-cold trapped rubidium atoms.

This system allows for quantum information in the form of qubits to be transmitted reliably and stored for later processing. A novel ultrabright narrowband source of polarization-entangled photons is proposed [34] to achieve efficient coupling of photons into the optical cavity containing the atom which has a $\sim$6 MHz bandwidth at a 795 nm center wavelength. This source produces narrowband polarization-entangled photon pairs using a doubly resonant optical cavity for signal and idler. Pumped well below threshold, the OPA produces a high flux of photon pairs over the bandwidth defined by the OPA cavity that is designed to match the trapped-atom memory. A single OPA would produce signal and idler outputs correlated in polarization, but not in a polarization-entangled state. Two such OPAs can be combined in such a way that each of the signal and idler outputs is in a superposition state of two orthogonal polarizations coming from the two OPAs. Such a scheme does not require that the signal and idler be frequency degenerate as do many typical downconverter sources. In the proposed system this feature is utilized to make the signal match the 795 nm excitation wavelength of a local trapped-Rb quantum memory, and the idler at $\sim$1600 nm for low loss fiber optic transmission to a remote location. The first step towards such a source is implemented in this thesis using PPLN pumped by a 532 nm pump to generate photons at 795 nm and 1609 nm. The benefits of PPLN in providing a flexible and efficient means to generate entangled photon pairs is beginning to be recognized [35, 36]. We demonstrate efficient generation and collection of photon pairs into single-mode fibers by time-coincident counting of the signal and idler photons.

Another application demonstrated in this thesis was also made possible by electric-field poling of ferroelectric crystals. Conventional materials for generation of wavelengths in the UV and vacuum UV spectral regions suffer from limitations such as solarization, large Poynting-vector walk-off, and limited vacuum-UV transparency. One material, barium magnesium fluoride (BMF), not only has excellent transparency down to $<$140 nm, but is also resistant to solarization. However, the birefringence is not strong enough to birefringently phase match interactions for generating wavelengths this short. We have shown that it is possible to use electric-field poling to enable QPM in this material [37]. This also eliminates Poynting-vector walk-off since

QPM utilizes noncritical phase matching. We also use an environmental scanning electron microscope to examine the quality of the domain reversal and find that high-fidelity patterning of a 19.2-mm-period grating is possible, an important step for showing feasibility of obtaining shorter period gratings.

1.4 Thesis organization

This thesis demonstrates devices based on optical parametric downconversion and developments made in periodic poling of ferroelectric crystals. Chapter (2) introduces and describes the self-phase locked OPO. It starts with a theoretical analysis and illustrations of some basic properties of the device in section (2.1). Then in section (2.2) the observations made from an experimental realization of the device are presented. Chapter (3) covers periodic poling in two nonlinear crystals, lithium niobate and BMF, and the advantages they bring to particular applications. A detailed description of all the steps involved in fabricating PPLN is contained in section (3.1). Section (3.2) then covers the first-time demonstration of periodic poling in the material BMF enabling UV generation through QPM. Then the use of PPLN for as a high-efficiency source of frequency-nondegenerate photon pairs is discussed in section (3.3) with a demonstration of nonclassical time correlations through coincidence counting. The thesis concludes in chapter (4) with a summary of the main results and a discussion of future directions for work on the photon pair source.

Chapter 2

Self-phase locked optical parametric oscillator

Self-phase locking is a means of achieving a mutually phase-locked (and frequency degenerate) signal and idler output in a type-II phase-matched doubly-resonant OPO without the need for an external phase-locked loop [21]. By inserting an intracavity quarter-wave plate (QWP) a linear coupling between the orthogonally polarized signal and idler fields allows a form of mutual injection locking at exact frequency degeneracy. Two self-phase locked modes with different thresholds and signal-idler phases are possible. This is illustrated here both theoretically and experimentally along with other properties of this device [24, 23].

A detailed theoretical model of the steady-state characteristics of the self-phase locked OPO is covered in section (2.1). Section (2.2) describes the experimental observations of self-phase locking in a type-II phase-matched KTP OPO. We observed two distinct phase states that differed by nearly π in their signal-idler phase difference. Attention is focussed on how these two states were identified. These observation prompted the analysis of section (2.1).

2.1 Theoretical analysis of a SPLOPO

In section 2.1.1 the basic equations of both the normal, uncoupled OPO and the self-phase locked OPO are introduced and solved. As a first step, and in order to introduce the relevant notations and equations, we consider a nondegenerate, doubly resonant OPO (DRO) without an intracavity waveplate. In a DRO the signal and idler fields are resonated in a cavity which contains the nonlinear crystal. Since we are covering self-phase locking phenomenon under type-II phase matching, we will assume a crystal that is phase matched for orthogonal signal and idler polarizations (set by the ordinary and extraordinary crystal axes) given by unit vectors $\vec{i_1}$ and $\vec{i_2}$ for signal and idler, respectively. We then modify the equations introducing an intracavity QWP for self-phase locking. The orientation of the fast and slow axes of the QWP are defined according to the angle ψ_q between the QWP's fast axis and the fixed direction $\vec{i_2}$. In section 2.1.2 numerical results are plotted to illustrate the regimes of operation for various values of the free parameters.

2.1.1 Basic Equations

The DRO converts a pump field of frequency ω_p into signal and idler fields of frequencies ω_1 and ω_2, respectively. Energy conservation yields the relationship among the frequencies $\omega_p = \omega_1 + \omega_2$. Furthermore, the interaction is assumed to be phase matched such that $k_p = k_1 + k_2$. Let A_p, A_1, A_2 be the complex amplitudes of these three fields, normalized in such a way that $|A_i|^2$ $(i = p, 1, 2)$ gives the corresponding photon flux in units of photons/second.

The pump is assumed to be nonresonant and takes a single pass through the crystal. The signal and idler modes are allowed to have some nonzero detuning from the nearest cavity resonance denoted by Δ_i $(i = 1, 2)$, where

$$\Delta_i = \frac{\omega_i}{c} L(\omega_i) - 2\pi p_i. \tag{2.1}$$

The parameter p_i is an integer representing a particular longitudinal cavity mode, and

$L(\omega_i)$ is the cavity roundtrip optical length at frequency ω_i, which can be experimentally changed either by moving one mirror of the cavity or by changing the crystal temperature and therefore its index of refraction. The double resonance condition implies that $\Delta_1 \ll 1$ and $\Delta_2 \ll 1$, i.e., the output fields are near cavity resonance and within a cavity linewidth of the resonance peaks.

When the DRO is in the steady-state regime the roundtrip gain and losses experienced by the resonant fields are equal and small. The fields can therefore be approximated as varying linearly over the length of the crystal: the signal and idler fields increase and the pump decreases linearly over the length of the crystal. The circulating fields A_s and A_i are approximately constant inside the cavity. The nonresonant pump can be depleted by a significant amount. However, as shown below, the magnitude of A_p, defined here as the mid-crystal pump field amplitude, is clamped at its threshold value even at full depletion [38].

By requiring in steady-state that the field amplitude is unchanged after one round trip in the cavity, one obtains the following well-known classical equations for the three fields:

$$(\kappa_1 - i\Delta_1)A_1 = \chi A_p A_1^*, \tag{2.2}$$

$$(\kappa_2 - i\Delta_2)A_2 = \chi A_p A_1^*, \tag{2.3}$$

$$A_p = e_p - \frac{1}{2}\chi A_1 A_2, \tag{2.4}$$

where χ is the normalized crystal nonlinearity (taken real, because the crystal is assumed to be lossless and exactly phase matched), e_p (its phase set to zero) is the pump amplitude at the input of the crystal, and κ_i (with $\kappa_i \ll 1$) is the roundtrip cavity field loss coefficient. The pump is assumed to make a single pass through the crystal and the cavity losses are lumped together and assigned to a single output coupling mirror with power reflection coefficient R_i $(i = 1, 2)$ given by $R_i = (1 - \kappa_i)^2$.

It is well-known that these equations have a nonzero solution only when

$$\frac{\Delta_1}{\Delta_2} = \frac{\kappa_1}{\kappa_2}, \tag{2.5}$$

which, with the help of Eq. (2.1), sets a well-defined value to the signal and idler frequencies for a given longitudinal mode number p_i. Expressing the complex field amplitudes in terms of the real-valued amplitudes and phases $A_i = r_i e^{i\varphi_i}$, the following relations hold

$$\chi^2 r_p^2 = \kappa_1\kappa_2 + \Delta_1\Delta_2, \tag{2.6}$$

$$\left(\frac{r_1}{r_2}\right)^2 = \frac{\Delta_2}{\Delta_1}, \tag{2.7}$$

$$\varphi_1 + \varphi_2 = \varphi_p + \tan^{-1}\left(\frac{\Delta_1}{\kappa_1}\right). \tag{2.8}$$

The mid-crystal pump power is independent of the pump input power e_p^2. The ratio of the signal and idler circulating powers is determined by the ratio of their detunings (which is the same as the ratio of their losses). The sum of the signal and idler phases is fixed relative to the pump phase. However, their difference is undetermined and undergoes a phase diffusion process [20, 39].

The oscillation threshold occurs when the input pump power is equal to the value given by Eq. (2.6):

$$(e_p^2)_{th} = r_p^2 = \frac{1}{\chi^2}(\kappa_1\kappa_2 + \Delta_1\Delta_2). \tag{2.9}$$

Above threshold, the photon flux transmitted through the output coupler (including the loss associated with it) is given by $P_i = 2\kappa_i r_i^2$ $(i = 1, 2)$. As expected, the total photon flux for the signal and idler are equal: $P_1 = P_2$. The total output power can also be expressed in terms of the input pump power and other cavity parameters

$$P_{out} = P_1 + P_2 = 2\kappa_1 r_1^2 + 2\kappa_2 r_2^2 \tag{2.10}$$

$$= 8e_{p0}^2\left[\sqrt{F_p - (\Delta_1/\kappa_1)^2} - 1\right], \tag{2.11}$$

where $F_p = e_p^2/e_{p0}^2$ is the number of times the DRO is pumped above the zero-detuned threshold $e_{p0}^2 = \kappa_1\kappa_2/\chi^2$. The circulating signal and idler powers that determine the

output powers P_1 and P_2 are related to P_{out} by the following expressions

$$r_1^2 = \frac{\Delta_2}{\kappa_1\Delta_2 + \kappa_2\Delta_1}\frac{P_{out}}{2}, \tag{2.12}$$

$$r_2^2 = \frac{\Delta_1}{\kappa_1\Delta_2 + \kappa_2\Delta_1}\frac{P_{out}}{2}. \tag{2.13}$$

For the self-phase locked OPO, we now modify the equations for the usual DRO by inserting a linear coupling term between the signal and idler fields. Experimentally this can be easily achieved in a type-II phase-matched DRO with an intracavity QWP in a standing-wave cavity configuration. A double pass through the QWP is equivalent to a single pass through a half-wave plate, rotating each field by twice the angle ψ_1 between the wave plate and the crystal axes. The equations for the projections of the fields on the ordinary and extraordinary crystal axes are now

$$(\kappa_1 - i\Delta_1)A_1 = \chi A_p A_1^* + \epsilon A_2 e^{i(\omega_1-\omega_2)t}, \tag{2.14}$$

$$(\kappa_2 - i\Delta_2)A_2 = \chi A_p A_1^* - \epsilon^* A_1 e^{-i(\omega_1-\omega_2)t}, \tag{2.15}$$

where ϵ is the mutual-injection coupling constant due to the QWP. As required by energy conservation, the injection coupling constant in Eq. (2.15) is the negative complex conjugate of that in Eq. (2.14). Writing $\epsilon = \epsilon_0 \exp(i\theta)$, we have $\epsilon_0 \propto \sin 2\psi_q$. The coupling strength ϵ_0 also depends on mode matching and Poynting-vector walk-off. θ is the roundtrip phase shift between the signal and the injected idler.

This DRO has a frequency degenerate regime with time independent values for A_1 and A_2 with the condition $\omega_1 - \omega_2 = 0$, i.e., $\omega_1 = \omega_2 = \omega_p/2$. This corresponds to the *self-phase locked OPO* (SPLOPO), working at exact frequency degeneracy, where the coupling between the two oscillating fields leads to mutual frequency locking. Experimentally this regime is entered when the signal-idler frequency difference is tuned to within the capture range that depends on the coupling strength as in laser injection locking. The theoretical analysis here covers only the steady-state solutions

within this regime where Eqs. (2.14) and (2.15) take the simplified form

$$(\kappa_1 - i\Delta_1)A_1 = \chi A_p A_1^* + \epsilon A_2, \tag{2.16}$$

$$(\kappa_2 - i\Delta_2)A_2 = \chi A_p A_1^* - \epsilon^* A_1. \tag{2.17}$$

This set of equations has a nontrivial solution ($A_1 \neq 0, A_2 \neq 0$) when its determinant is zero. This leads to the following equation that is necessary for the self-phase locked operation

$$(\chi^2 r_p^2 - \kappa_1\kappa_2 - \Delta_1\Delta_2 - \epsilon_0^2)^2 + (\kappa_1\Delta_2 - \kappa_2\Delta_1)^2 = 4\epsilon_0^2\Delta_1\Delta_2.$$

This equation has real solutions for the pump field amplitude r_p if and only if

$$4\epsilon_0^2\Delta_1\Delta_2 \geq (\kappa_1\Delta_2 - \kappa_2\Delta_1)^2. \tag{2.18}$$

As Δ_1 and Δ_2 can be tuned by changing external parameters, such as the cavity length or the crystal temperature, condition (2.18) defines an operating range for these parameters within which the locking phenomenon takes place. The oscillation threshold is still defined as the clamped mid-crystal pump power: $(e_p^2)_{th} = r_p^2$. However, there are now two solutions for r_p^2. When condition (2.18) is satisfied the SPLOPO may oscillate in one of two locked modes, each with a different threshold given by

$$\chi^2 r_p^2 = \kappa_1\kappa_2 + \Delta_1\Delta_2 + \epsilon_0^2 \pm \sqrt{4\epsilon_0^2\Delta_1\Delta_2 - (\kappa_1\Delta_2 - \kappa_2\Delta_1)^2}. \tag{2.19}$$

The ratio of the signal and idler circulating powers is still given by the ratio of their detunings as in Eq. (2.7). However, now this ratio is no longer equal to the ratio of their losses, but can vary over the *locking range* determined by condition (2.18).

The signal and idler sum and difference phases are given in the following equations

$$\varphi_1 + \varphi_2 = \varphi_p \pm \cos^{-1}\left[\frac{1}{2\chi r_p}\left(\kappa_1\sqrt{\frac{\Delta_2}{\Delta_1}} + \kappa_2\sqrt{\frac{\Delta_1}{\Delta_2}}\right)\right], \tag{2.20}$$

$$\varphi_1 - \varphi_2 \;=\; \theta \pm \cos^{-1}\left[\frac{1}{2\epsilon_0}\left(\kappa_1\sqrt{\frac{\Delta_2}{\Delta_1}} - \kappa_2\sqrt{\frac{\Delta_1}{\Delta_2}}\right)\right], \tag{2.21}$$

where the $\pm$ signs depend on the sign of Δ_1 and on the oscillation mode. The sine of both $\varphi_1 + \varphi_2 - \varphi_p$ and $\varphi_1 - \varphi_2 - \theta$ can also be obtained from Eqs. (2.16) that can uniquely determine the signs in Eqs. (2.20) and (2.21) which clearly show that the phases φ_1 and φ_2 are uniquely determined by the various operating parameters, and hence are both locked to well defined values that are related to the mid-crystal pump phase φ_p. Unlike the conventional OPO in which the signal-idler phase difference undergoes phase diffusion, the SPLOPO has a fixed phase difference and fixed signal and idler phases. Note that these phases take on different values in the two possible oscillation modes.

The total output power P_{out} as defined by (2.10) can be shown to be a solution of the following equation

$$\begin{aligned} 0 \;=\; & \frac{\chi^4 P_{out}^2}{16(\kappa_1^2\Delta_2/\Delta_1 + 2\kappa_1\kappa_2 + \kappa_2^2\Delta_1/\Delta_2)} + \frac{\chi^2 P_{out}}{4} \\ & + (\kappa_1\kappa_2 + \Delta_1\Delta_2 + \epsilon_0^2 \pm \sqrt{4\epsilon_0^2\Delta_1\Delta_2 - (\kappa_1\Delta_2 - \kappa_2\Delta_1)^2}) - \chi^2 e_p^2. \end{aligned} \tag{2.22}$$

The signal and idler amplitudes are still related to the total output power by Eqs. (2.12). Above threshold, there is only one positive solution for P_{out} in Eq. (2.22) for each oscillation mode.

2.1.2 Tuning Behavior

Based on the above solutions we now investigate the tuning characteristics of the SPLOPO. The linear coupling strength ϵ_0 is an adjustable parameter that is expected to have a significant effect on the SPLOPO tuning behavior. Physically ϵ_0 is determined by the amount of polarization rotation due to the intracavity waveplate as described above. When we speak of tuning we do not mean the tuning of the output frequencies, which are fixed at $\omega_p/2$ in the self-phase locked regime. Instead, the tunings that we are interested in are those of Δ_1 and Δ_2 which can be adjusted

by varying the crystal temperature, the physical length of the cavity, or even the separate beam paths inside the cavity (due to walk-off). Changes in Δ_1 and Δ_2 within the locking range affect the thresholds, the output powers, and the signal and idler phases.

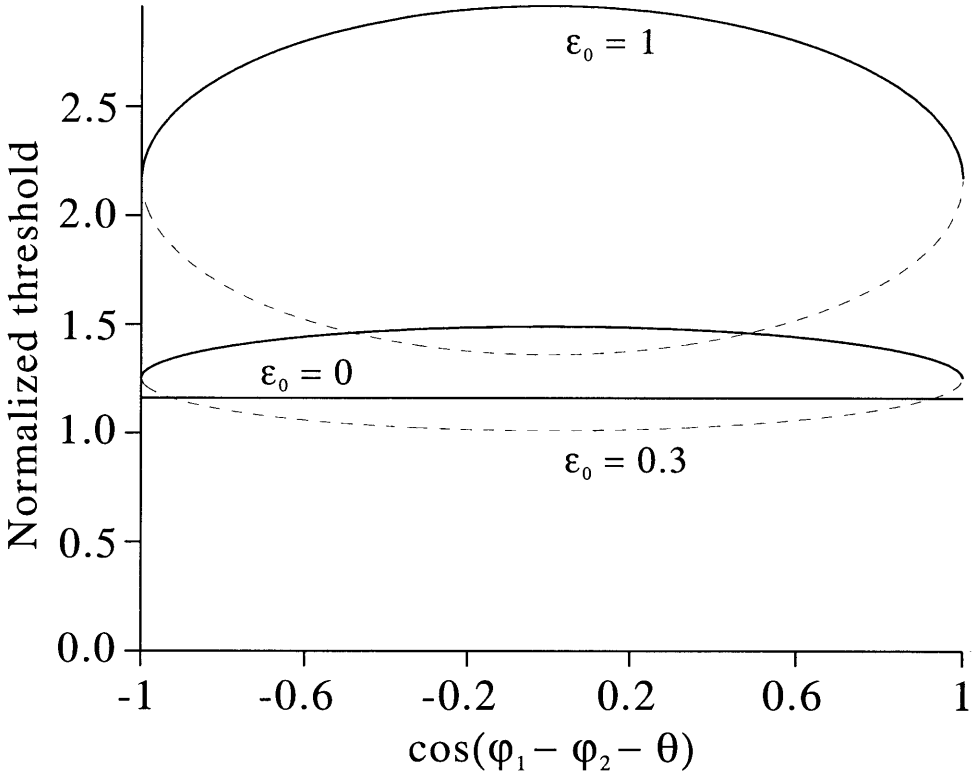

Figure 2-1: Plot of thresholds normalized to $\kappa_1\kappa_2/\chi^2$ over the locking range for no coupling ($\epsilon_0 = 0$), weak coupling ($\epsilon_0 = 0.3$), and strong coupling ($\epsilon_0 = 1$). The two threshold branches for the two coupled cases correspond to the higher-threshold (solid) and the lower-threshold (dashed) self-phase locked states. ϵ_0 is normalized to $\sqrt{\kappa_1\kappa_2}$ and $\sqrt{\Delta_1\Delta_2} = 0.4\sqrt{\kappa_1\kappa_2}$.

From the threshold Eq. (2.19) it is clear that the geometric mean of the roundtrip cavity losses $\sqrt{\kappa_1\kappa_2}$ serves as the normalization factor to which other parameters should be compared. Figure (2-1) shows the threshold power $(e_p^2)_{th}$ over the locking range for the two SPLOPO states for weak coupling with $\epsilon_0/\sqrt{\kappa_1\kappa_2} = 0.3$ (or $\epsilon_0^2/(\kappa_1\kappa_2) \approx 0.1$) and for strong coupling with $\epsilon_0/\sqrt{\kappa_1\kappa_2} = 1$. The locking range

defined by condition (2.18) can be rewritten as

$$1 \geq |\frac{1}{2\epsilon_0}(\kappa_1\sqrt{\frac{\Delta_2}{\Delta_1}} - \kappa_2\sqrt{\frac{\Delta_1}{\Delta_2}})| = |\cos(\varphi_1 - \varphi_2 - \theta)|. \tag{2.23}$$

It is therefore appropriate to represent the locking range axis in Fig. (2-1) by $-1 \leq \cos(\varphi_1 - \varphi_2 - \theta) \leq 1$. We note that the locking range condition constrains only the ratio Δ_1/Δ_2 and, in order to completely specify the operating conditions for Fig. (2-1), we set the geometric mean of the cavity detunings $\sqrt{\Delta_1\Delta_2} = 0.4\sqrt{\kappa_1\kappa_2}$. For reference, the straight line in Fig. (2-1) represents the threshold for the uncoupled case ($\epsilon_0 = 0$) given by Eq. (2.9). There are two oscillation threshold branches for each coupling case corresponding to the two states of the SPLOPO. At the center of the locking range, where $\kappa_1/\Delta_1 = \kappa_2/\Delta_2$, the threshold difference between the two branches is maximum and equals $4\epsilon_0\sqrt{\Delta_1\Delta_2}$. As a result, this threshold difference is much more pronounced for the case of strong coupling. We note that in Fig. (2-1) the minimum threshold for the weak coupling case ($\epsilon_0/\sqrt{\kappa_1\kappa_2} = 0.3$) is actually lower than the uncoupled case ($\epsilon_0 = 0$).

In general the threshold is higher for a larger ϵ_0. However, near the center of the locking range it is possible for the strong-coupling threshold to be lower than the weak-coupling threshold. At the center of the locking range the threshold difference between the two oscillation modes is maximum. In this case the lower threshold is

$$\left[(e_p^2)_{th}\right]_{min} = \frac{1}{\chi^2}(\kappa_1\kappa_2 + (\sqrt{\Delta_1\Delta_2} - \epsilon_0)^2). \tag{2.24}$$

We see that for a given coupling strength the minimum threshold at the center of the locking range depends on the detuning. For a given pair of signal and idler detunings, this minimum threshold is reduced with respect to the uncoupled case if $4\Delta_1\Delta_2 > \epsilon_0^2$. We note that the minimum threshold in the SPLOPO is always above or equal to the minimum threshold for the uncoupled case at zero detuning ($\Delta_1 = \Delta_2 = 0$) which is $\kappa_1\kappa_2/\chi^2$.

Figure (2-2) plots the minimum threshold $\left[(e_p^2)_{th}\right]_{min}$ as a function of $\sqrt{\Delta_1\Delta_2}$ for

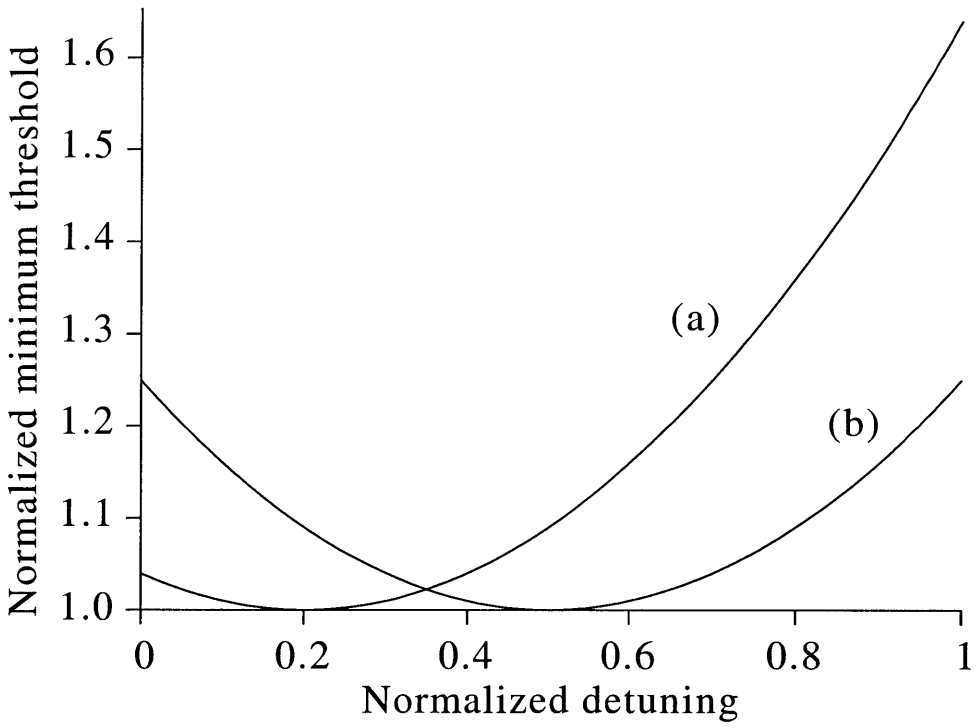

Figure 2-2: Plot of the minimum threshold $\left[(e_p^2)_{th}\right]_{min}$ normalized to $\kappa_1\kappa_2/\chi^2$ as a function of the normalized cavity detuning $\sqrt{\Delta_1\Delta_2/\kappa_1\kappa_2}$ for two different values of $\epsilon_0/\sqrt{\kappa_1\kappa_2}$: (a) 0.2, and (b) 0.5.

two different values of $\epsilon_0/\sqrt{\kappa_1\kappa_2} = 0.2, 0.5$. The two curves look identical except for a displacement along the cavity detuning axis, as Eq. (2.24) clearly indicates. The threshold reaches the minimum of unity (normalized to $\kappa_1\kappa_2/\chi^2$) at $\sqrt{\Delta_1\Delta_2} = \epsilon_0$. It illustrates that for a given coupling ϵ_0 the minimum threshold can be obtained with adequate cavity detuning and that this minimum threshold does not occur at zero detuning, as is the case for the uncoupled OPO.

While it is useful to plot the threshold values over the locking range it is perhaps more intuitive to study the tuning behavior as a function of the individual cavity detunings Δ_1 and Δ_2. Figure (2-3) shows contour plots of the total output power P_{out} of Eq. (2.22) of the (a) lower-threshold and (b) higher-threshold SPLOPO states as a function of the normalized cavity detunings, Δ_1/κ_1 and Δ_2/κ_2, for weak coupling ($\epsilon_0/\sqrt{\kappa_1\kappa_2} = 0.3$) and for pumping at 2.5× above the minimum threshold, or $e_p^2 =$

$2.5(\kappa_1\kappa_2/\chi^2)$. The area within the two straight lines is within the locking range and the shaded areas denote above-threshold operation. The contour lines are scaled by $\kappa_1\kappa_2/2\chi^2$ and the higher output power is in darker shades. For this weak coupling case the operating regions and the output power levels for the two SPLOPO states are quite similar, which is expected because the linear coupling term which lifts the degeneracy of the two states is small. One apparent difference in Fig. (2-3) is the convex curvature of the contour lines for (a) the lower-threshold output power, and the concave curvature for (b) the higher-threshold output power, when viewed toward the origin.

For strong coupling $\epsilon_0/\sqrt{\kappa_1\kappa_2} = 1$, Fig. (2-4) shows that the two SPLOPO states have very different operating regions and output powers for pumping at $2.5\times$ above the minimum threshold. The lower-threshold state (a) in Fig. (2-4) has a much broader operating region in the Δ_1, Δ_2 space than that for the weak coupling case Fig. (2-3(a)). The operating space of the higher-threshold state (b) in Fig. (2-4) is confined to a much smaller area because the strong coupling makes the threshold significantly higher in most regions. In addition, the output powers of the high-threshold state in Fig. (2-4(b)) are significantly lower than that of the lower-threshold state in Fig. (2-4(a)). Note that the convex-concave features of the contour lines remain in the strong coupling regime.

The signal-idler phase difference $\varphi_1 - \varphi_2$ of the self-phase locked OPO determines the polarization of the output. This phase difference ranges from 0 to π for one mode and from 0 to $-\pi$ for the other oscillation mode (for $\theta = 0$). The exact phase-difference angle depends on the operating point within the locking range. Therefore the output polarization can be manipulated by changing the operating point of the OPO. Figure (2-5) shows the signal-idler phase difference (θ is set to zero for convenience) for the two SPLOPO states as a function of the normalized cavity detunings. We assume moderate coupling of $\epsilon_0/\sqrt{\kappa_1\kappa_2} = 0.5$ for Fig. (2-5). We note that near the center of the locking range the *difference* in the relative phase difference $\varphi_1 - \varphi_2$ between the two oscillation modes is a maximum of π.

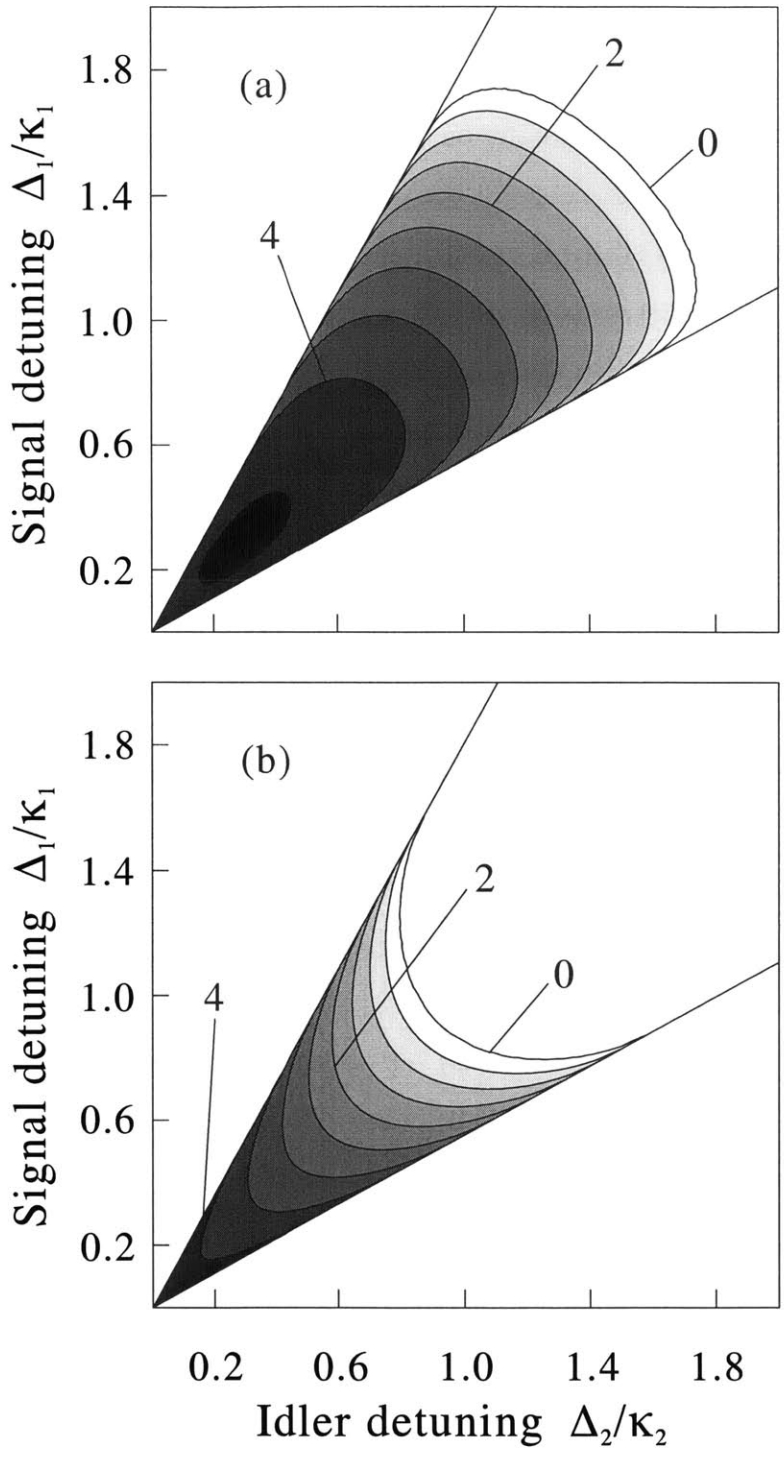

Figure 2-3: Contour plots of the total output powers for (a) the lower-threshold SPLOPO state and (b) the higher-threshold state under the condition of weak coupling $\epsilon_0/\sqrt{\kappa_1\kappa_2} = 0.3$. The output power is scaled by $\kappa_1\kappa_2/2\chi^2$.

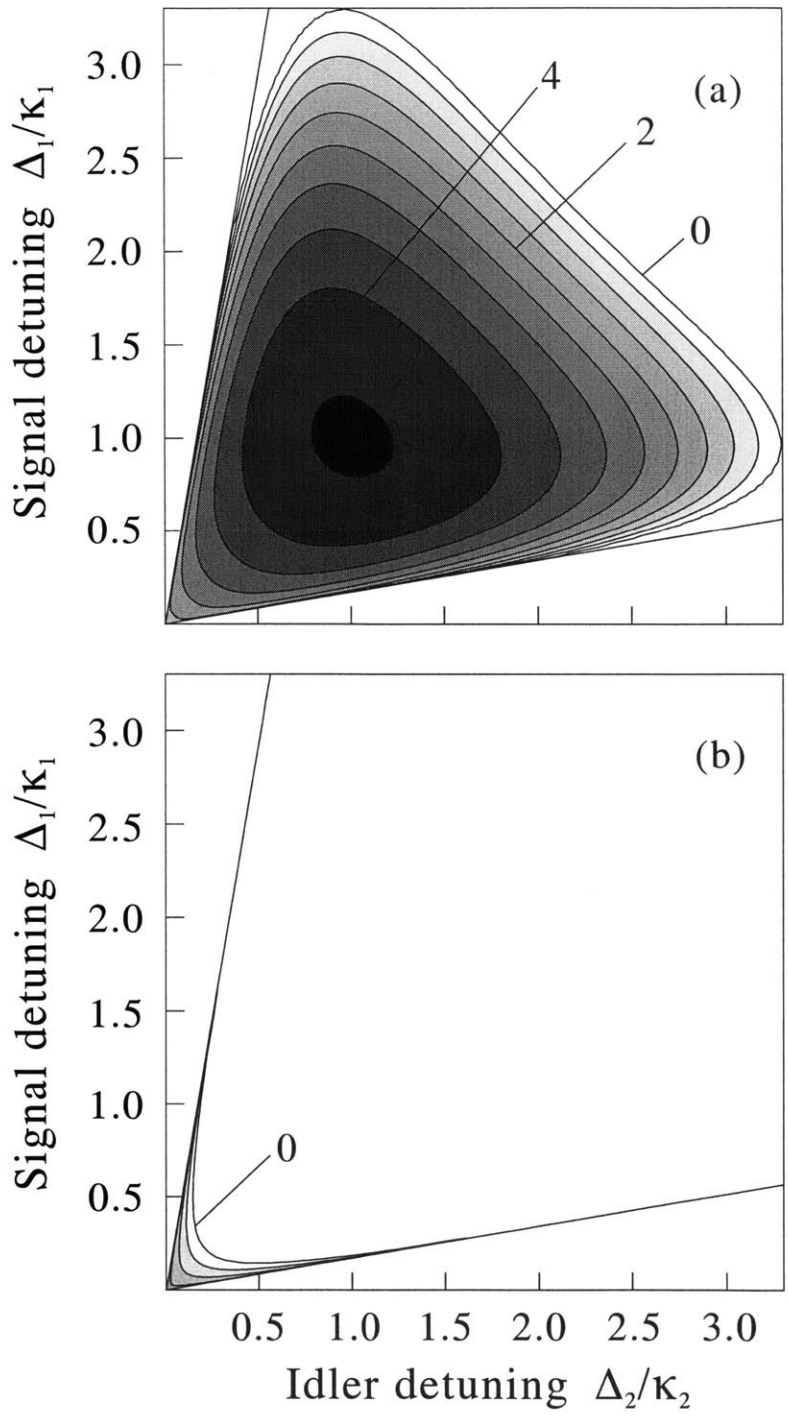

Figure 2-4: Contour plots of the total output powers for (a) the lower-threshold SPLOPO state and (b) the higher-threshold state under the condition of strong coupling $\epsilon_0/\sqrt{\kappa_1\kappa_2} = 1$. The output power is scaled by $\kappa_1\kappa_2/2\chi^2$.

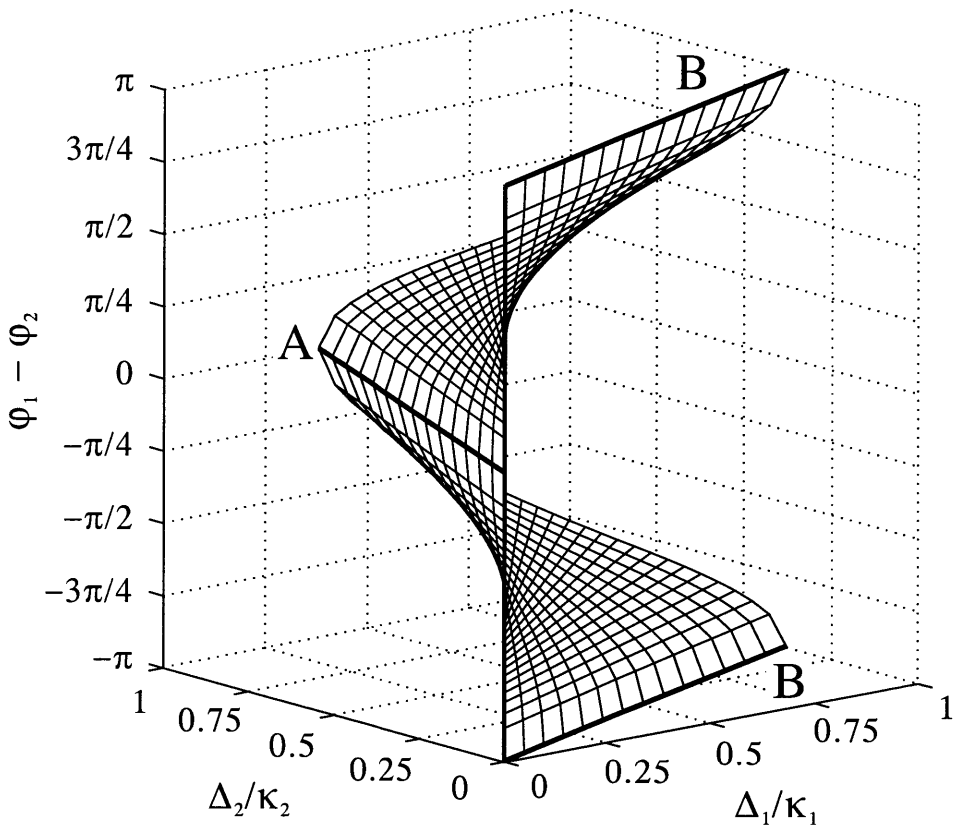

Figure 2-5: Plot of the signal-idler phase difference $\varphi_1 - \varphi_2$ as a function of the normalized cavity detunings for the two SPLOPO states. The range of one state is from 0 to π (top half) while the other state spans from 0 to $-\pi$ (bottom half). The two states have the same phase difference of 0 (heavy line A) and π (modulus 2π, heavy lines B) at the two ends of the locking range. $\epsilon_0/\sqrt{\kappa_1\kappa_2} = 0.5$ and $\theta = 0$.

2.2 Observation of two distinct phase states

Figure (2-6) is a schematic of our experimental setup for the SPLOPO. We frequency-doubled a diode-pumped cw 1064-nm YAG laser to pump the OPO, which contained a $3 \times 3 \times 10$-mm KTP crystal that was cut for OPO operation at frequency degeneracy (crystal cut parameter: $\theta = 90°$, $\phi \simeq 23°$). The OPO cavity was formed with a 10-cm-radius input mirror and a 2.5-cm-radius output coupler and had a nominal free spectral range of ~1.14 GHz. The input (output) mirror was coated for high transmission (maximum reflection) at 532 nm and maximum reflection (0.75% transmission) at 1064 nm. The KTP crystal and the zero-order QWP were antireflection coated at both 532 nm and 1064 nm, and the QWP was aligned nearly normal to the propagation axis. As described in section (2.1.1) $\epsilon_0 \propto \sin 2\psi_q$, where ψ_q is the angle between the QWP's fast axis and the crystal's c-axis $\vec{i_2}$. At $\psi_q = 0°$ there was no polarization mixing and we observed that the threshold was approximately the same with or without the QWP. We have also confirmed that at $\psi_q = 0°$ we could continuously tune the OPO through frequency degeneracy without any sign of self-phase locking by varying the crystal's temperature.

Typically, with ψ_q initially set to zero, we tuned the OPO close to frequency degeneracy with a signal-idler beat note of < 600 MHz that was detected by a 1-GHz InGaAs photodetector, D1. Part of the vertically polarized signal output was monitored by detector D3 and fed back to stabilize the OPO signal intensity at a preset level, while the horizontally polarized idler was monitored by detector D4. The OPO threshold was ~65 mW, although we had both higher and lower thresholds depending on the alignment of the crystal and QWP. The OPO was usually operated at a pump level of 120 mW. Under stable cw operation we set ψ_q to the desired value and tuned the crystal temperature to bring the beat note closer to zero. As the beat frequency came within the capture range, self-phase locking occurred. The capture range was a function of the QWP angle ψ_q and the cavity's free spectral range. Typical capture ranges were ~20 MHz/degree for ψ_q up to 4°. We have also measured a capture range of 300 MHz at $\psi_q = 8°$ for a shorter cavity with a 3-GHz

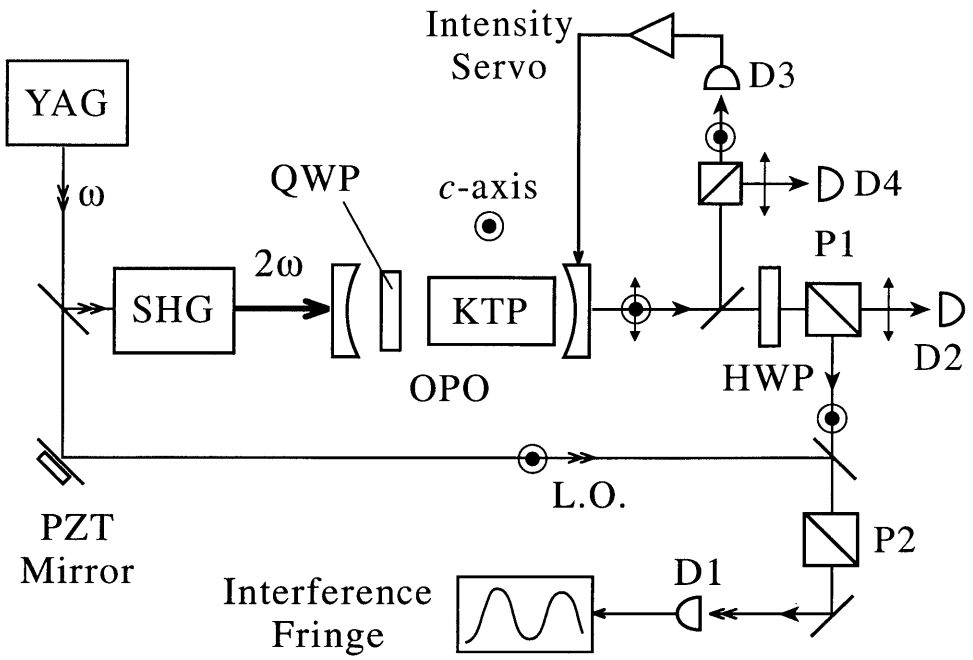

Figure 2-6: Schematic of the experimental setup. SHG, second-harmonic generator; PZT, piezoelectric transducer. See text for other definitions.

free spectral range.

The signal and idler outputs passed through a half-wave plate (HWP) and then a polarizer P1 for analysis of their frequencies, phases, and polarizations. The horizontally polarized, transmitted output of P1 was monitored by detector D2. The vertically polarized, reflected output of P1 was mixed with a local oscillator (LO) that was derived from the YAG laser, and the homodyne signal was detected with the 1-GHz detector, D1. A second polarizer, P2, aligned for transmission of vertically polarized light was placed before D1 to block any leakage of horizontally polarized light from P1.

When the angle ψ_h between the HWP's fast axis and the crystal's c-axis was set to 0° the idler was transmitted and the reflected light was the intensity-stabilized signal. We monitored the dc portion of the homodyne signal as the LO phase was varied using a piezo-mounted mirror. The ac portion of the D1 output was sent to a rf spectrum analyzer to measure the signal-idler beat note that was obtained when the LO was blocked and $\psi_h \approx 22.5°$ was set to project the signal and idler onto a

common polarization axis.

Trace (a) in Fig. 2-7 shows a typical LO-signal interference at $\psi_h = 0°$ (for $\psi_q = 2°$). We adjusted the LO power to match the signal power of ~0.6 mW at D1 (set as 1 arbitrary unit). The interference pattern confirms that the signal and LO had the same frequency and were phase coherent and hence the OPO was self-phase locked. Trace (b) of Fig. 2-7 shows an interference pattern that indicates that the signal phase had a $\sim \pi$ phase shift relative to that of trace (a). The switch between traces (a) and (b) in Fig. 2-7 was usually triggered by a momentary perturbation in the OPO operation (without breaking the intensity servo). The two SPLOPO oscillation modes are labelled as p state (*preferred* state with lower threshold) and n state (*non-preferred* state with higher threshold). Traces 2-7(a) and 2-7(b) belonged to the same p state with the same threshold, sum and difference phases, but they differed by a π phase shift in both the signal and idler fields. We observed similar interference and phase shift between the LO and idler at $\psi_h \approx 45°$. We note that the minimum (maximum) amplitude of the interference does not reach 0 (4) owing to mode mismatch. Trace (c) of Fig. 2-7 is a LO-signal interference for the n state that is phase shifted from trace 2-7(a) by ~67°. The switch between phase states usually occurred after a large perturbation or a break in the intensity servo.

We determined by the following observations that under our experimental conditions the n phase state had a higher threshold (various ψ_h angles): In one set of measurements with a pre-self-phase locked pump threshold of ~40 mW and a pump level of ~100 mW, we found that the p state occurred slightly more often than the n state. However, in another set of measurements in which the pump threshold was ~90 mW and the pump level was ~110 mW, we observed the n state only once out of ~100 measurements. This is consistent with theory that predicts a higher threshold for the n state near the center of the operating range.

To characterize the OPO further, we used detector D2 to monitor the transmitted output of P1. Figure 2-8 shows the D1 and D2 outputs for the (a) p state and (b) n state at $\psi_h = 103°$ and $\psi_q = 1°$. The angle $\psi_h = 103°$ was chosen because at this angle the D1 output of the p state yielded the maximum interference. The

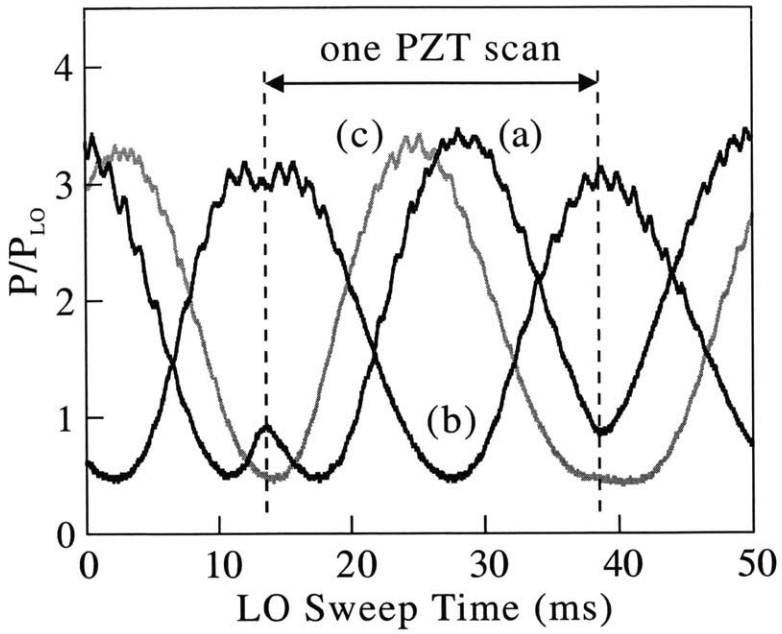

Figure 2-7: LO-signal interference under self-phase locked conditions ($\psi_q = 2°$, $\psi_h = 0°$) for (a) the p state, (b) the p state with a π phase shift in both ϕ_1 and ϕ_2, and (c) the n state.

nonzero D2 output for the p state indicates that the output was elliptically polarized. A comparison of the D1 and D2 outputs for the p and n states in Fig. 2-8 clearly shows that the two states have different ellipticity. We can therefore obtain the phase difference $\phi_d = \varphi_1 - \varphi_2$ for each state by varying ψ_h and analyzing the corresponding D1 and D2 outputs. We should point out that even though the two states had different threshold levels the OPO intensity servo always set the signal power level at 1 unit. However, the idler power could vary by as much as 50% which was confirmed by measurements at detector D4.

We made extensive measurements of the p and n states of the SPLOPO as a function of ψ_h, often by maximizing or minimizing the D1 or D2 outputs. For each D1 or D2 measurement the signal and idler powers were recorded by D3 and D4. The signal-idler beam walk-off prevented simultaneous mode-matching between the LO and the signal, and between the LO and the idler. We used a numerical fitting program to estimate $\phi_d(p)$ and $\phi_d(n)$ for a set of 28 different measurements taken at

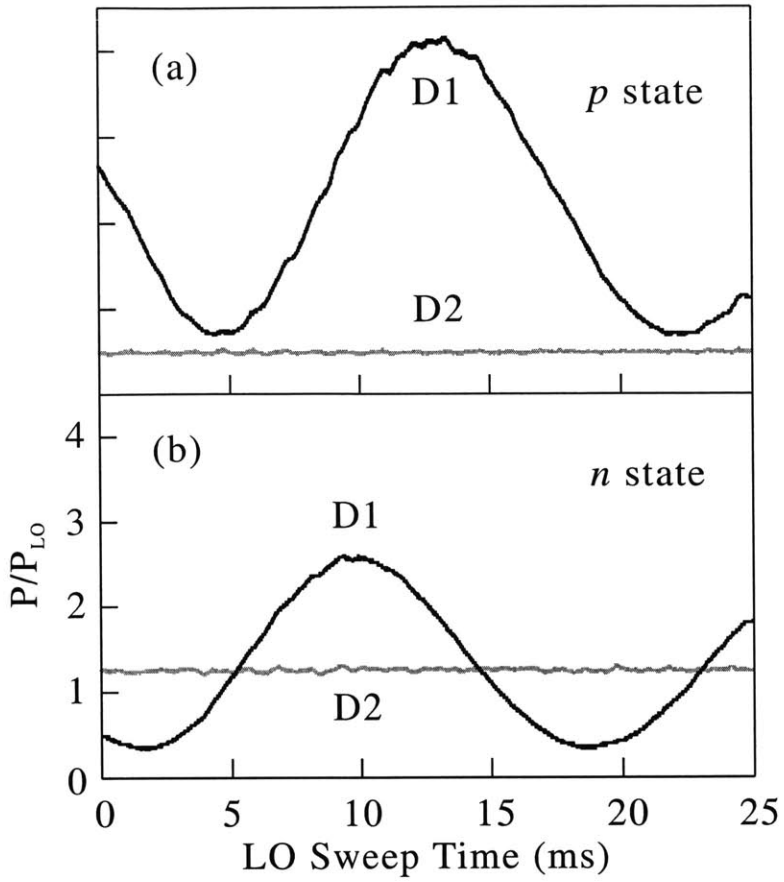

Figure 2-8: Outputs at detectors D1 and D2 ($\psi_q = 1°$, $\psi_h = 103°$) for (a) p state and (b) n state. At $\psi_h = 103°$ the D1 interference of the p state was maximized.

$\psi_q = 1°$ with a fixed pumping level and a fixed signal intensity servo level. The mode-matching efficiencies among the LO, signal, and idler beams were estimated from the interference visibilities. These numbers were then used in the fitting program in the form of overlap integrals (a measure of the mode-matching efficiencies): LO-signal at 78%, LO-idler at 38%, and signal-idler at 49%. The small idler-related overlap was caused by the signal-idler walk-off and by our efforts to optimize the LO-signal mode matching. We obtain (within $[-\pi, \pi]$) $\phi_d(p) = -154°$ and $\phi_d(n) = 21°$ with a standard deviation of 12° and 13°, respectively, and $\theta = 108°$. The difference in ϕ_d between the p and n states is 175°, which is consistent with theory for measurements that were made near the center of the temperature operating range. It should be noted that since the DRO was operated in a constant signal power mode using a

side-locking servo, even when the DRO switched between the two SPLOPO states the same signal power was maintained due to the servo. Since the two states had different thresholds, in general the cavity detunings for the two states must be different in order to produce the same signal power. Therefore we cannot directly compare the details of the experiment such as the change in the signal-idler phase difference for the two states with the theoretical results in this thesis. A proper comparison would require a knowledge of how the cavity detunings were modified when the switch between the two states occurred.

Chapter 3

Periodically-poled nonlinear materials

Periodic poling in ferroelectric crystals allows for efficient nonlinear interactions over a broad wavelength range via quasi-phase matching (QPM). QPM is a way to enable three-wave mixing of the pump, signal, and idler fields with wavelengths λ_p, λ_s, and λ_i that would not have been possible using birefringent phase matching due to phase mismatch:

$$\Delta k = k_p - k_s - k_i.$$

One way to interpret the phase mismatch is that the interacting fields have different phase velocities in the medium, and as the fields propagate over one coherence length ($l_c = \pi/\Delta k$) the phase mismatch $\Delta k l_c$ slips by 180°. This reverses the direction of the power flow: instead of from the pump to the signal and idler, power flows from the signal and idler fields to the pump. In addition to the energy conservation requirement introduced earlier $\omega_p = \omega_s + \omega_i$, for significant power conversion the phase matching condition must be satisfied:

$$\Delta k = 0.$$

This condition can also be interpreted as imposing the momentum matching among the interacting photons, although momentum conservation is not strictly required in a finite medium [9]. In the case of collinear phase matching this condition implies the

following relationship among the refractive indices at the interacting frequencies

$$\omega_p n_p = \omega_s n_s + \omega_i n_i. \tag{3.1}$$

Taking into account energy conservation, this can be expressed in a useful form [9]:

$$\omega_s(n_p - n_s) + \omega_i(n_p - n_i) = 0. \tag{3.2}$$

From Eq. 3.2 it can be seen that perfect phase matching can only be achieved for $n_s \leq n_p \leq n_i$ or $n_i \leq n_p \leq n_s$, while $\omega_p > \omega_s, \omega_i$. This is not possible for an isotropic material with a monotonic dispersion relation (refractive index vs. frequency). However, in a birefringent crystal with different dispersion relations for ordinary and extraordinary polarizations it is possible to find choices of input frequencies, input polarizations, propagation axis, and crystal temperature such that this condition is met. In the decades since the inception of nonlinear optics a number of nonlinear crystals have been found for birefringent phase matching at various spectral regions such as potassium dihydrogen phosphate (KDP), potassium titanyl phosphate (KTP), beta barium borate (BBO), lithium triborate (LBO), silver thiogallate ($AgGaS_2$), lithium iodate ($LiIO_3$), lithium niobate ($LiNbO_3$), potassium niobate ($KNbO_3$), rubidium titanyl arsenate (RTA), and cesium titanyl arsenate (CTA). The choice of field polarizations are classified as type I or type II depending on whether the signal and idler have parallel polarizations (type I) or perpendicular polarizations (type II). For either type there is always one field that is perpendicular to the other two which also limits the components of the nonlinear susceptibility tensor which can be used.

A different approach is taken with QPM interactions. Instead of selecting conditions such that the phase velocities of the interacting fields are equal, the phase slip is corrected by periodically resetting the relative phases to prevent a change of power flow. This is accomplished by periodically reversing the direction of the spontaneous polarization in the crystal before the direction of power flow changes. The result is a crystal with periodically alternating ferroelectric domains forming a QPM grating.

In the simplest case the duty cycle is 50% with equal sections of length l and period $\Lambda = 2l$. The only requirement is that the phase mismatch acquired in a section is $\Delta kl = m\pi$ where m is odd. For the most efficient interaction the grating is 1st-order where $m = 1$. For interactions that would require periods that are too small to fabricate the 3rd-order ($m = 3$) or higher gratings can be used with a penalty in efficiency. The details of QPM are covered extensively in various publications [40, 41].

In recent years the use of QPM to achieve efficient, engineered, non-critical phase matching in various nonlinear crystals has become standard practice. This was made possible by advances in electric-field poling of ferroelectric crystals. Though it had been known for many years that ferroelectric domains could be reversed by application of a strong electric field, the first demonstration of periodic poling at room temperature with a lithographically-defined electrode pattern was made by Yamada, *et al.* in 1993 [8]. Two years later the first single-pass demonstration experiments were published using the same electric-field poling technique in PPLN [42, 43], as well as in periodically-poled KTP (PPKTP) [44]. Then in 1995 and thereafter there was a dramatic increase in published research activity in this area including the first OPO using PPLN [45].

Among the various ferroelectric materials used for QPM, lithium niobate is a well known material that is a popular choice for several reasons. It has a large nonlinear coefficient compared to other materials. It is used in many other applications for its optical and electro-optic properties and is therefore produced in high volume at reasonable prices. It has a large transparency range from ~350 to ~5000 nm. One drawback in using lithium niobate is its susceptibility to photorefractive damage, particularly when being pumped by 532 nm light. This effect can be greatly reduced by heating the crystal above 120°C. This is not a problem for our application since we use low pump powers of a few mW with a PPLN crystal that is heated to above 140°C.

3.1 Device fabrication

Photolithography is a mature process which is ideally suited to the task of creating a metal electrode grating with a specified period and duty cycle needed for QPM devices. When a voltage is applied to generate a field inside the crystal larger than the coercive field (21 kV/mm for lithium niobate) the domains start to flip. This generates a polarization current which draws current from the high voltage supply for the time it takes to flip all the domains under the electrode. In addition to giving a precise definition of the grating period, the flexibility inherent in photolithography allows for multiple gratings on a single device. Gratings can be placed side-by-side for easy tuning [46, 11], or in series along the same propagation axis to phase match multiple interactions [47]. The design procedure described here allows the option for both types of multiple gratings.

3.1.1 QPM grating design

The electric-field poling procedures (done with facilities provided by MIT Lincoln Laboratory) are described in detail in sections (3.1.2) and (3.1.3). This section briefly describes the design of a typical lithographic mask which is used to define the metal electrode for the QPM devices. We use a 4-in×4-in, 0.060-in thick mask substrate made of Quartz or White Crown glass. The usable area is defined by the size of the openings in the available mask holders. The size of a single device is limited by the size of the lithium niobate wafer that is used. For typical devices, which are a few cm long and about 1 cm wide, several devices can fit on the same mask. For each device the desired period (or periods for multiple interactions) are calculated using the Sellmeier equations for the refractive indices. Additional parameters are then specified for each device and for the relative placement of the devices on the mask.

To facilitate accurate and flexible mask design we wrote a set of AutoCAD^{TM} scripts to generate the file format required by the mask vendor from an arbitrary set of specifications (which are included in Appendix A). The file must indicate which parts of the mask are to be opaque and which parts are to be clear. A negative

photoresist is used which means that the areas exposed to UV light are developed away, and the surface of the crystal that is underneath the UV-exposed photoresist is revealed. So the metal that the electrode is made of will be deposited on the crystal according to the pattern of the clear part of the mask.

In addition to the metal that forms the grating teeth, metal must be deposited to ensure that all of the metal teeth make contact with the high voltage source supplying the unpaired poling current. A single device consists of adjacent gratings which are connected to each other by 50-μm-wide "contact strips" that run along the length of the device (perpendicular to the grating teeth). The entire device is then surrounded by "contact pads" that join to form a 1-mm-wide frame around the device. This is illustrated in the sketch in Fig. (A-1) of Appendix A. The device will be covered with insulating layers of fused silica and photoresist such that only the contact pads make contact with the liquid electrolyte. Contact strips improve fidelity of the gratings by isolating them from defects of an adjacent grating. For "long" periods (over $\approx$15 μm) it is best to make the individual gratings no wider than 2 mm, separated by contact strips. For "short" periods (under $\approx$10 μm) there should be no more than 500 μm between contact strips.

One of the most important design parameters of the QPM grating is its duty cycle. In the poling process the domains tend to spread beyond their defining electrodes. Modelling of the kinematics of the domain growth process has shown that the domain growth slows rapidly to a target value which depends on the metal duty cycle and poling voltage used [48]. Our approach uses this behavior to aid in reaching a target duty cycle. The poling current is integrated in real-time and turned off by the computer when the target duty cycle is reached. This computer control is described in section 3.1.3. The metal duty cycle is designed to be 40% for long periods with a target duty cycle of 50%. Short periods have a metal duty cycle of around 20% and a target duty cycle of 35%. Here the target is kept below the optimal 50% to reduce the number of domains that merge together. Even though it is ultimately the poling current controlled by the computer that determines the amount of spreading, the compensation designed in the metal duty cycle assures that when the target duty

cycle is reached the domain wall velocity has slowed enough to have an acceptably small turn-off overshoot of the poling current.

After each device has been specified, it is also necessary to design an additional mask that can be used to pattern the insulating photoresist layer mentioned above. This layer should have an opening that exposes just the contact pads of the device. So a separate contact pad mask can be designed which is opaque except for a frame for each device that only exposes the contact pads. Since the smallest feature of this mask is on the order of 1 mm it can be manufactured more economically as a separate mask. A mask with the smallest features on the order of a few μm and tolerances on the order of 0.05 μm requires the use of more expensive manufacturing techniques.

3.1.2 Lithography and sample preparation

This section outlines a detailed procedure for preparing the lithium niobate wafer for electric-field poling. Extensive previous work has been done on developing the techniques involved with the lithography and preparation of lithium niobate samples for fabrication of PPLN [49, 48, 50]. The procedures used in this work include refinements and modifications of some of those techniques along with a new method for insulation. The prepared lithium niobate sample will have a metal grating defined by the lithographic mask on its top surface. An overcoating of insulating material will control the electric field distribution around the grating. The bottom surface will be unpatterned and forms the ground plane.

The first step is to obtain a number of rectangular pieces by cutting a uniformly-poled z-cut lithium niobate wafer. The dimensions of the resulting blank starting samples are determined by the size of the grating mask for the particular device being fabricated. As mentioned in section 3.1.1, the size of the mask is limited by the size of the available wafers. Circular wafers with 3-in diameters (purchased from Crystal Technology) were sufficient for all of our devices. We did try 4-in diameter wafers, but found that they cracked more easily when cut with a dicing saw. The thickness of the wafers was 0.5 mm, although these procedures are for the preparation of the surface of the lithium niobate and they would apply to wafers of any thickness.

The dimensions of the blank samples should be large enough to accommodate the device including contact pads, about 4 mm in each dimension for a gasket, and about 6 mm more in each dimension to increase the air path between the positive and ground potentials. This reduces the chance of a spark that provides an alternative and undesirable path for the poling current. If sparking occurs it is not always a catastrophic failure but it does reduce the knowledge of how much poling has occurred. The metal electrode is patterned on the $+z$ face which can be identified by inscribing a light mark on the $-z$ face of the crystal so it doesn't interfere with the lithography. Due to the hexagonal shape of the domains in lithium niobate the domain walls should be parallel to the crystal y axis. Care should be taken to insure that the orientation of the x and y axes are identified as well. Usually the x and y dimensions are different making this easy to do.

After the blank samples have been thoroughly cleaned using standard solvents (acetone, isopropanol) the photoresist can be spun. The thickness of the photoresist depends both on its viscosity and the spinning speed. For long periods we use a relatively thick photoresist, Shipley 1818, yielding a thickness of about 1.7 μm when spun at 5000 rpm. This thickness is helpful for the lift-off process described later. For periods less than about 10 μm we use a thinner resist, Shipley 1805, yielding a thickness of about 0.5 μm when spun at 5000 rpm. This is to ensure that the trenches that will be formed in the photoresist defining the grating will reach the surface of the crystal. This is important because the metal that will form the electrode must adhere to the bare crystal surface. A 10-μm period with a 50% duty cycle would have a trench width-to-height ratio of 3-to-1 (using the thicker photoresist). If this ratio becomes much smaller then the photoresist does not completely develop away to reach the surface of the crystal.

The photoresist needs to be baked after it is spun, which hardens it by evaporating away some of the solvents. We use a bake temperature of 80°C which is low enough to avoid excessive microdomain formation that tends to happen upon exposure to high temperatures [51]. Microdomains are small ($\approx$ 10 μm) hexagonal-shaped areas where the domain reversal takes place without application of a coercive field. This

can be a problem if the electrode width is comparable in size to the microdomains. The samples are baked for 20 minutes and then allowed to cool for at least 5 minutes before they are UV-exposed.

Since we use a negative photoresist the area that is not covered by the mask is exposed to UV light and dissolves more quickly in a developing solution. The exposure process begins by achieving good contact between the lithographic mask and the photoresist on the sample. This is especially important for short-period devices for which the opening in the mask is on the order of a few wavelengths of the exposing UV light. The best way to achieve good contact is to place the sample by hand, with the photoresist side facing down, onto the mask [51]. If necessary, the sample should be gently shifted in order to center it over the grating for the device to be patterned. Then the sample should be pressed down with a thumb or finger until Newton's rings are visible over most of the sample indicating good contact. The sample will stick to the mask and it can then be inserted into the mask aligner. We use a machine with a 405 nm UV lamp with an intensity of 13.5 mW/cm^2.

The exposure time and developing time are two parameters that must be optimized together to find a recipe for creating a well defined pattern in the photoresist. After extensive testing, two recipes were created, one for short periods and one for long periods, with exposure times of 7 and 13 seconds, respectively. The longer exposure time leads to more easily dissolved photoresist that makes a difference in the developing step.

Before the samples are developed they are soaked in chlorobenzene for 14 minutes. This step is important because it makes the sidewalls of the trenches steeper. Only the top surface of the photoresist is affected by the chlorobenzene, which changes the composition of the photoresist and makes it harder to dissolve. Normally the developer dissolves away the exposed photoresist much faster than the unexposed photoresist, but the top edge begins to erode by the time the exposed photoresist is completely developed, and a rounded and sloped sidewall to the trench is formed. By making the top surface dissolve more slowly this sloping effect is mitigated. A steep sidewall is helpful for the metal lift-off step described below. After the samples are

removed from the chlorobenzene and thoroughly blown dry with compressed air they are ready for developing.

The recipe for the long-period gratings uses a developing solution of 1 part Shipley 351 concentrate to 5 parts water. This yields a developing time of 40-60 seconds. The sample is held with tweezers and agitated until the dissolved photoresist is visible in the clear developing solution. A few seconds after this "cloud" begins to die down the sample is removed. The photoresist is then examined under a microscope and put back into the developer for a few seconds at a time if necessary. The main feature to look for is the steep sidewalls described above. The trenches should be entirely clear of photoresist. If the sample is developed for too long the sidewalls appear eroded.

The recipe for the short-period gratings needed to be modified because the narrow trenches would not reach the surface of the crystal if the long-period grating recipe was used. A stronger developing solution (1 part Shipley 351 to 3 parts water) is used to develop more aggressively. With the same exposure time the exposed photoresist would develop in a few seconds. So the exposure time is decreased, increasing the developing time to 10–20 seconds. This allows enough time to prevent over-developing the sample.

It is important throughout the lithography process to keep the sample as clean as possible and free from scratches. However, it is inevitable that some defects exist. Dust and debris can prevent the metal from adhering to the surface which creates gaps in the electrode grating lines, and scratches in the photoresist can cause unintentional metal deposition between the grating lines. Since the electrode grating is contacted on both sides by the contact strips or contact pads, two or more gaps in a grating line can isolate a section from the applied potential. The photoresist can be stripped away with acetone at this point to start over if there are more defects than usual in the grating lines.

The next step is the deposition of the metal that fills in the trenches in the photoresist to form the electrodes. It is first deposited over the entire sample, then a lift-off process removes the unwanted metal by dissolving the remaining photoresist. We use sputtered nichrome (80% nickel, 20% chrome) since it has been found to

have a large nucleation site density that is helpful for poling short periods [48]. We have previously used evaporated gold and found that the sputtered nichrome provides better adhesion during the lift-off process. The target thickness of the nichrome is ~50 nm.

Next, the sample is soaked in acetone for at least 30 minutes. This dissolves the photoresist that is under the metal. If the previous steps succeeded in making the sidewalls of the trenches steep enough then the metal will be much thinner there and will break easily. An acetone spray gun is used to remove the metal. The sample is checked under a microscope to make sure that the remaining metal is intact and free from clinging metal "wing tips" that have not completely broken off (the result of shallow sidewalls).

After the electrode grating is in place an insulating layer needs to be applied to control the surface charge distribution and the fringing fields during the poling phase. The insulating material should have low conductivity as well as a high dielectric constant. For long-period gratings we have successfully used photoresist. However, for a short-period (6.5 μm) grating, Miller found that "photoresist lacked either adequate resistivity when baked in the usual manner, or adequate dielectric strength when super-baked (180°C)" [48]. He used a 0.5-μm-thick layer of spin-on-glass with a dielectric constant of 3.1. This requires a delicate procedure of etching with hydrofluoric acid in order to make contact with the electrode underneath.

After trying this method, we decided to use fused silica which has also been used by others. Like spin-on-glass, it has a low conductivity and a dielectric constant of 3.8. We mask off the contact pads in advance and then coat the sample with a 0.4-μm-thick layer of fused silica. Then on top of this we deposit a 2.2-μm-thick layer of photoresist (Shipley 1818 spun at 3000 rpm) which provides an even higher dielectric constant of around 6. The contact pad mask is then used to remove the photoresist over the contact pads. The procedure to expose and develop the photoresist over the contact pads is the same as that for the long-period gratings except that the chlorobenzene step is not necessary and the development time is reduced to ~30 seconds. Also, instead of manually contacting the sample, it is necessary to use the

mask aligner to align the opening in the mask to the metal contacts on the sample. A schematic of the prepared sample with the deposited materials is shown in Fig. (3-1).

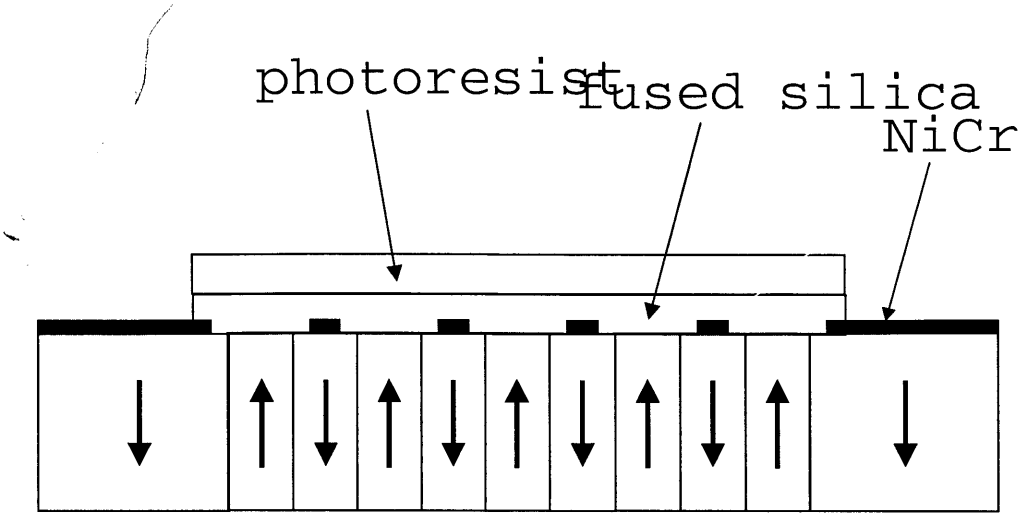

Figure 3-1: Schematic of lithium niobate sample after preparation with deposited NiCr and insulating layers of fused silica and photoresist. Arrows indicate directions of domains after poling is completed.

With this procedure we have poled a 0.5-mm-thick sample with a 7.5-μm-period grating. We have found that this thick layer of photoresist plays a part in determining where domain nucleation occurs, presumably by affecting the field distribution around the electrodes. The methods described here provide another set of tools for consistent fabrication of short-period gratings that can be used in conjunction with other methods such as self-terminating poling current design [48], backswitching [52], or the use of thinner crystals [53].

3.1.3 Electric-field poling

The poling voltage is applied using a liquid electrolyte fixture similar to those used by others [49, 50]. A schematic of the sample mounted in the fixture is shown in Fig. (3-2). The lithium niobate crystal is held between two plexiglas blocks with gaskets cut from 1-mm-thick Viton rubber. The chambers in the plexiglas allow a liquid electrolyte solution (0.5 g/ml LiCl) to make electrical contact between the circuit leads and the crystal surfaces. On the $+z$ crystal face the liquid makes contact

with the metal electrodes through the opening in the photoresist. The $-z$ face of the crystal should have a clean surface in contact with the liquid so that there is a uniform potential across the $-z$ surface. We have found that by cutting out a small piece of the gasket at the top, the electrolyte solution more easily fills the chamber. By providing a way for the air to escape, there is no need for pumping it out with vacuum as we previously did. We then replace the small piece and seal the top with an electrically insulating RTV compound. This helps to reduce the chance of the high voltage creating a spark across the air path which sometimes induces dielectric breakdown of the sample.

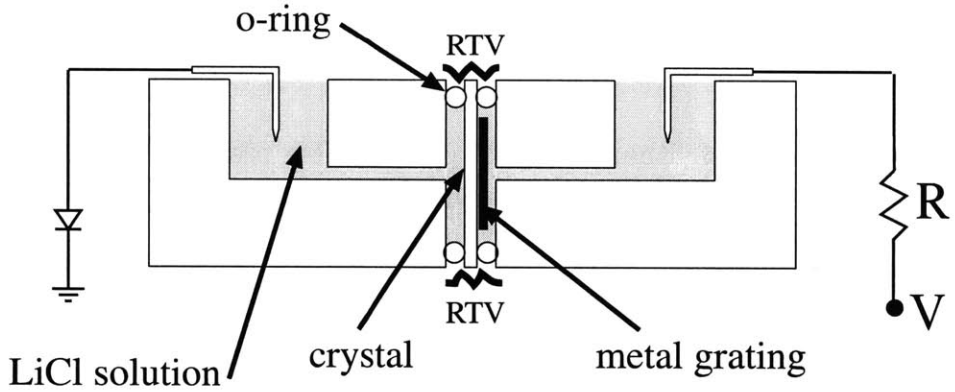

Figure 3-2: The lithium niobate sample is shown here in the fixture which connects to the high voltage circuit. The chamber in the plexiglas is filled with liquid electrolyte that makes electrical contact between the circuit leads and the crystal surfaces.

From the liquid electrolyte, the leads connect to a circuit in which a computer applies a voltage waveform while monitoring the poling current. Fig. (3-3) shows a simplified circuit schematic. While the series resistance R can be used to limit the current and therefore the rate of charge reversal in the crystal, we use a small enough value such that the current is limited by the maximum output current (20 mA) of the high voltage amplifier (Trek Model 20/20). The amplifier has internal current and voltage monitors which were fed back to the data acquisition card in the computer. The diode is there to prevent back-flow of the poling current after the poling is complete which would cause some of the domains to flip back.

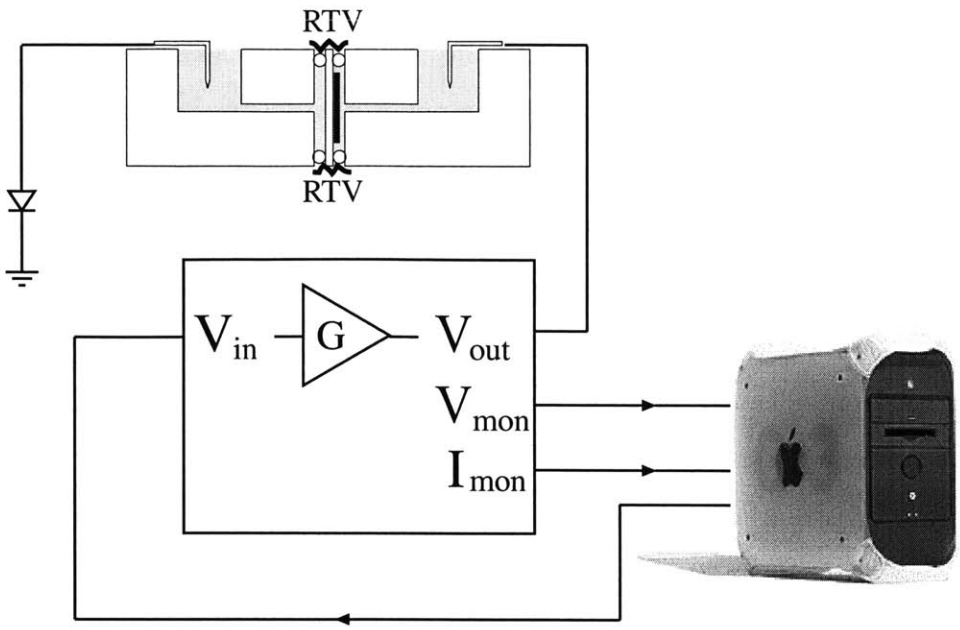

Figure 3-3: Simplified circuit schematic for poling of PPLN device. V_{mon} and I_{mon} are voltage and current monitors which are fed back to control the total charge transfer. The high voltage amplifier has a gain $G = 2000$. The diode prevents back-flow of current.

The data acquisition is performed on a National Instruments PCI-MIO-16E-1 multi-function input/output card. A control loop is implemented in LabVIEW^{TM} software. First the voltage is ramped up slowly (over 60 ms) to 19 kV/mm, just below the poling voltage. It is then held constant for 10 ms before spiking up to 23 kV/mm. This initial spike is used to seed the domain reversal, after which the voltage is lowered to the poling voltage of 21.4 kV/mm [51]. After generating this initial voltage waveform, the program sits in the control loop updating the value of the transferred charge by integrating the monitored current. Due to the low conductivity of the crystal virtually all of the current that flows through the sample is polarization current caused by the domain flipping.

Since the final state of the crystal has the opposite surface charge on the top and bottom surfaces of the domains that have been reversed, it is straightforward to figure out how much charge has to be transferred. It is sufficient to consider the total charge that would be needed to bring the crystal's total surface charge from its

initial state to its final state. The integrated current should be equal to twice the surface charge density times the area of the top electrode, $2P_sA$ (since the surface charge density is equal to the spontaneous polarization P_s). When this amount of charge has been transferred the program exits the control loop and shuts off the poling current by dropping the voltage below the poling voltage again and then ramping it back down to zero. Both the applied voltage waveform and the resulting current waveform are shown in Fig. (3-4) for a crystal with a grating period of 22.1 μm. The initial nucleation spike can be seen, after which the actual applied voltage fluctuates since the amplifier is in its current-limited state during poling. When the target charge transfer is reached the voltage steps below the poling voltage and the current immediately drops down sharply stopping the domain reversal process.

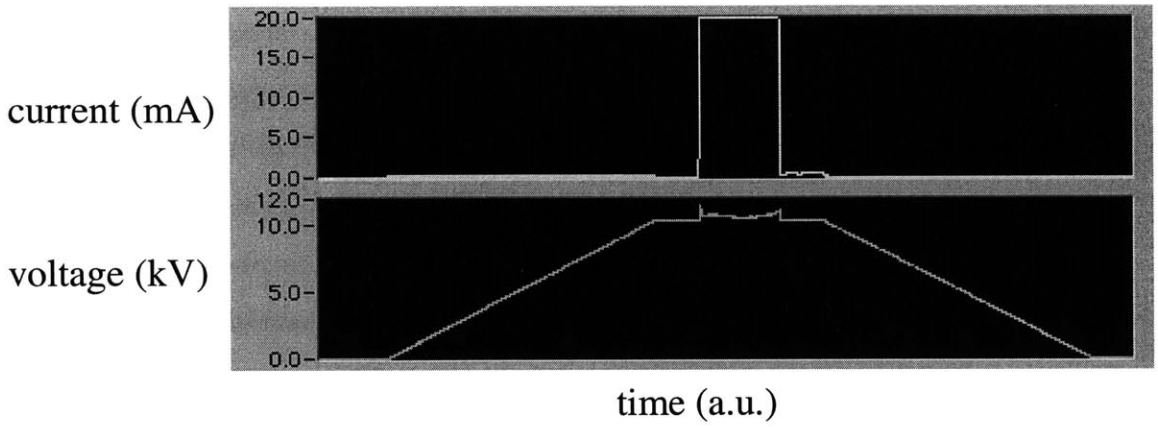

Figure 3-4: Traces of the voltage and current monitors out of the Trek 20/20 high voltage amplifier. LabVIEW^{TM} is used to integrate the current and turn off the voltage when the total charge transferred reaches its target value. In this ideal case the current turns on and off sharply.

There is some variation in the lithium niobate samples that causes problems in the poling process. The biggest problem is dielectric breakdown which happens more often for thicker samples (possibly due to an increase in impurities or defects). There is also variation in the voltage at which the poling current turns on (that is larger than the uncertainty in the measurement of the crystal thickness). If the current starts before the nucleation spike the control loop can recover because the amount of

charge transfer is monitored from the beginning. However, if the current fails to turn off sharply when the target charge transfer amount is reached, the sample becomes over-poled (where the domain walls spread beyond the target duty cycle or merge together). Such a situation is shown in Fig. (3-5) for a 22.4-μm-long grating period. These voltage variations lead to uncertainty and variations in the domain duty cycle.

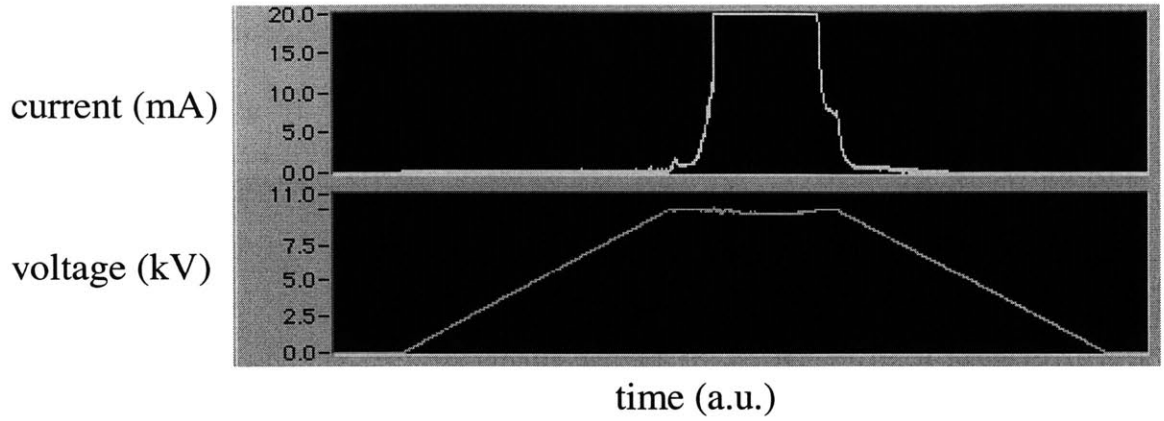

Figure 3-5: More traces of the voltage and current monitors out of the Trek 20/20 high voltage amplifier. In this case the poling current started early and stopped late due to uncertainty in the turn-on poling voltage.

The poled samples must be visually inspected to ensure that the poling is uniform over the entire grating. Defects in the lithography can sometimes cause affected areas to remain unpoled which leads to other areas being over-poled. This is especially true for short periods where merging of adjacent domains is more likely to occur. The grating can be visualized by soaking the crystal in HF acid for about 40 minutes. The positively and negatively charged surfaces etch at different rates. Also the negative charges are attacked more aggressively by the acid creating a frosted appearance that can be easily identified. Before the crystal can be etched, however, the metal grating must be polished away. We use 0.25 μm diamond slurry which leaves the surface smooth enough for etching. Pictures taken under a microscope of both the top and bottom surfaces of the 22.4-μm-period PPLN grating after etching are shown in Fig. (3-6). The over-poling that is evident from Fig. (3-5) only led to a 10% deviation in the actual duty cycle from the target value of 50%. The actual duty cycle of the

poled device is measured directly under the microscope at randomly sampled locations over the surface of the grating. This particular device had an average duty cycle of 55%. The top of the crystal typically has a higher quality since that is where the electrode is patterned. For short-period gratings or extremely over-poled long-period gratings adjacent domains merge somewhere in the bulk of the crystal so that the merged domains are only evident on the bottom surface. The only visible differences between the top and bottom surfaces of this device are that the domain walls are not as straight on the bottom.

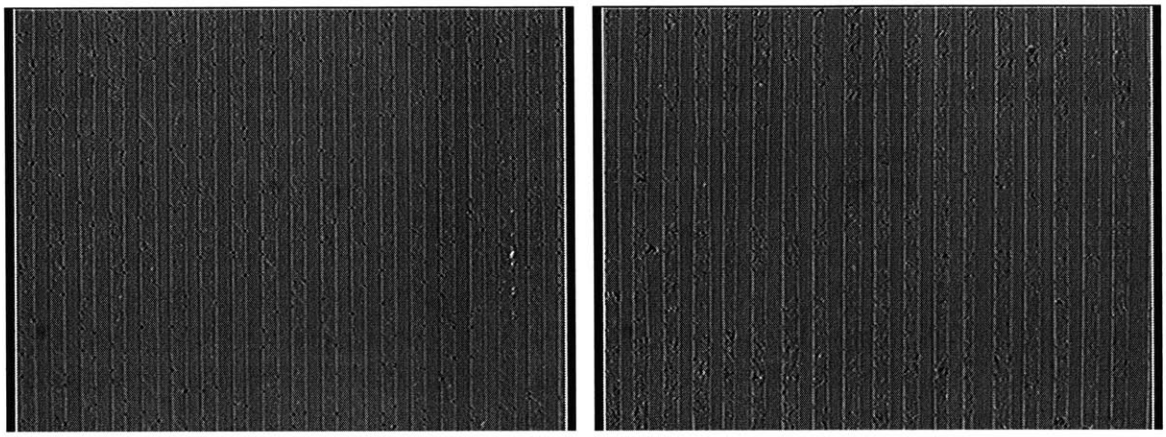

Figure 3-6: Top (left panel) and bottom (right panel) etched surfaces of PPLN grating with a 22.4 μm period. The grating is only slightly over-poled with a 55% duty cycle.

After visual inspection the excess material around the grating is cut away and the end facets are polished and anti-reflection (AR) coated at the particular wavelengths of interest. Our yield of usable devices is lowered mainly by dielectric breakdown of samples during the poling step. For long-period gratings the yield is around 50–70%. However, for short-period gratings it is even lower, around 20%, due to devices which have large patches of merged domains. The shortest period grating successfully poled with these techniques was 7.5 μm. The main limitation to achieving smaller periods is domain merging. Most of the benefits of work described here were in providing well-defined, repeatable procedures for obtaining high quality gratings of periods around 20 μm and longer.

3.2 Periodically-poled $BaMgF_4$ for VUV generation

For years it has been known that barium magnesium fluoride (BMF) has excellent short-wavelength transparency. The absorption edge was thought to be around 170 nm [54]. However, its birefringence was too small to birefringently phase match any interactions for UV generation. Early investigations of BMF in the 1970's were primarily focussed on its nonlinear optical properties and the fact that it could be noncritically phase matched for frequency doubling of 1.06 μm light. However, there were other crystals with much higher second-order nonlinear coefficients better suited for this purpose. BMF was discovered to be ferroelectric in 1969 [55], and this has opened the door, years later, for the use of quasi-phase-matching techniques to finally enable UV and vacuum ultraviolet (VUV) generation in BMF. We have investigated its suitability for electric-field periodic poling and other material properties in collaboration with MIT Lincoln Laboratory [37].

3.2.1 Material Properties

Conventional nonlinear materials have significant limitations for UV and VUV (100–200 nm) generation. Many suffer from solarization (loss of transparency induced by exposure to UV radiation), large Poynting-vector walk-off, or limited VUV transparency. A widely used material, BBO, suffers from solarization, has a walk-off of 4.9° for SHG of 266 nm, and has a short wavelength cut-off of about 185 nm. BMF overcomes these limitations and has the potential of generating the shortest wavelength via a $\chi^{(2)}$ frequency-mixing process using crystalline materials.

BMF has been tested for optical damage due to solarization using 157-nm radiation at 2 mJ/cm^2/pulse with 10-ns-long pulses [56]. After $> 1.1 \times 10^9$ pulses, no change in optical transmission was detected at a $\sim$1% level. Since QPM is necessary to allow nonlinear generation of short wavelengths, noncritical phase matching is used to eliminate Poynting-vector walk-off. The absorption coefficient of BMF was

measured by comparing the differences in the unpolarized optical transmission for two different crystal lengths. The crystals had the same surface preparation and polishing. The results in Fig. (3-7) indicate that the band edge is around 140 nm [37], shorter than the 170 nm previously reported, possibly due to lower impurities.

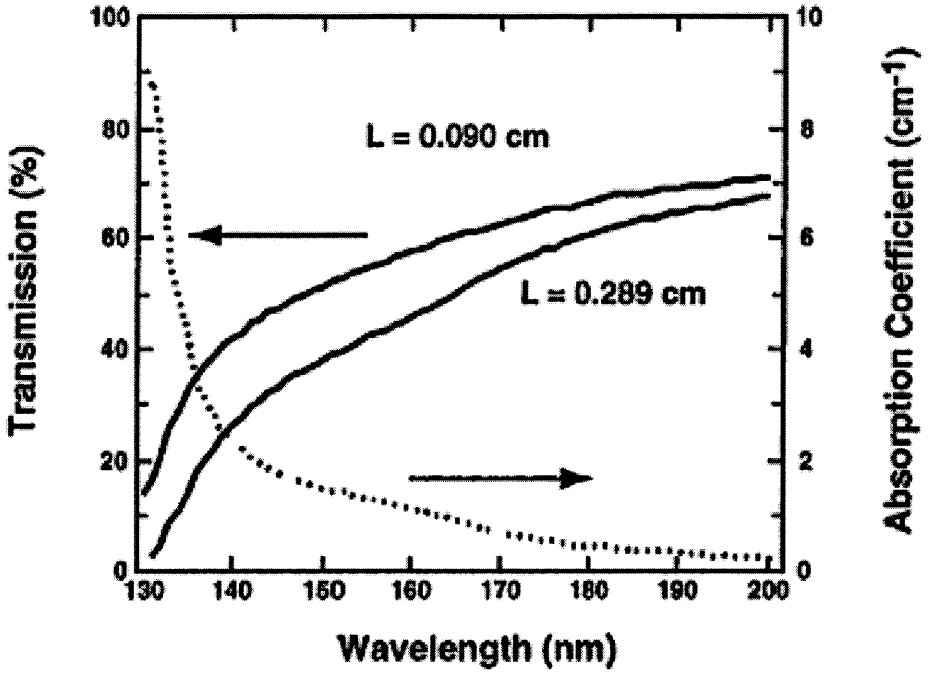

Figure 3-7: Plots of the unpolarized optical transmission for two crystal lengths and the resulting inferred absorption coefficient.

The second-order nonlinear coefficients of BMF are relatively small. The largest coefficient is $d_{32} \approx 0.06$ pm/V, and the second largest one is $d_{33} \approx 0.02$ pm/V [37]. Both can be used with type I quasi-phase matching to generate 157 nm radiation for optical lithography applications. The grating period required when using the d_{33} coefficient is slightly larger. This is important because the periods required are on the order of 1 μm which is smaller than the periods achieved so far in PPLN fabrication by any group. The refractive indices necessary for calculating the grating periods have recently been measured to wavelengths as short as 157 nm [57]. For d_{33}, n_z is needed, and for d_{32}, n_z and n_y are needed. The Sellmeier equation fits to the measured data

are

$$n_y^2 = 2.07971 + \frac{0.006897}{\lambda^2 - 0.00914}, \tag{3.3}$$

$$n_z^2 = 2.12832 + \frac{0.0075537}{\lambda^2 - 0.008979}, \tag{3.4}$$

where λ is the wavelength in units of μm. Fig. (3-8) shows a plot of the period of the QPM grating needed to generate 157 nm with sum frequency generation. The grating period is plotted against the shorter wavelength from 193 nm to 314 nm which is the fundamental for SHG of 157 nm. The periods are shown for both d_{33} (dashed line) and d_{32} (solid line). As shown, a 1st-order grating would require a period of $\sim$1.5 μm which should be achievable with a thin enough crystal. For a first demonstration we fabricated a grating with a 19.2 mm period for 3rd-order quasi-phase-matched SHG of 266 nm from a fundamental of 532 nm. The fabrication process is described in the following section.

3.2.2 Periodic-poling of BMF

We fabricated periodically-poled BMF (PPBMF) using a procedure similar to that described for lithium niobate. The z-cut crystal (for propagation along the x-axis) had a thickness of 500 μm and the $+z$-face was lithographically patterned with a 19.2-μm-period grating. The grating k-vector was parallel to the crystal x-axis. Sputtered NiCr was used for the electrode grating. The 9-mm-long, 4-mm-wide metal grating was overcoated with a 2-μm-thick layer of photoresist with openings for contacting the conducting LiCl solution. The bottom surface of the BMF was in direct contact with the solution, held in place with rubber O-rings. Poling was achieved with a series of 50-ms-long high-voltage pulses applied to a 220-kΩ series resistor, with an in-series diode to prevent back flow of current. Based on the published value of spontaneous polarization for BMF of 7.7 μC/cm^2, a total charge of 5.3 μC was expected for an ideal 50% duty cycle. Figure (3-9) shows the applied voltages and the monitored currents for 19 pulses that were applied to the crystal, and we estimate that a total of 5.4 μC was delivered. The typical poling current was about an order of magnitude lower

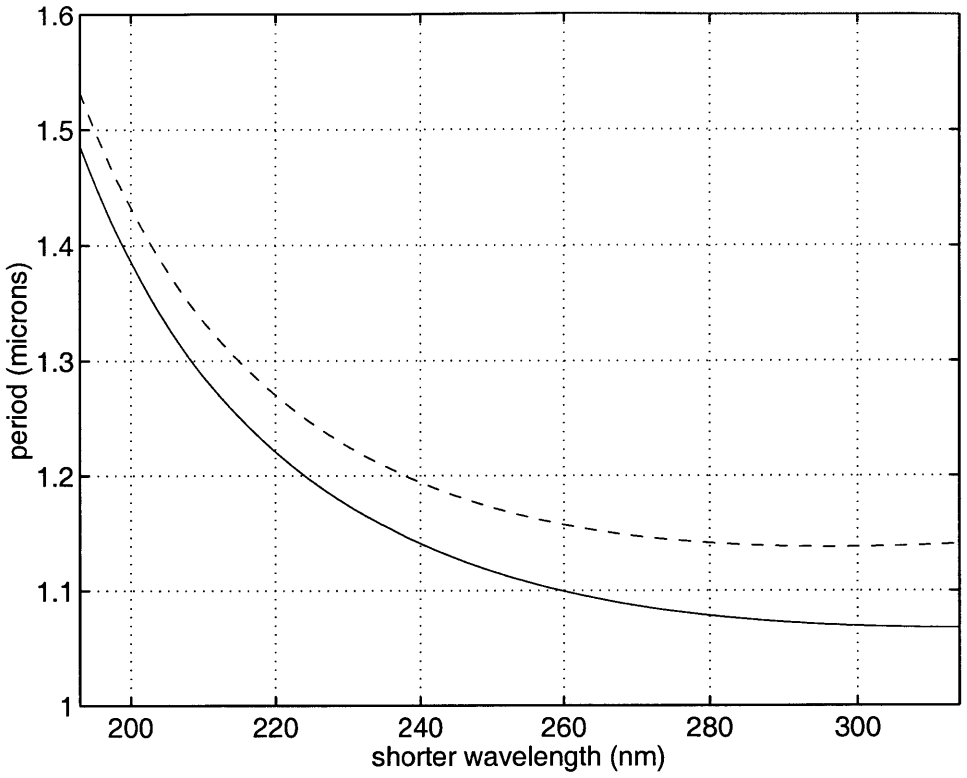

Figure 3-8: Period of QPM grating needed to generate 157 nm with sum frequency generation. Plot versus shorter wavelength, for d_{33} (dashed) and d_{32} (solid).

than that for lithium niobate, consistent with the lower spontaneous polarization of BMF.

The grating was visually inspected using a different method from that used to image PPLN because the usual HF did not differentially etch the positive and negatively charged areas of the BMF surface. It also severely eroded the surface. Another method of imaging a poled device is with the use of an environmental scanning electron microscope. The proper settings are unconventional, but they allow for a high-resolution image of the areas of domain inversion. The resulting image of the PPBMF shown in Fig. (3-10) reveals a high quality grating with a duty cycle matching very closely to the target value of 50%.

The conversion efficiency of the PPBMF grating for generating 266 nm was within $\sim$50% of theory. Reasonable conversion efficiency to the VUV is expected in this ma-

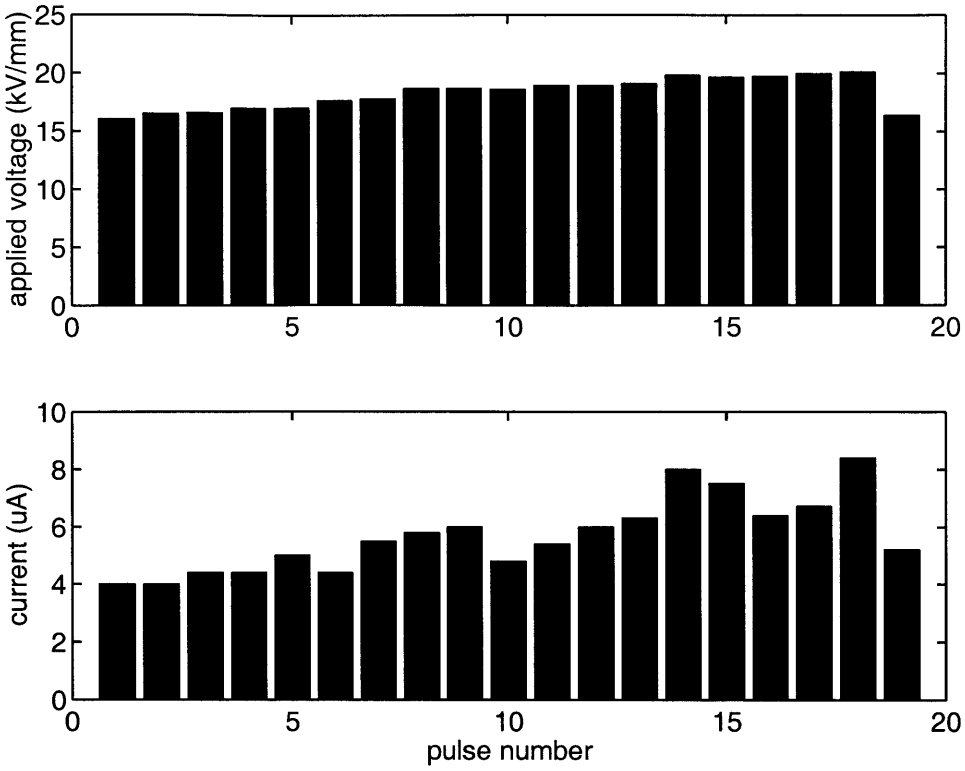

Figure 3-9: Voltage and current of 19 pulses used to pole the BMF grating.

terial assuming 1st-order QPM with d_{32}. For frequency doubling to 157 nm, a conversion efficiency of 13% is projected in the plane-wave limit, assuming an incident fundamental intensity of 1 GW/cm^2 (the damage threshold has been measured to be at least this large [54] at 1.064 μm), a PPBMF crystal length of 1 cm, and no optical absorption at both the fundamental and second-harmonic wavelengths. Though the quality of this long-period grating is high, it remains to be seen how difficult fabrication of short-period gratings will be in this material. Part of the difficulty of fabricating short-period gratings in lithium niobate is controlling the poling current to prevent domain spreading and merging. The intrinsically lower poling current may be an advantage for controlling the domain wall dynamics. It may also be helpful to pole thinner crystals for the first attempts at short periods.

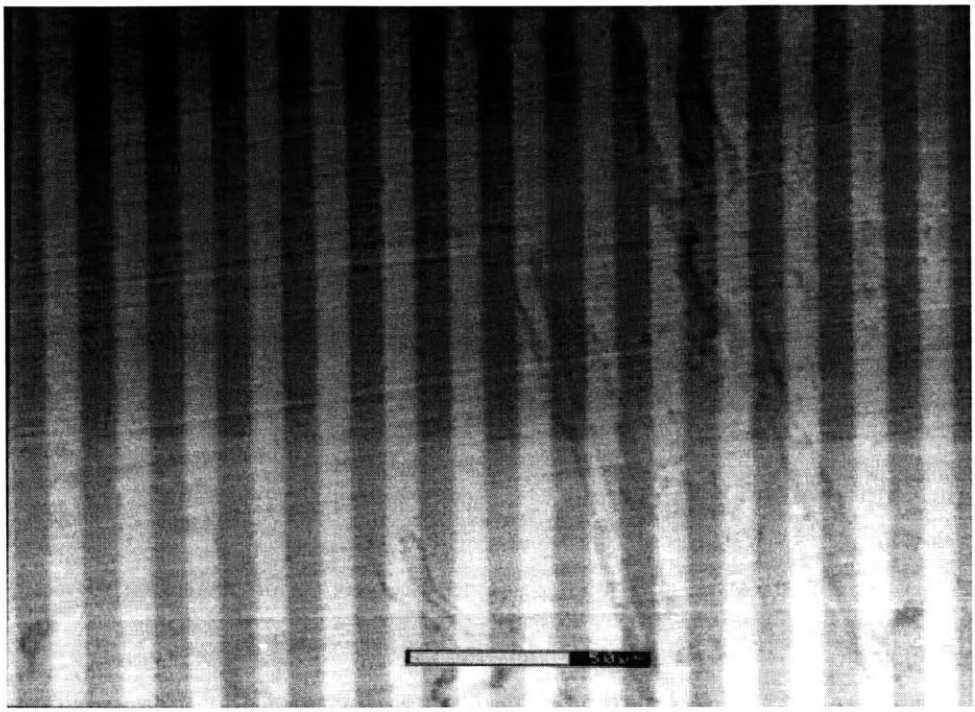

Figure 3-10: Image of $+z$-face of periodically-poled BMF using an environmental scanning electron microscope. The grating period is 19.2 μm and the white scale bar corresponds to 50 μm.

3.3 Application of PPLN to frequency-nondegenerate entanglement source

In a recently proposed singlet-based quantum communication system [32] there is a need to generate entangled photons at 795 nm for local trapped-Rb quantum memories and at 1.55 μm for low-loss fiber-optic transmission to remote locations. An efficient, high-intensity, nondegenerate downconversion source for this singlet-based protocol can be obtained using PPLN with a pump laser at 532 nm. PPLN is an ideal nonlinear material for a nondegenerate entanglement source because of its large nonlinear coefficient, flexibility in operating wavelengths, tunability, and low-cost fabrication.

We have fabricated a 2-cm-long 3rd-order PPLN crystal with a grating period of 21.6 μm that can be type-I quasi-phase matched at $\sim$140°C to yield colinearly propagating downconvereted photon pairs at the wavelengths of 808 nm and 1559 nm. At an operating temperature of $\sim$140°C and only a few mW of pump power, photorefractive damage of the crystal is eliminated. By varying the crystal temperature from 142.4° C to 183.5° C, we could tune the output wavelengths from 808 nm to 795 nm for the signal, and from 1559 nm to 1609 nm for the idler. Specifically, at 183.5° C the downconverted wavelengths were 795 nm and 1609 nm. These wavelengths were picked to match the 795 nm excitation wavelength for the local trapped-Rb atom quantum memory in the long-distance teleportation scheme. The 1609 nm wavelength is compatible with low-loss long distance propagation over standard telecommunications fiber. Time-coincident counting was performed at various operating temperatures and detailed measurements were made at 142.4° C where the output wavelengths were 808 nm and 1559 nm. The co-propagating signal and idler photons were separated from each other using a prism. This was also a convenient way to isolate the pump light from our single-photon counters. It did require that we realign the signal and idler paths into our detectors after temperature tuning because of changes in the wavelengths. However, the need for realignment could be eliminated by using other means to separate the different wavelengths such as dichroic mirrors.

The use of PPLN for the downconverter is well suited for high efficiency photon-pair generation. Not only is its nonlinear coefficient higher than that of the commonly used crystal BBO, but it can also be scaled to longer crystal lengths because it employs noncritical phase matching and is not limited by walk-off as in BBO. Pumping our downconverter with only 0.75 mW of 532 nm light, we measured a signal (800 nm) singles count rate of 4.2×10^6/s with our single-photon counter, an EG&G photon counting module based on a Si APD. The inferred pair generation rate was 1.4×10^7 pairs/s/mW of pump power (corrected for 54% detector quantum efficiency and 1.4× correction factor for detector dead time). The pump linewidth is <1 MHz so the phase matching bandwidth of 146 GHz determines the bandwidth of the downconverted photons.

In addition to high efficiency generation of photon pairs, it is important to provide for high efficiency coupling into a well-defined spatial mode such as a single-mode fiber for easy transport over long (or short) distances [58]. We performed our coincidence counting by coupling both the signal and idler into single-mode fibers for their respective wavelengths. This acts as a spatial mode filter for the downconverted light out of the crystal. It is therefore important to match the mode selection for the signal and idler fields to preserve the correlation between them. We have demonstrated nonclassical time-correlation and high efficiency collection of photon pairs, comparing the coincidence rate with what has been achieved so far [58, 59].

3.3.1 PPLN Characterization

The fabricated 2-cm-long PPLN crystals for entangled photon-pair generation were first characterized using laser sources at the operating wavelengths. Testing was performed with difference frequency generation (DFG) of 795–807 nm light from inputs at 532 nm and 1560–1609 nm. This allowed measurements of the conversion efficiency and the tuning behavior of the crystals. There were several crystals with one of three grating periods, 22.4 μm, 22.1 μm, or 21.6 μm corresponding to 3rd-order QPM for these wavelengths at various temperatures from ~30–180°C. Each crystal had six 2-mm-wide grating sections with the same grating period. Due to

nonuniformity in the poling process some of the grating sections had lower conversion efficiencies than others. The crystals were mounted in an oven that had a maximum temperature setting of 200°C and a ±0.1°C uncertainty. The different grating sections were accessed by translating the oven on a vertical stage. We have also fabricated one crystal with a period of 7.5 μm for 1st-order QPM at 33°C for generation of 795 nm light.

The input laser sources were a Coherent 8 W Verdi laser for the 532 nm light, and a New Focus 4 mW external-cavity tunable diode laser for the ~1600 nm light, which was tunable from 1594-1609 nm. For testing at 1560 nm an Alcatel 20-mW fiber-coupled distributed-feedback (DFB) laser was used. The generated ~800 nm DFG signal was detected and amplified with a lock-in amplifier. The power in the ~1600 nm input light was fixed at 3.3 mW. The 532 nm input light was varied from 80–450 mW for the 3rd-order gratings. Since the 1st-order grating was phase matched near room temperature it was more susceptible to photorefractive damage so the 532 nm power was only varied from 40–150 mW. The ~1600 nm input light was chopped at ~200 Hz. After the crystal a long-pass filter was used to remove the 532 nm light and a Si PIN photodiode was used to detect the ~800 nm light. The photodiode was not sensitive to the ~1600 nm input light. A schematic of the setup is shown in Fig. (3-11).

The two input beams were aligned and mode-matched into the 20-mm-long crystal with a confocal parameter of 30 mm inside the crystal. While monitoring the output of the lock-in amplifier, the temperature was tuned starting from the calculated phase matching temperature to find the actual phase matching temperature. Once a signal was detected it was further optimized by fine tuning the wavelength of the ~1600 nm light. The actual phase matching temperatures for the four grating periods 7.5 μm, 22.4 μm, 22.1 μm, 21.6 μm, were higher than the designed temperatures by 11.4°C, 9.6°C, 7.0°C, 3.0°C, respectively, indicating that the refractive index data used [60] is more accurate for higher temperatures at these wavelengths.

Testing was performed on six 3rd-order devices, each with six grating sections, and one 1st-order device with 24 grating sections. The measured conversion efficiencies

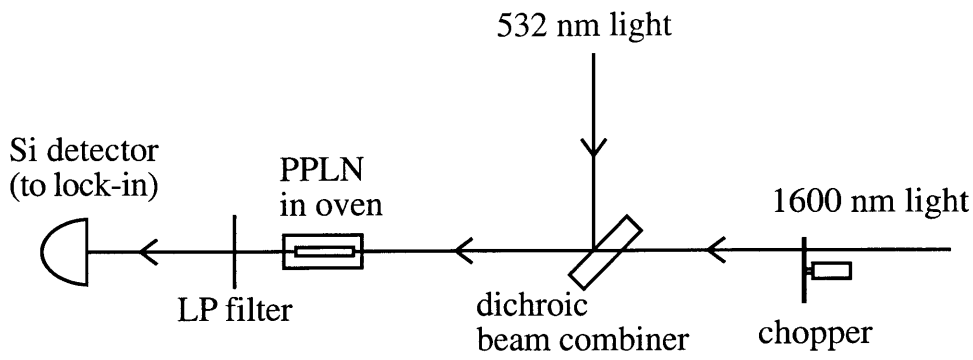

Figure 3-11: Experimental setup for the DFG measurements taken to evaluate the poled crystals. A Si PIN photodiode and a lock-in amplifier was used to detect the generated light. The LP filter is a long-pass filter with cut-off frequency ~700 nm.

varied with different crystals or with different grating sections of the same crystal. The conversion efficiencies obtained were lower than those predicted by theory for an interaction with perfect mode-matching and ideal QPM using the nominal value of $d_{33} = 27.2$ pm/V. There was also variation in performance over the different gratings. Adjacent grating sections on the same device varied by as much as 20%. Before specific results are given some of the reasons for the sub-optimal conversion efficiencies will be discussed.

Some of the discrepancy can be explained by the imperfect mode overlap between the two input fields and mis-alignment of their propagation axes. This may account for a large part of the discrepancy, but does not explain the variation among the gratings. That variation can be explained by non-ideal QPM in the grating. Some of the factors which contribute to the non-ideal QPM include random duty cycle variation, missing domains, and sub-optimal duty cycle [41]. The lithography process ensures that the average grating period is very accurate. However the domain wall locations vary due to the dynamics of the domain inversion. This leads to duty cycle variation which in turn leads to a reduction in conversion efficiency that depends on the standard deviation of the domain lengths. Missing domains occur when adjacent domain walls spread so much that they merge together. This is more of a problem

Device	P_i (mW)	P_p (mW)	$\frac{P_s}{P_p P_i}$ (%/W) (measured)	$\frac{P_s}{P_p P_i}$ (%/W) (theory)
1st-order A	2.86	34.6	0.55	1.78
3rd-order A	2.86	69.1	0.16	0.45
3rd-order B	2.0	55.8	0.041	0.076

Table 3.1: Measured DFG conversion efficiency and comparison with theory based on nominal value of $d_{33} = 27.2$ pm/V. Different focussing where reduction factors $h_m = 0.47$ (A) and $h_m = 0.08$ (B) were used.

for short-period gratings (under $\sim$10 μm).

One of these factors, sub-optimal duty cycle, can be easily modelled and taken into account in the comparison with theory. The effective nonlinear coefficient for QPM is given by

$$d_Q = \frac{2}{\pi m} \sin(\pi m DC) d_{\text{eff}},$$

where m is the order of QPM used, DC is the duty cycle of the grating, and d_{eff} in our case is d_{33} since all of the interacting fields are co-polarized and parallel to the crystal z-axis. The optimal duty-cycle for an odd-order QPM interaction is 50%, and in that case a 3rd-order grating has a factor of 9 penalty in conversion efficiency. A duty cycle of 45% was assumed for the 3rd-order grating based on sampled measurements on the top surface of the crystal. The 1st-order grating, however, had a duty cycle which varied greatly due to the domain spreading which is more difficult to control for short-period gratings. The d_Q estimate for the 1st-order grating assumes a duty cycle of 30% (sampled measurements varied from $\sim$20–40%). The best measured results and comparison with theory under these assumptions is summarized in table (3.1). The results denoted by (A) in table (3.1) assume a focussing parameter of $l/b = 2/3$, as employed in the experimental setup. The result denoted by (B) used a looser pump focussing with a larger confocal parameter such that $l/b = 1/10$ which led to a lower predicted conversion efficiency, but the measured value was closer to this lower predicted value. Even though the 1st-order device has a non-ideal duty cycle and a larger variation in duty cycle it still achieves a factor of $\sim$3.4$\times$ higher conversion efficiency than the 3rd-order device.

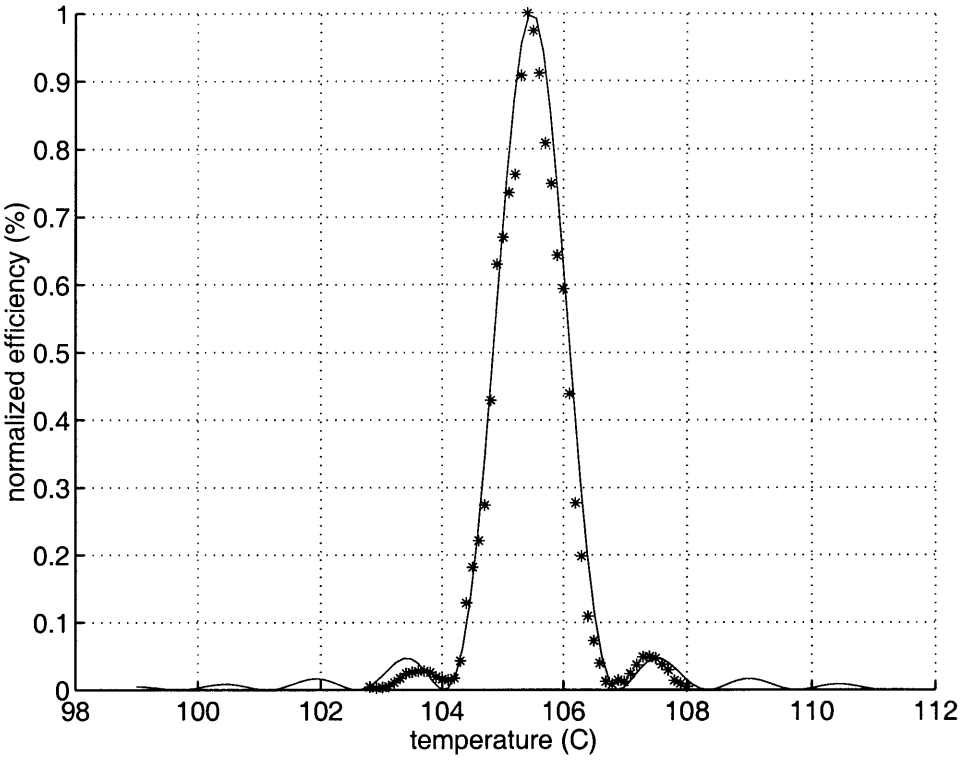

Figure 3-12: DFG conversion efficiency of the 3rd-order 22.1 μm period grating as a function of temperature with FWHM of 1.3°C.

The tuning behavior of the PPLN devices were also examined. The effective interaction length in the crystal can be inferred from a measurement of the width of the tuning curves as a function of temperature or input wavelength. From the Sellmeier coefficient data [60] both temperature and wavelength dependence can be predicted and compared with measurements. The converted power is plotted as a function of both temperature and idler wavelength. Even though the peak conversion efficiency is lower than expected as explained above, we have confirmed that the entire crystal length was phase matched for both the 3rd-order and 1st-order devices from data shown in Figs. (3-12, 3-13). In particular, this confirms that the oven was effectively heating the entire length of the crystal, and these grating sections do not have large gaps of merged or unpoled domains over the length of the beam path. If the effective interaction length were shorter, then the FWHM of the data (1.3°C for

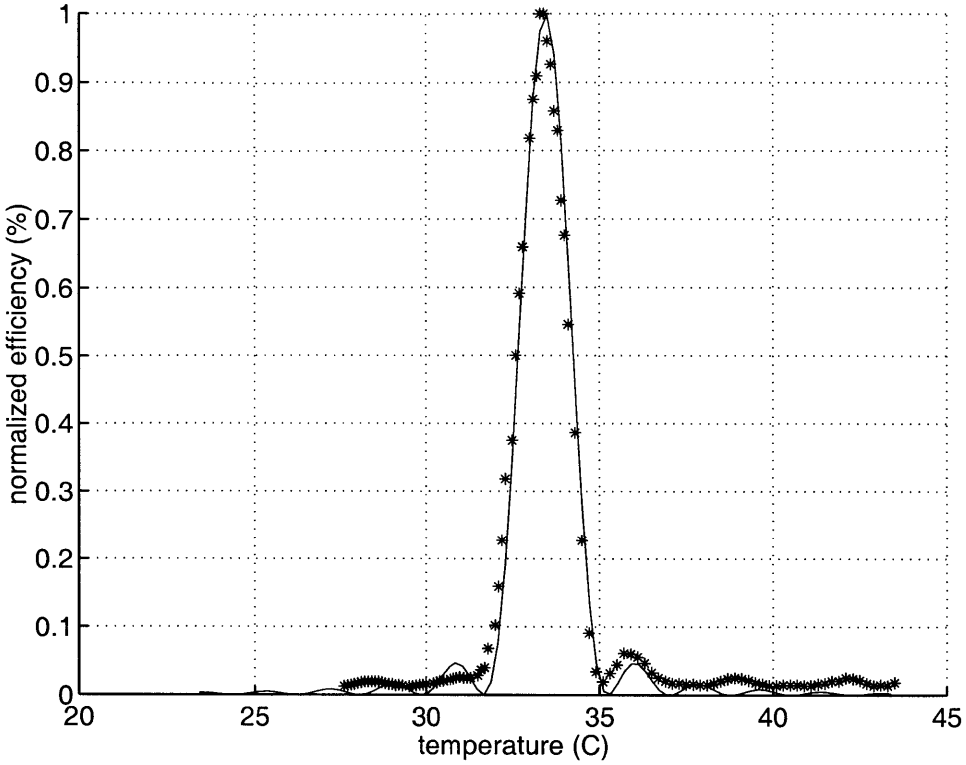

Figure 3-13: DFG conversion efficiency of the 1st-order 7.5 μm period grating as a function of temperature with FWHM of 1.6°C.

the 3rd-order device, 1.6°C for the 1st-order device) would have been wider than the theoretical curve shown in the plots. In both figures, the curve from the Sellmeier fit was scaled in height and shifted in temperature to overlap the data.

The tunable New Focus laser was also used to determine the wavelength-temperature tuning curve corresponding to maximum conversion efficiency. We optimized the converted DFG power by varying the idler input wavelength at successive operating temperatures which allows us to map the wavelength vs. temperature curve. The slope of 1.3 nm/C agrees well with the (dashed) theoretical curve from the Sellmeier coefficients as shown in Fig. (3-14) for a 3rd-order device. (The theoretical curve was shifted in temperature by 4°C to overlap the data.) The laser was also tuned in wavelength to calculate the phase matching bandwidth from the FWHM of the resulting curve shown in Fig. (3-15). Here the curve from the Sellmeier fit was also

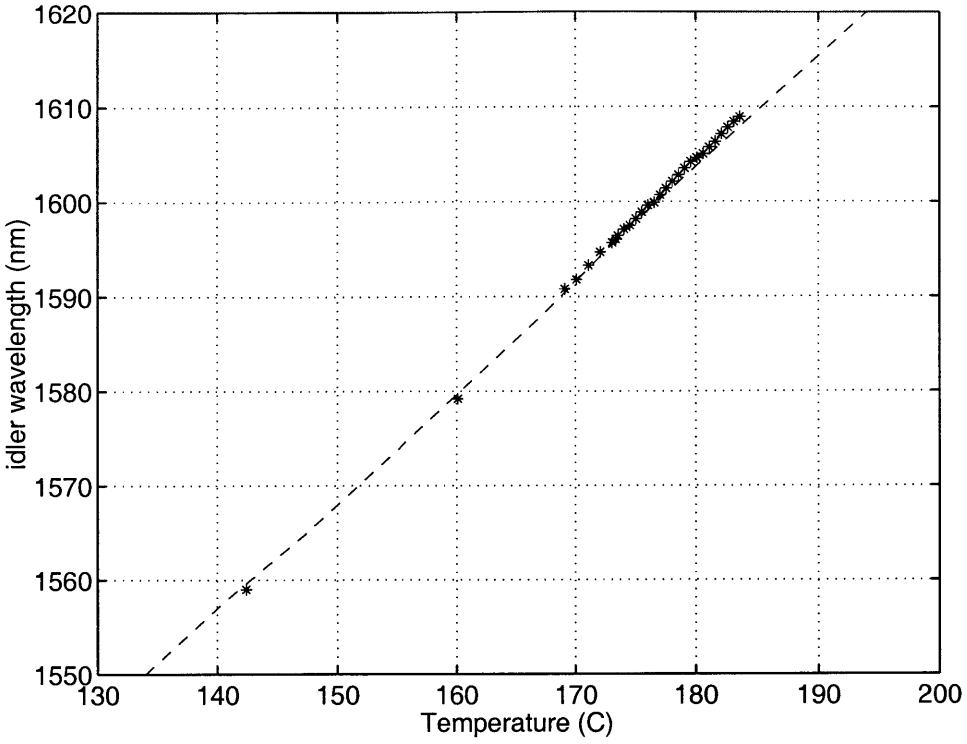

Figure 3-14: Wavelength vs. temperature tuning curve for 21.6 μm period grating of PPLN.

normalized and shifted (by 4.25 nm) to overlap the data. The FWHM indicates a wavelength bandwidth of 1.26 nm, equivalent to a frequency bandwidth of 146 GHz.

3.3.2 Coincidence counting

The signal photons at ~800 nm were detected using an EG&G Si avalanche photodiode (APD) single-photon counting module. The quantum efficiency at 800 nm was measured to be 54%. The counter was actively quenched with a dead time of 40 ns. The dark counts were below 100 counts/sec. The ~1600 nm idler photons were detected using a fiber-coupled InGaAs APD operating in Geiger mode with a passively quenched biasing circuit [61]. The InGaAs APD was cooled to an operating temperature of $-50°$C to reduce dark counts. It was operated with a bias voltage of 2.7 V above the breakdown voltage. Using the 1560 nm source a quantum effi-

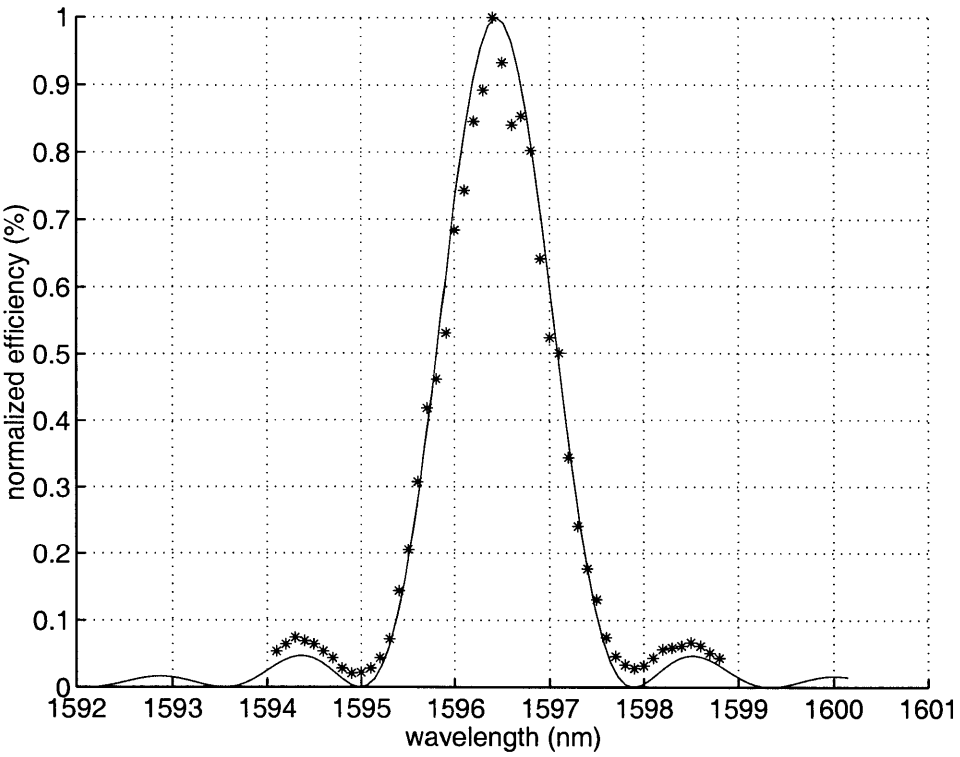

Figure 3-15: DFG conversion efficiency of the 3rd-order 21.6 μm period grating of PPLN as a function of wavelength with FWHM of 1.26 nm.

ciency of ~21% was measured. The dark counts under these conditions were on the order of 10,000 counts/sec. This required gated operation of the device such that the probability of detection of an incoming photon (i.e. the quantum efficiency) is much larger than the probability of a dark count within the time span of the gate. We used 20 ns-long gates so that the probability of counting a dark count was ~0.02%.

The experimental setup is shown in Fig. (3-16). The downconverted signal and idler were spectrally separated by a prism, collected into separate single-mode fibers, and sent to their respective APD detectors. A conditional coincidence counting was performed by using the arrival of the signal photon to trigger the gate for detecting the idler photon. In order to do this the idler photon is delayed with a 70-m span of fiber. Since the signal fiber is 1 m this provides a delay of 345 ns (assuming a propagation speed in the fiber of 2×10^8 m/s) which is ample time for the electronics.

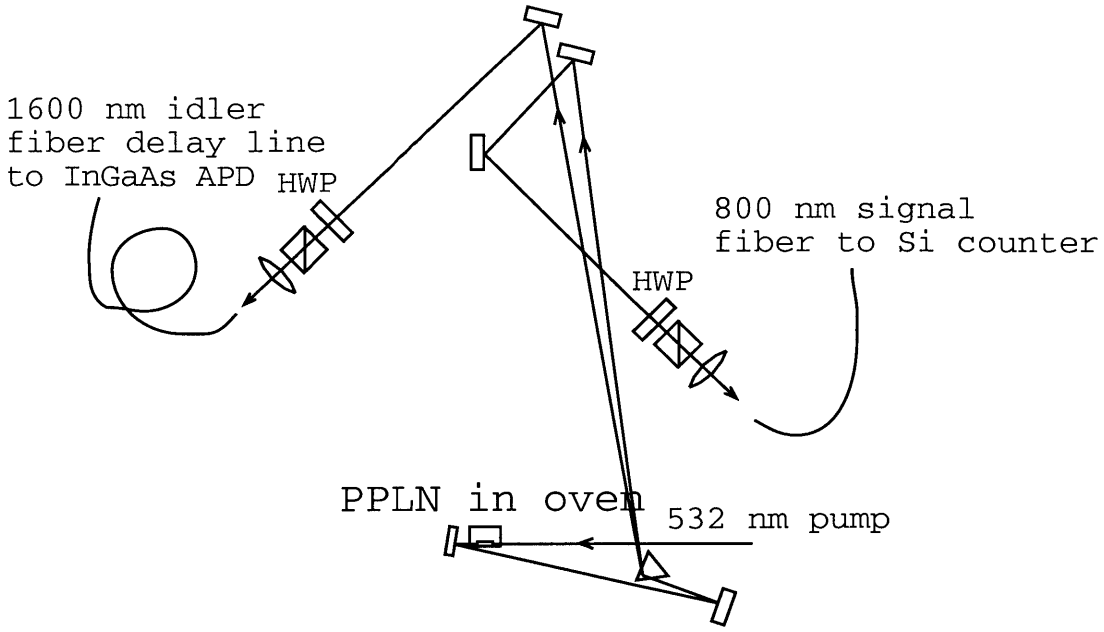

Figure 3-16: Setup for coincidence counting of generated photon pairs.

A detailed timing diagram is shown in Fig. (3-17). The arrival of a signal photon generated a 25-ns-wide TTL pulse from the EG&G photon counting module. This was used to trigger a Stanford Research Systems delay/pulse generator. A minimum time of 95 ns was needed for the delay of the coaxial cable for the electronic signal and the fixed internal delay of the delay/pulse generator. A control pulse T_0 was used to set a maximum detection rate of 10 kHz. During this period of 100 μs any additional signal photon arrivals and subsequent triggers were ignored. The reason this limit was needed was to eliminate the effects of after-pulsing in the InGaAs APD. A variable delay τ_D was used to shift the 20-ns gate that was applied to the APD circuit to bring it above the breakdown voltage and turn on the Geiger mode operation. There was an additional time delay of about 10 ns before the detector could produce the output pulses representing the arrival of an idler photon. The idler output pulse had a risetime of about 4 ns and length of about 8 ns. The delay τ_D was used to fine tune the gate timing with respect to the idler photon arrival time. A LabVIEW board and acquisition software was used to detect a positive-going threshold crossing of the generated pulse and record a time stamp for the risetime with a resolution of 2 ns.

These times were stored for later analysis.

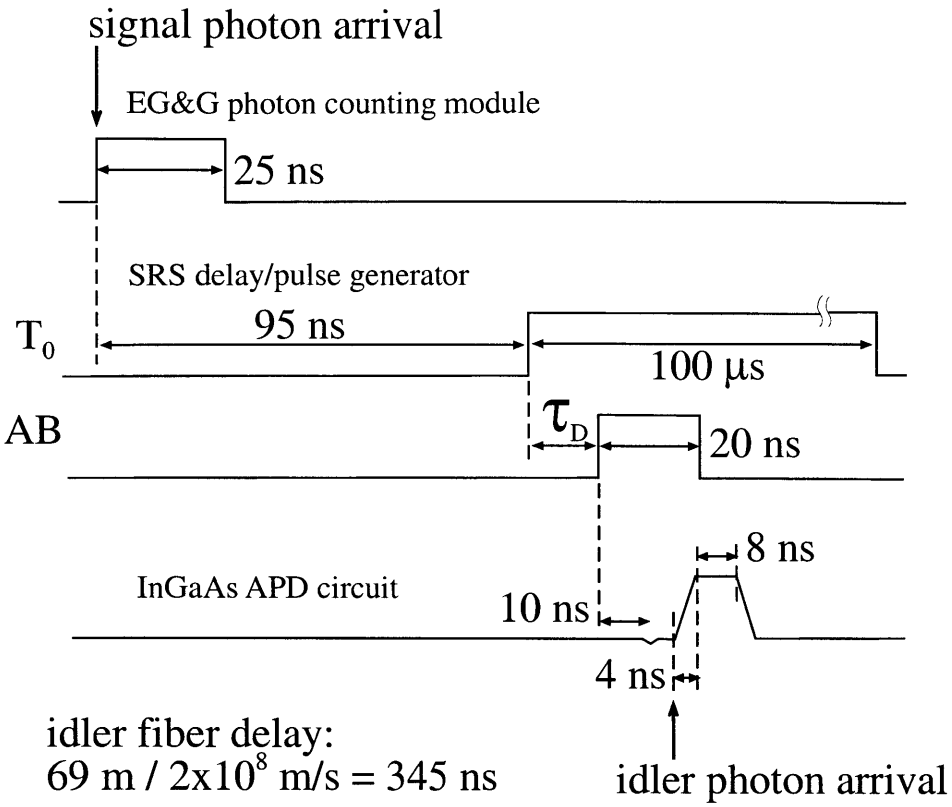

Figure 3-17: Timing of conditional coincidence counting.

Figure (3-18) shows the results in a histogram of time-stamps in 2-ns bins that has been normalized to give the probability of detecting a count (representing an idler photon arrival or a dark count) per gate. Since the device is passively quenched only one count can be generated per gate. So the probability of getting two or more photon arrivals per gate was made negligible by having a low enough pair generation rate. By adding the counts in two adjacent bins we calculate that the overall probability of detecting an idler photon given that a signal photon is detected is 3.1%. The counts in the other bins are dark counts and are also low enough to be neglected (<0.01%/ns). This measurement shows that the signal and idler photons were coincident to within a 4-ns window limited by the accuracy of the threshold crossing of a pulse with a 4-ns risetime and digitized to the nearest 2 ns.

The measured conditional detection probability of 3.1% is determined by the de-

tector quantum efficiency of ~21%, the propagation loss of ~15%, and the inferred fiber coupling efficiency of the idler mode that was matched to the signal mode of ~17%. We were able to collect the signal photons into the single-mode fiber and detect them at a rate of 30,000 counts/s/mW (with a detector quantum efficiency of 54%) normalized by pump power which was typically 1–2 mW. This number is much lower than the rate measured directly out of the crystal without the fiber due to fiber coupling efficiency and mode selection of the single-mode fiber. Using the conditional idler detection probability we can determine the effective rate of coincident photon pairs that would have been counted without the 10 kHz limit imposed by the idler photon counter; it is simply the product of the detected signal rate and the conditional idler coincidence probability: $30,000 \times 3.1\% = 930$ counts/s/mW.

We can now compare this figure of merit with what has been obtained in other high-efficiency entangled photon pair sources that use single-mode optical fiber for collection. In Kurtsiefer, *et al.* [58] a 2-mm-long BBO crystal was used and a maximum count rate of 360,800 counts/s was detected with a pump power of 465 mW. This yields a 776 counts/s/mW normalized rate. In the low power regime they obtained a normalized rate of 900 counts/s/mW. In another experiment Volz, *et al.* [59] used a pump-resonant scheme to obtain 1,231 pairs/s/mW. These experiments used frequency-degenerate photons that were near the detection peak of Si APDs (700 nm and 850 nm) giving a quantum efficiency in the range of 50–70%. While one of our wavelengths was in this range, the other was near 1600 nm where our InGaAs APD had a quantum efficiency of 20%. Correcting for this would yield a higher actual photon pair detection rate. We also have the potential for improvement by using a 1st-order grating and a longer crystal.

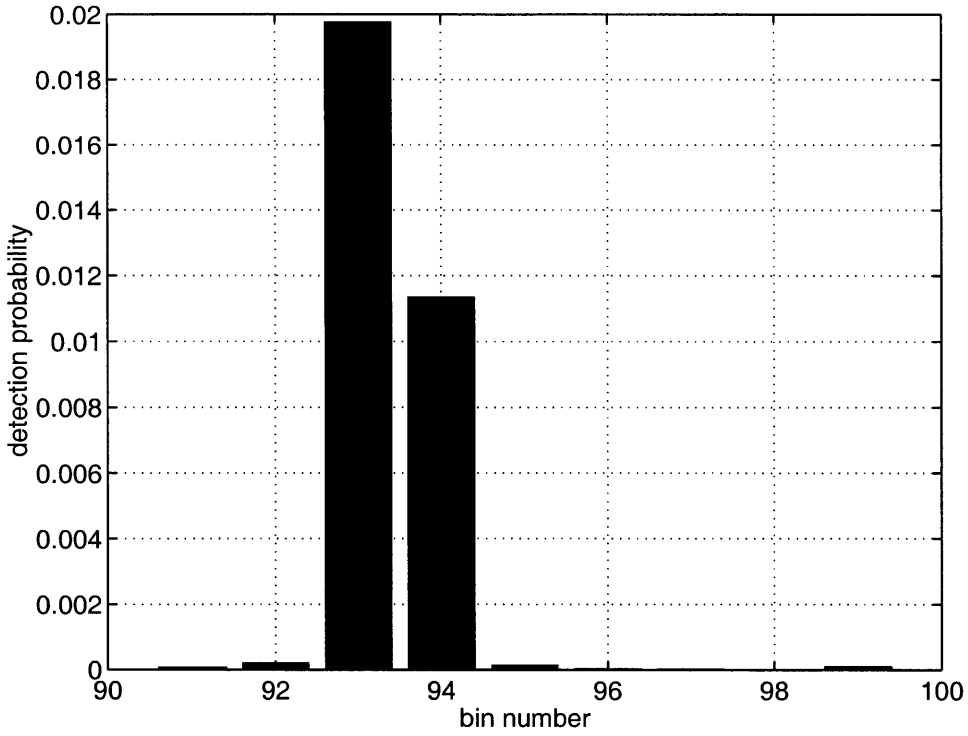

Figure 3-18: Conditional detection probability of idler photons given a signal photon is detected. Normalized histogram of counts in 2-ns time bins over a 20-ns window.

Chapter 4

Conclusion

4.1 Summary

In this thesis we first presented a theoretical model of self-phase locking in a type-II phase matched DRO. It described the linear coupling mechanism for the locking behavior and gave the steady-state solutions. In particular, the existence of two oscillation modes was indicated by the solutions and also observed in the experimental realization of the device. Details of the experiment were also presented along with the results of comparisons with the theoretical model.

A comprehensive description of procedures for fabrication of PPLN was then given with discussion of the various challenges and limitations. The details included the mask design and photolithography process as well as the electric-field poling of the crystals. One of the main results was the demonstration of periodic poling in the material BMF. A high-quality 3rd-order QPM grating with a period of 19.2 μm was fabricated. The advantages of periodically-poled BMF for use in UV and VUV generation were discussed.

Finally, a demonstration of the use of PPLN for high-efficiency generation of frequency-nondegenerate photon pairs was presented. Single-photon detection was performed at both downconverted wavelengths, 800 nm and 1600 nm using a conditional coincidence counting technique. High coincidence rates comparable to the best results published to date were achieved for photons coupled into single-mode fibers.

These results were obtained with a 3rd-order 2-cm-long PPLN crystal. Even higher rates are possible with 1st-order gratings and longer crystals.

4.2 Future Work

As described in section (1.3) the photon pair source demonstrated in this thesis is the first step towards the realization of a polarization-entangled photon pair source to be used for quantum teleportation. The signal and idler photons from our source are correlated in polarization. The photons exit from the crystal with the same polarization since type-I phase matching is used. The scheme for constructing a polarization-entangled source is based on a proposal by Shapiro and Wong [34] for creating polarization entanglement by combining the outputs from two coherently-pumped identical OPAs. In this proposed source, an optical cavity is used to create a narrowband output to increase the efficiency of subsequent coupling into the optical cavity of a trapped-atom quantum memory. To avoid associated timing uncertainty of a few reciprocal cavity linewidths that would affect our coincidence counting, we decided to use single-pass downconversion with a bandwidth determined by the phase matching. Since we are using type-I phase matching, our source will employ the same combining arrangement for the signal and idler outputs as described by Shapiro and Wong for two type-I phase-matched OPAs.

Before describing the polarization states produced by the source, we first point out that an arbitrary polarization state of a single photon can be expressed as a superposition $|\psi\rangle = \alpha|\uparrow\rangle + \beta|\bullet\rangle$ of two orthogonal polarization states $|\uparrow\rangle$ and $|\bullet\rangle$, where $|\alpha|^2 + |\beta|^2 = 1$. The goal of the combining arrangement is to produce two photons whose polarizations are completely random, but, given one photon is in a particular polarization state described by a complex-valued unit vector $\vec{i}$, then the other photon is in a conjugate polarization state $\vec{i}'$ with unit probability. Such a state can be produced using two coherently-pumped identical downconverters, combining the signal outputs in one polarization beam splitter (PBS), and the idler outputs in another PBS as illustrated in Fig. (4-1).

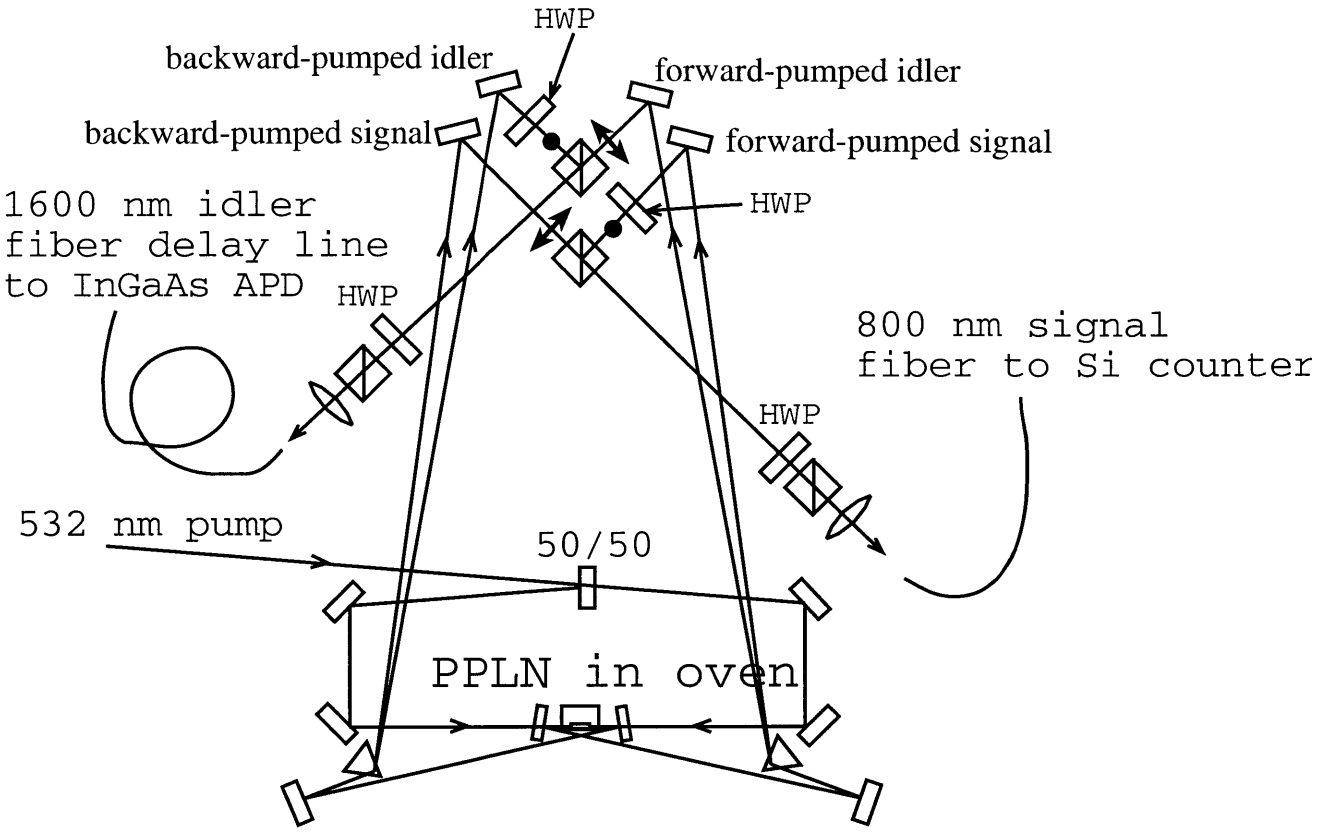

Figure 4-1: Dual coherently-pumped downconverter setup. The signal outputs are combined in one PBS and the idler outputs are combined in another PBS. Coincidence counting is performed as before, with HWPs and polarizers to project the outputs onto an arbitrary linear polarization basis.

One pump beam is split by a 50/50 beam splitter to coherently pump a single PPLN crystal in both the forward and backward directions. By overlapping the forward and backward pump beams the two downconverters have identical phase matching conditions. On each side the co-propagating signal and idler are separated by a prism. All four fields start with the identical polarization state $|\uparrow\rangle$. Before the beam paths are combined the polarization state of the forward-pumped signal and of the backward-pumped idler are rotated to the orthogonal polarization state $|\bullet\rangle$. When pumped with a low enough power a single photon pair is emitted in a superposition state. The joint state of the resulting signal (s subscript) and idler (i

subscript) pair is expressed by

$$|\psi\rangle_{si} = (|\uparrow\rangle_s|\bullet\rangle_i + e^{i\varphi}|\bullet\rangle_s|\uparrow\rangle_i)/\sqrt{2}$$

where φ is determined by the relative phase delays of the signal and idler optical paths at the combining PBSs. Before the outputs are coupled into their respective fibers, HWPs and polarizers are used to project the outputs onto an arbitrary linear polarization basis.

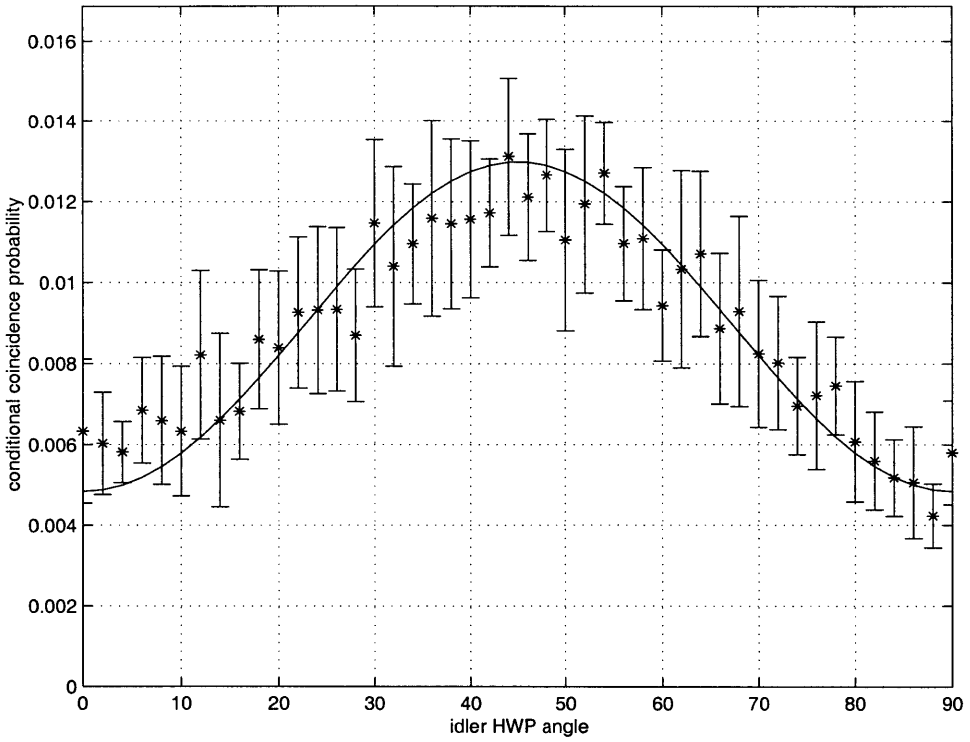

Figure 4-2: Conditional coincidence counts normalized to give the probability of detecting an idler photon, given a signal photon has been detected. Plotted for various HWP angles from 0° to 90°. The maximum value at a HWP angle of 45° corresponds to rotation of the idler polarization by 90° such that the orthogonal state is detected.

Initial coincidence measurements were performed using this setup. The data plotted in Fig. (4-2) show the conditional coincidence counts normalized to give the probability of detecting an idler photon, given a signal photon has been detected. The error bars indicate the standard deviation of the data that was collected at each

angle. The coincidences are plotted against the angle of the HWP in front of the idler polarizer. The HWP in front of the signal polarizer was fixed at an angle to rotate the two orthogonal states defined by the PBS by 45° with respect to the linear basis of the polarizer (each state will be passed with probability 1/2). The HWP in front of the idler was rotated in increments of 2° to look for changes in the coincidence probabilities. The minimum value of ~0.5% at a HWP angle of 0° and 90° correspond to detection in the linear polarization basis of the forward-pumped idler photons. The maximum value of ~1.3% at a HWP angle of 45° corresponds to detection in the linear polarization basis of the orthogonally-polarized backward-pumped idler photons. The fact that the forward-pumped and backward-pumped coincidence probabilities are different indicates that the two idler modes are not identically matched into the fiber or aligned to their respective signal modes.

This initial result shows that the data fit a sine function with a maximum at 45° and minima at 0° and 90° HWP settings. If the coincidence probabilities at other HWP angles were higher than the value at 45° or lower than the value at 0° and 90°, that would be an indication of coherent nonclassical combining of the forward-pumped and backward-pumped outputs, as needed for generation of polarization entanglement. This can be seen by looking at an expression of the average number of coincidences within coincidence time interval T over a measurement time interval T_M in terms of the signal and idler field operators $\hat{E}_s(t)$ and $\hat{E}_i(t)$

$$C(T) \propto T_M \int_{-T}^{T} |\langle \hat{E}_s(t+\tau)\hat{E}_i(t)\rangle|^2 d\tau,$$

where accidental coincidences have been subtracted out and coherent combining has been assumed. Since the signal field is projected onto a basis that is rotated 45° with respect to both the forward-pumped and backward-pumped outputs it is given by $\hat{E}_s(t) = (\hat{E}_{sF}(t) + e^{i\phi_s}\hat{E}_{sB}(t))/\sqrt{2}$. The idler field is projected onto a basis that is rotated with respect to the outputs by an angle 2θ where θ is the angle of the HWP as described in the experiment, and is given by $\hat{E}_i(t) = \hat{E}_{iF}(t)\cos(2\theta) + e^{i\phi_i}\hat{E}_{iB}(t)\sin(2\theta)$. As described above, there is a relative phase between the forward-

pumped and backward-pumped fields for both the signal (ϕ_s) and idler (ϕ_i). Under the assumption of coherent combining, these phases do not fluctuate during the measurement interval T_M, so that

$$C(T) \propto |\sqrt{C_F}\cos(2\theta) + e^{i(\phi_s+\phi_i)}\sqrt{C_B}\sin(2\theta)|^2$$

where C_F and C_B are the coincidence rates for idler detection along the linear basis of the forward-pumped or backward-pumped outputs. Here there is the possibility for a minimum value lower than $\min(C_F, C_B)$ and a maximum value higher than $\max(C_F, C_B)$, occurring at values of θ other than $\theta = 0, \pi/4, \pi/2$. On the other hand, if ϕ_s and ϕ_i fluctuate over the measurement interval, then the $\sqrt{C_F C_B}$ cross term in the preceding expression will be reduced. In the limit of incoherent combining, when this cross term averages to zero, we then find

$$C(T) \propto C_F\cos^2(2\theta) + C_B\sin^2(2\theta).$$

As seen in our experimental results, the incoherent combining limit has coincidence extrema at $\theta = 0, \pi/4, \pi/2$.

For future progress towards achieving a clear demonstration of polarization entanglement, various technical issues must be investigated and any potential problems must be corrected. One potential problem is the need to control the relative phases ϕ_s and ϕ_i such that the joint state of the pairs is stable over successive measurements. It may also be desirable to choose a particular value of $(\phi_s + \phi_i)$, such as 0 or π. This could be accomplished by using a phase modulator in one of the beam paths before the combining PBS. The relative phases could also potentially be made more stable by shortening the distance from the crystal to the PBSs with a more compact setup. The relative phase difference between the forward and backward pump fields also affects ϕ_s and ϕ_i, and efforts should be made to ensure that it is stable. Another issue that should be further investigated is the effect of unequal generation and collection efficiencies for the forward-pumped and backward-pumped outputs. With matched forward and backward pump powers the two generation rates should be the same.

In our setup the beam splitter ratio was 42/58 instead of 50/50. It was also evident that there were unequal collection efficiencies for the forward-pumped and backward-pumped signal photons since the backward-pumped output had a lower pump power, but a higher photon detection rate. A final comment on the steps to be taken to achieve a stable relative phase between the forward-pumped and backward-pumped paths is that it may be useful to investigate the classical interference between the intense field amplitudes obtained when the crystal is pumped with signal or idler inputs as an OPA [62]. Such a configuration could yield insight into the stability of the optical paths and the quality of the beam overlap on the combining PBSs.

Appendix A

Grating Mask Specification and Generation

This Appendix contains the code used to generate the photolithographic masks for the QPM gratings. The language used is AutoLisp. The code follows a specification with various parameters used to design the device features. Section (A.1) explains the basic layout of the mask and defines the design parameters as illustrated in Fig. (A-1). Section (A.2) contains all of the actual code including the mask specification files for the device and contact pad masks, and the libraries containing the drawing procedures and auxiliary subroutines.

A.1 Mask design parameters

Each QPM grating requires a complete pattern to be specified on a photolithographic mask which can be manufactured from various vendors. The 2-D pattern is usually required in a particular CAD format such as "DXF" or "gdsII". We have defined a set of parameters such as the period, width, and length of the QPM gratings, as well as the number of gratings and their positions on the mask. These parameters are entered into a "mask specification file" in the syntax of the AutoLisp language. This file is then used as input to the AutoCAD procedures which produce a DXF file that is suitable for manufacturing the mask.

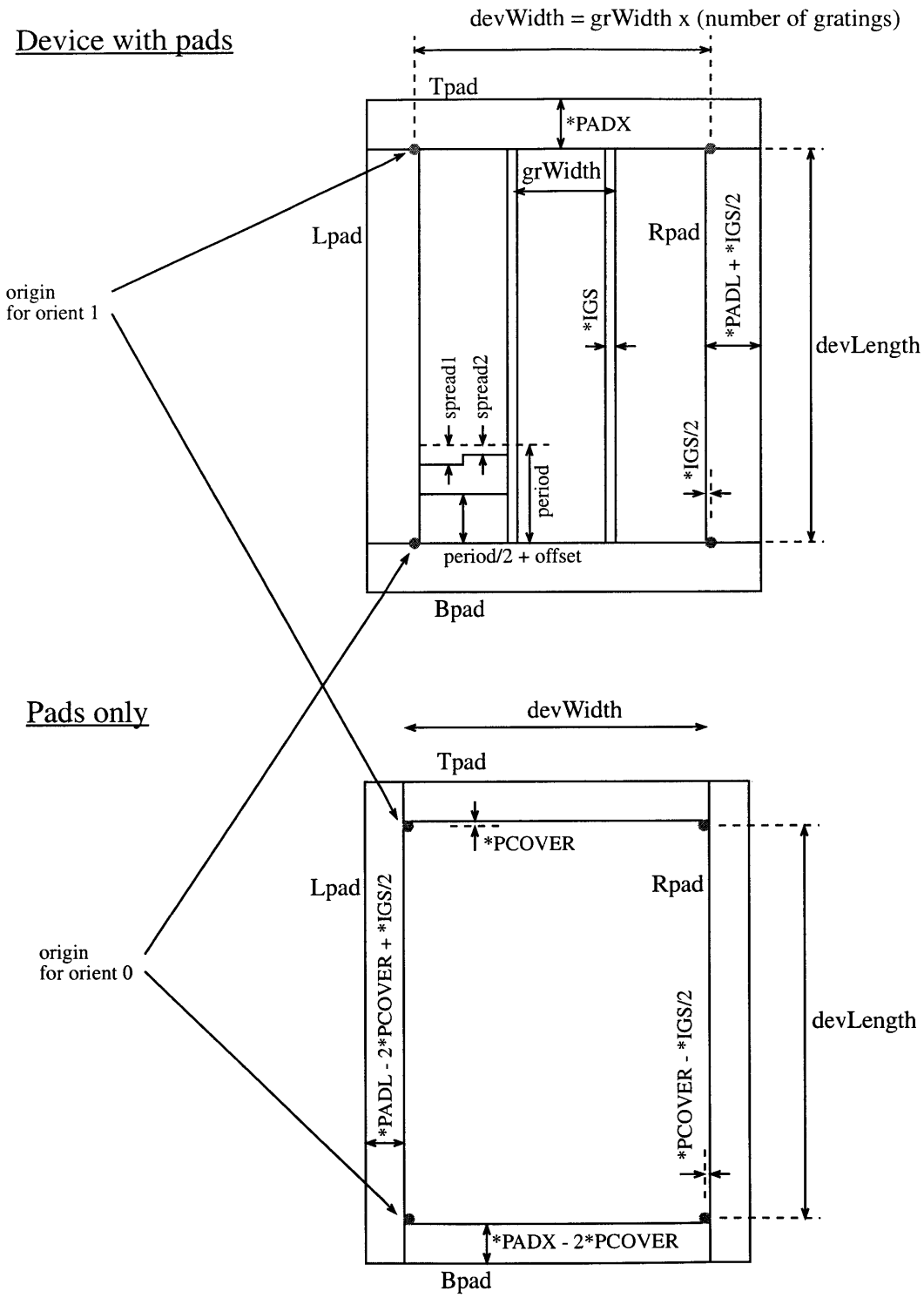

Figure A-1: Shown here are the definitions of the parameters specified when designing a QPM grating device with contact pads, and the corresponding device with contact pads only.

A mask can contain several QPM grating "devices." Each device can contain several "gratings" that have the same or different periods arranged side by side. There is also an option to make one grating have two "sections" with different periods. Each device has associated with it a pair of coordinates specifying its location on the mask. All sizes are given in units of μm. Figure (A-1) shows all of the elements of the 2-D pattern that have to be drawn on the mask. A typical device with three gratings is illustrated under the heading "Device with pads." Since this constitutes a device that would be patterned onto a crystal substrate and poled it has contact pads surrounding it.

The drawing procedures are written in terms of a global mask coordinate system and a local device coordinate system. To facilitate switching between the two, each device has a well-defined local "origin." Since the device may be oriented horizontally or vertically on the mask, there are two possible locations for the origin of the device. The origin is always in the lower left corner, so it is specified for both the vertical orientation "orient 0," and the horizontal orientation "orient 1."

Everything on the mask is drawn as non-overlapping closed polygons, where the area inside the polygon is clear on the mask. All other areas of the mask are opaque. The figure only illustrates one of the teeth that make up the grating itself. There is a step in it that corresponds to the option of making an arbitrary number of adjacent duty cycles. Under the heading "Pads only" is the pattern that is used on a separate mask which is used for the contact pad photolithography step mentioned in the procedure. It consists of four rectangles as shown.

A.2 AutoLisp Code

This section contains the actual AutoLisp code that is run by AutoCAD to generate the DXF file used to manufacture the mask. The mask specification files contain the parameters defined above. The other "code libraries" are separate collections of procedures that perform various tasks as described below. In addition to brief summaries of the contents of each code library, the code itself has comments (preceded

by one or more semicolons) that indicate the functions performed by the procedures.

A.2.1 Mask specification files

The following is the file for 3rd-order QPM devices that were used in the experiments of this thesis. There are seven devices consisting of gratings of various periods and duty cycles. In addition to the specification of the devices, the main command-line procedure that is called to initiate all of the tasks performed by the code is defined here. The instructions for loading the code libraries and issuing the command in AutoCAD are included in the comments.

```
;;;  Grating mask: QPM-VI (filename: mqpm6.lsp)
;;;  This file loads all needed subroutines.
;;;
;;;  To make a new grating mask specification file edit this .lsp file
;;;  and save it with a new name
;;;
;;;  To load this file in autocad type: (load "~/autocad/mqpm6")
;;;  To draw mask type at the command line: drawmask
;;;

(load "~/autocad/msetup") ;global variable stuff
(load "~/autocad/mdrdev") ;main draw routines
(load "~/autocad/mutils") ;utility functions
(load "~/autocad/marea")  ; versions of mdrdev routines that don't draw
  ; (find area only)

;;;;;;;;;;;;;;;;;;;;;;;;;;;;;;;;;;;;;;;;;;;;;;;;
;;;  Enter mask specifications:     ;;;
;;;;;;;;;;;;;;;;;;;;;;;;;;;;;;;;;;;;;;;;;;;;;;;;

;;; all locations are specified by a dotted pair which represents
;;; x and y coordinates in microns with respect to the lower left
;;; corner of the mask (origin). Up and right are positive. Down
;;; and left are negative.

;; Define total mask working area:
(setq *MASKX 80000.0 *MASKY 80000.0)

;; Define global offsets added to every point drawn:
```

```
(setq *HOFFSET 0.0 *VOFFSET 0.0)

;; Enter inter-grating space:
(setq *IGS 50.0)

;; Enter the width of the contact pads along/across the gratings:
(setq *PADL 1000.0 *PADX 1000.0)

;; Enter the width of contact pad edge covering:
(setq *PCOVER 100.0)

;; Enter space between contact pad and "division" mark
;; and "radius" of square
(setq *DIVSPACE 500.0 *DIVSIZE 250.0)

;; Enter target duty cycle
;; (only affects calculated device area,
;; not "spread" values which assumes 50% target duty cycle)
(setq *DC 0.5)

;;;;;;;;;;;;;;;;;;;;;;;;;;;;;;;;;;;;;;;;;;;;
;;;  Enter device specifications:  ;;;
;;;;;;;;;;;;;;;;;;;;;;;;;;;;;;;;;;;;;;;;;;;;

;; The gobal constant *DEVICES is a list containing all device specs:
;; each element in *DEVICES is a list of specs for a particular device:
;; -dotted pair representing the location on mask
;;  of lower left corner of device
;; -decimal representing length of device
;; -list of grating spec lists containing:
;;  -decimal representing width of grating plus 1 full *IGS space
;;  -period or for a double grating
;;   a list of 2 periods and ratio of 1st to whole
;;   (if the period itself is a list the the second number
;;   is an offest for the bottom of the grating line)
;;  -list of spreading compensation amounts in increasing order
;;   (still a list even if there is only one amount;
;;   a list of two lists if there are two periods)
;; -0 or 1 for grating orientation along y or x

(setq *DEVICES
  '( ((27500.0 . 66000.0) 25000.0
      ((2000.0 21.6 (2.1)) (2000.0 21.6 (2.1)) (2000.0 21.6 (2.1))
       (2000.0 21.6 (2.1)) (2000.0 21.6 (2.1)) (2000.0 21.6 (2.1))) 1)
 ((27500.0 . 50000.0) 25000.0
```

```
  ((2000.0 21.6 (4.3)) (2000.0 21.6 (4.3)) (2000.0 21.6 (4.3))
   (2000.0 21.6 (4.3)) (2000.0 21.6 (4.3)) (2000.0 21.6 (4.3))) 1)
 ((27500.0 . 34000.0) 25000.0
  ((2000.0 (22.1 0.05) (2.1)) (2000.0 (22.1 0.05) (2.1))
   (2000.0 (22.1 0.05) (2.1)) (2000.0 (22.1 0.05) (2.1))
   (2000.0 (22.1 0.05) (2.1)) (2000.0 (22.1 0.05) (2.1))) 1)
 ((27500.0 . 18000.0) 25000.0
  ((2000.0 (22.1 0.05) (4.4)) (2000.0 (22.1 0.05) (4.4))
   (2000.0 (22.1 0.05) (4.4)) (2000.0 (22.1 0.05) (4.4))
   (2000.0 (22.1 0.05) (4.4)) (2000.0 (22.1 0.05) (4.4))) 1)
 ((27500.0 . 2000.0) 25000.0
  ((2000.0 22.4 (6.2)) (2000.0 22.4 (6.2)) (2000.0 22.4 (6.2))
   (2000.0 22.4 (6.2)) (2000.0 22.4 (6.2)) (2000.0 22.4 (6.2))) 1)
 ((10000.0 . 23000.0) 34000.0
  ((2000.0 22.4 (2.2)) (2000.0 22.4 (2.2)) (2000.0 22.4 (2.2))
   (2000.0 22.4 (2.2)) (2000.0 22.4 (2.2)) (2000.0 22.4 (2.2))) 0)
 ((58000.0 . 23000.0) 34000.0
  ((2000.0 22.4 (4.5)) (2000.0 22.4 (4.5)) (2000.0 22.4 (4.5))
   (2000.0 22.4 (4.5)) (2000.0 22.4 (4.5)) (2000.0 22.4 (4.5))) 0) ))

;;;;;;;;;;;;;;;;;;;;;;;;;;;;;;;;;;;;;;;;;;;;;;;;;;;;;;;;;;;;;;;;;;;;;;;
;;;  End of inputs
;;;;;;;;;;;;;;;;;;;;;;;;;;;;;;;;;;;;;;;;;;;;;;;;;;;;;;;;;;;;;;;;;;;;;;;


;;;;;;;;;;;;;;;;;;;;;;;;;;;;;;;;;;;;;;;;;;;;;;;;
;;;
;;;  Send inputs to drawing subroutines:
;;;
;;;;;;;;;;;;;;;;;;;;;;;;;;;;;;;;;;;;;;;;;;;;;;;;

(defun c:drawmask ()
  (m:setup)
  (ma:pads 0) ; m:pads to draw, ma:pads to calculate area only
  (ma:gratings) ; m:gratings to draw, ma:gratings to calculate area only
  (ma:finnish)) ; m:finnish to draw, ma:finnish to calculate area only

(setq all "~/autocad/mqpm6")

(princ "\n all files loaded for mqpm6.lsp")
(prin1)
```

The following is the file for the contact pad mask associated with the device mask above. There are only contact pad patterns on this mask corresponding to the two

different sizes of devices on the device mask.

```
;;;  Grating mask: QPM-V (filename: mqpm6p.lsp)
;;;  This file loads all needed subroutines.
;;;
;;;  To make a new grating mask specification file edit this .lsp file
;;;  and save it with a new name
;;;
;;;  To load this file in autocad type: (load "~/autocad/mqpm6p")
;;;  To draw mask type at the command line: drawpads
;;;

(load "~/autocad/msetup") ;global variable stuff
(load "~/autocad/mdrdev") ;main draw routines
(load "~/autocad/mutils") ;utility functions

;;;;;;;;;;;;;;;;;;;;;;;;;;;;;;;;;;;;;;;;;;;;;;;
;;;  Enter mask specifications:     ;;;
;;;;;;;;;;;;;;;;;;;;;;;;;;;;;;;;;;;;;;;;;;;;;;;

;;; all locations are specified by a dotted pair which represents
;;; x and y coordinates in microns with respect to the lower left
;;; corner of the mask (origin). Up and right are positive. Down
;;; and left are negative.

;; Define total mask working area:
(setq *MASKX 80000.0 *MASKY 80000.0)

;; Define global offsets added to every point drawn:
(setq *HOFFSET 0.0 *VOFFSET 0.0)

;; Enter inter-grating space:
(setq *IGS 50.0)

;; Enter the width of the contact pads along/across the gratings:
(setq *PADL 1000.0 *PADX 1000.0)

;; Enter the width of contact pad edge covering:
(setq *PCOVER 100.0)

;; Enter space between contact pad and "division" mark
;; and "radius" of square
(setq *DIVSPACE 500.0 *DIVSIZE 250.0)
```

```
;;;;;;;;;;;;;;;;;;;;;;;;;;;;;;;;;;;;;;;;;;;;
;;;  Enter device specifications:  ;;;
;;;;;;;;;;;;;;;;;;;;;;;;;;;;;;;;;;;;;;;;;;;;

(setq *DEVICES
  '( ((34000.0 . 6000.0) 25000.0 ((12000.0 22.4 (2.2))) 0)
 ((34000.0 . 40000.0) 34000.0 ((12000.0 22.4 (6.2))) 0) ))

;;;;;;;;;;;;;;;;;;;;;;;;;;;;;;;;;;;;;;;;;;;;;;;;;;;;;;;;;;;;;;;;;;;;;;;;;;;;;;;
;;;  End of inputs
;;;;;;;;;;;;;;;;;;;;;;;;;;;;;;;;;;;;;;;;;;;;;;;;;;;;;;;;;;;;;;;;;;;;;;;;;;;;;;;


;;;;;;;;;;;;;;;;;;;;;;;;;;;;;;;;;;;;;;;;;;;;
;;;
;;;  Send inputs to drawing subroutines:
;;;
;;;;;;;;;;;;;;;;;;;;;;;;;;;;;;;;;;;;;;;;;;;;


(defun c:drawpads ( / point ul ur ll lr)
  (m:pads 1))

(setq all "~/autocad/mqpm6p")

(princ "\n all files loaded for mqpm6p.lsp")
(prin1)
```

A.2.2 Setup code library

The convention used in this code for global variables is that they have a name starting with an asterisk (e.g. *NAME). Most are defined in the mask specification file. The setup code library contains some global variable definitions as well as subroutines to find values and initial reference points that are either defined as global variables or are computed from global variables.

```
;; Initialize area totals and double grating division marks:
(defun m:setup ( / indx devList devWidth devLength initArea)
  (setq *AREAS (alist 0.0 (length *DEVICES)))
```

```
  (setq *DIVISIONS (alist 0.0 (length *DEVICES))))

;; modify AREAS and DIVISIONS

(defun areaAdd (devNum area / old new)
  (setq old (assoc devNum *AREAS)
new (list devNum (+ (cadr old) area)))
  (setq *AREAS (subst new old *AREAS)))

(defun divMark (devNum location / old new)
  (setq old (assoc devNum *DIVISIONS)
new (list devNum location))
  (setq *DIVISIONS (subst new old *DIVISIONS)))

;; getters for *DEVICES

(defun getOrigin (devList)
  (nth 0 devList))

(defun getDevLength (devList)
  (nth 1 devList))

(defun getGrts (devList)
  (nth 2 devList))

(defun getOrient (devList)
  (nth 3 devList))

(defun getDevWidth (devList / indx width grts grt)
  (setq width 0)
  (setq grts (getGrts devList))
  (setq indx 0)
  (while (< indx (length grts))
    (setq grt (nth indx grts))
    (setq width (+ width (nth 0 grt)))
    (setq indx (1+ indx)))
  (+ width 0))

(defun getGrWidth (grt)
  (nth 0 grt))

(defun getPeriod (grt)
  (nth 1 grt))

(defun getSpread (grt)
```

```
  (nth 2 grt))

;; find contact pad vertices:

(defun find00 (origin devLength devWidth /
       Rul Rur Rlr Rll Lul Lur Llr Lll Tul Tur Tlr Tll Bul Bur Blr Bll)
  (setq Llr (horAdd origin (/ *IGS 2)))
  (setq Lur (vertAdd Llr devLength))
  (setq Lll (horAdd origin (- *PADL)))
  (setq Lul (vertAdd Lll devLength))
  (setq Tll Lul)
  (setq Bul Lll)
  (setq Tul (vertAdd Tll *PADX))
  (setq Bll (vertAdd Bul (- *PADX)))
  (setq Tur (horAdd Tul (+ devWidth (* 2 *PADL))))
  (setq Blr (horAdd Bll (+ devWidth (* 2 *PADL))))
  (setq Tlr (vertAdd Tur (- *PADX)))
  (setq Bur (vertAdd Blr *PADX))
  (setq Rur Tlr)
  (setq Rlr Bur)
  (setq Rll (horAdd origin (- devWidth (/ *IGS 2))))
  (setq Rul (vertAdd Rll devLength))
  (list (list Rul Rur Rlr Rll)
(list Lul Lur Llr Lll)
(list Tul Tur Tlr Tll)
(list Bul Bur Blr Bll)))

(defun find10 (origin devLength devWidth /
       Rul Rur Rlr Rll Lul Lur Llr Lll Tul Tur Tlr Tll Bul Bur Blr Bll)
  (setq Lul (vertAdd origin (/ *IGS 2)))
  (setq Lur (horAdd Lul devLength))
  (setq Lll (vertAdd origin (- *PADL)))
  (setq Llr (horAdd Lll devLength))
  (setq Tlr Lll)
  (setq Bll Llr)
  (setq Tll (horAdd Tlr (- *PADX)))
  (setq Blr (horAdd Bll *PADX))
  (setq Tul (vertAdd Tll (+ devWidth (* 2 *PADL))))
  (setq Bur (vertAdd Blr (+ devWidth (* 2 *PADL))))
  (setq Tur (horAdd Tul *PADX))
  (setq Bul (horAdd Bur (- *PADX)))
  (setq Rul Tur)
  (setq Rur Bul)
  (setq Rll (vertAdd origin (- devWidth (/ *IGS 2))))
  (setq Rlr (horAdd Rll devLength))
```

```
  (list (list Rul Rur Rlr Rll)
(list Lul Lur Llr Lll)
(list Tul Tur Tlr Tll)
(list Bul Bur Blr Bll)))

(defun find01 (origin devLength devWidth /
       Rul Rur Rlr Rll Lul Lur Llr Lll Tul Tur Tlr Tll Bul Bur Blr Bll)
  (setq Bul (horAdd (vertAdd origin (- *PCOVER)) (- (/ *IGS 2) *PCOVER)))
  (setq Tll (vertAdd Bul (+ devLength (* *PCOVER 2))))
  (setq Bur (horAdd Bul (+ devWidth (* *PCOVER 2) (- *IGS))))
  (setq Tlr (horAdd Tll (+ devWidth (* *PCOVER 2) (- *IGS))))
  (setq Bll (vertAdd Bul (- (* *PCOVER 2) *PADX)))
  (setq Blr (vertAdd Bur (- (* *PCOVER 2) *PADX)))
  (setq Tul (vertAdd Tll (- *PADX (* *PCOVER 2))))
  (setq Tur (vertAdd Tlr (- *PADX (* *PCOVER 2))))
  (setq Lur Tul)
  (setq Rul Tur)
  (setq Llr Bll)
  (setq Rll Blr)
  (setq Lul (horAdd Lur (- (* *PCOVER 2) (+ *PADL (/ *IGS 2)))))
  (setq Rur (horAdd Rul (- (+ *PADL (/ *IGS 2)) (* *PCOVER 2))))
  (setq Lll (horAdd Llr (- (* *PCOVER 2) (+ *PADL (/ *IGS 2)))))
  (setq Rlr (horAdd Rll (- (+ *PADL (/ *IGS 2)) (* *PCOVER 2))))
  (list (list Rul Rur Rlr Rll)
(list Lul Lur Llr Lll)
(list Tul Tur Tlr Tll)
(list Bul Bur Blr Bll)))

(defun find11 (origin devLength devWidth /
       Rul Rur Rlr Rll Lul Lur Llr Lll Tul Tur Tlr Tll Bul Bur Blr Bll)
  (setq Tlr (vertAdd (horAdd origin (- *PCOVER)) (- (/ *IGS 2) *PCOVER)))
  (setq Bll (horAdd Tlr (+ devLength (* *PCOVER 2))))
  (setq Tur (vertAdd Tlr (+ devWidth (* *PCOVER 2) (- *IGS))))
  (setq Bul (vertAdd Bll (+ devWidth (* *PCOVER 2) (- *IGS))))
  (setq Tul (horAdd Tur (- (* *PCOVER 2) *PADX)))
  (setq Tll (horAdd Tlr (- (* *PCOVER 2) *PADX)))
  (setq Bur (horAdd Bul (- *PADX (* *PCOVER 2))))
  (setq Blr (horAdd Bll (- *PADX (* *PCOVER 2))))
  (setq Rll Tul)
  (setq Rlr Bur)
  (setq Lul Tll)
  (setq Lur Blr)
  (setq Lll (vertAdd Lul (- (* *PCOVER 2) (+ *PADL (/ *IGS 2)))))
  (setq Rul (vertAdd Rll (- (+ *PADL (/ *IGS 2)) (* *PCOVER 2))))
  (setq Llr (vertAdd Lur (- (* *PCOVER 2) (+ *PADL (/ *IGS 2)))))
```

```
  (setq Rur (vertAdd Rlr (- (+ *PADL (/ *IGS 2)) (* *PCOVER 2))))
  (list (list Rul Rur Rlr Rll)
(list Lul Lur Llr Lll)
(list Tul Tur Tlr Tll)
(list Bul Bur Blr Bll)))

;; find vertices and area of grating line:
(defun findVerts (offset orient side1 side2 current period spread /
       indx spread1 spread2 loc verts area)
  (setq area (* (* period *DC) (- side2 side1 *IGS)))
  (cond ((= orient 0)
 (setq verts (list (cons (+ side1 (/ *IGS 2))
 (+ current period (- (nth 0  spread))))))
 (setq indx 1)
 (while (< indx (length spread))
   (setq loc
 (+ side1
    (/ *IGS 2)
    (* indx
       (round (/ (- side2 side1 *IGS) (length spread)))))
 spread1 (nth (1- indx) spread)
 spread2 (nth indx spread))
   (setq verts
 (append verts
 (list (cons loc (+ current period (- spread1)))
       (cons loc (+ current period (- spread2))))))
   (setq indx (1+ indx)))
 (setq verts
       (append verts
       (list (cons (- side2 (/ *IGS 2))
   (+ current period (- (last spread))))
     (cons (- side2 (/ *IGS 2))
   (+ current offset (/ period 2))))))
 (setq verts
       (append verts
       (list (cons (+ side1 (/ *IGS 2))
   (+ current offset (/ period 2))))))
 (setq verts
       (append verts
       (list (cons (+ side1 (/ *IGS 2))
   (+ current period (- (nth 0 spread)))))))
 (list verts area))
((= orient 1)
 (setq verts
       (list (cons (+ current period (- (nth 0 spread)))
```

```
  (- side2 (/ *IGS 2)))))
 (setq indx 1)
 (while (< indx (length spread))
   (setq loc
 (- side2 (/ *IGS 2) (* indx (round (/ (- side2 side1 *IGS)
       (length spread)))))
 spread1 (nth (1- indx) spread)
 spread2 (nth indx spread))
   (setq verts
 (append verts
 (list (cons (+ current period (- spread1)) loc)
       (cons (+ current period (- spread2)) loc))))
   (setq indx (1+ indx)))
 (setq verts
       (append verts
       (list (cons (+ current period (- (last spread)))
   (+ side1 (/ *IGS 2)))
     (cons (+ current offset (/ period 2))
   (+ side1 (/ *IGS 2))))))
 (setq verts
       (append verts
       (list (cons (+ current offset (/ period 2))
   (- side2 (/ *IGS 2))))))
 (setq verts
       (append verts
       (list (cons (+ current period (- (nth 0 spread)))
   (- side2 (/ *IGS 2))))))
 (list verts area))))

(defun round (num)
  (/ (fix (* num 10)) 10))

(princ "\n msetup loaded")
```

A.2.3 Device drawing code library

The device drawing code library contains the main procedures that draw the actual grating teeth as well as the contact pads and contact strips. The procedures called by the initial command-line procedure are defined here.

```
;;; routines to draw gratings, contact pads, contact strips;
```

```
;;; and draw double grating marks, do contact area
;;; calculation and any other finnishing tasks

;; draw outer contact pads
;; for device mask if flag is 0,
;; for contact pad mask if flag is 1
(defun m:pads (flag / indx devList devWidth devLength orient origin pads)
  (setq indx 0)
  (while (< indx (length *DEVICES))
    (setq devList (nth indx *DEVICES))
    (setq devWidth (getDevWidth devList))
    (setq devLength (getDevLength devList))
    (setq origin (getOrigin devList))
    (setq orient (getOrient devList))
    (cond ((and (= orient 0) (= flag 0))
   (setq pads (find00 origin devLength devWidth)))
  ((and (= orient 1) (= flag 0))
   (setq pads (find10 origin devLength devWidth)))
  ((and (= orient 0) (= flag 1))
   (setq pads (find01 origin devLength devWidth)))
    ((and (= orient 1) (= flag 1))
     (setq pads (find11 origin devLength devWidth))))
    (m:draw (nth 0 pads))
    (m:draw (nth 1 pads))
    (m:draw (nth 2 pads))
    (m:draw (nth 3 pads))
    (if (= flag 0)
(areaAdd indx (padsArea pads)))
    (setq indx (1+ indx)))
  (prin1))

;; draw inner contact strips and gratings
(defun m:gratings ( / indx1 indx2 devList grts devLength origin orient
  grt width period spread topL topR bottomL bottomR)
  (setq indx1 0)
  (while (< indx1 (length *DEVICES))
    (print (list "...drawing device" (1+ indx1)))
    (setq devList (nth indx1 *DEVICES))
    (setq grts (getGrts devList))
    (setq devLength (getDevLength devList))
    (setq origin (getOrigin devList))
    (setq orient (getOrient devList))
    (cond ((= orient 0)
   (setq bottomL origin
 topL (vertAdd origin devLength)))
```

```
  ((= orient 1)
   (setq bottomL origin
 bottomR (horAdd origin devLength))))
    (setq indx2 0)
    (while (< indx2 (length grts))
      (setq grt (nth indx2 grts))
      (setq width (getGrWidth grt))
      (setq period (getPeriod grt))
      (setq spread (getSpread grt))
      (cond ((= orient 0)
     (setq bottomR (horAdd bottomL width)
   topR (horAdd topL width)))
    ((= orient 1)
     (setq topL (vertAdd bottomL width)
   topR (vertAdd bottomR width))))
       (drawGrt indx1 topL topR bottomL bottomR period spread orient)
      (if (< indx2 (1- (length grts)))
  (drawStrip indx1 topL topR bottomL bottomR orient))
       (cond ((= orient 0)
      (setq bottomL bottomR
   topL topR))
     ((= orient 1)
      (setq bottomL topL
   bottomR topR)))
       (setq indx2 (1+ indx2)))
    (setq indx1 (1+ indx1)))
  (prin1))

(defun m:finnish ( / indx devList)
  (setq indx 0)
  (while (< indx (length *DEVICES))
    (setq devList (nth indx *DEVICES))
    (setq devWidth (getDevWidth devList))
    (setq devLength (getDevLength devList))
    (setq origin (getOrigin devList))
    (setq orient (getOrient devList))
    (setq location (cadr (assoc indx *DIVISIONS)))
    (if (/= location 0.0)
(drawDivision origin devWidth devLength location orient))
    (print (* 1e-8 (cadr (assoc indx *AREAS))))
    (setq indx (1+ indx))))


%%%%%%%%%%
% other procedures that invoke the m:draw procedure:
```

```
% drawGrt, drawStrip, drawDivision
%%%%%%%%%%

(defun drawGrt (devNum topL topR bottomL bottomR period spread orient)
  (if (listp period)
      (if (= (length period) 3)
     (drawDouble devNum topL topR bottomL bottomR period spread orient)
  (drawSingle devNum topL topR bottomL bottomR period spread orient))
      (drawSingle devNum topL topR bottomL bottomR period spread orient)))

(defun drawSingle (devNum topL topR bottomL bottomR period spread orient /
   period0 offset spaceLeft current verts vertices vArea)
  (setq period0 (nth 0 (getPerOff period)))
  (setq offset (nth 1 (getPerOff period)))
  (cond ((= orient 0)
 (setq spaceLeft (- (cdr topL) (cdr bottomL)))
 (setq current (cdr bottomL))
 (while (> spaceLeft period0)
   (setq verts (findVerts offset 0 (car bottomL) (car bottomR)
    current period0 spread))
   (setq vertices (nth 0 verts)
 vArea (nth 1 verts))
   (areaAdd devNum vArea)
   (m:draw vertices)
   (setq spaceLeft (- spaceLeft period0))
   (setq current (+ current period0))))
((= orient 1)
 (setq spaceLeft (- (car topR) (car topL)))
 (setq current (car topL))
 (while (> spaceLeft period0)
   (setq verts (findVerts offset 1 (cdr bottomL) (cdr topL)
    current period0 spread))
   (setq vertices (nth 0 verts)
 vArea (nth 1 verts))
   (areaAdd devNum vArea)
   (m:draw vertices)
   (setq spaceLeft (- spaceLeft period0))
   (setq current (+ current period0))))))

(defun drawDouble (devNum topL topR bottomL bottomR period spread orient /
   offset1 offset2 spaceLeft current verts vertices vArea
   period1 period2 spread1 spread2 Pratio)
  (setq period1 (nth 0 (getPerOff (nth 0 period)))
   period2 (nth 0 (getPerOff (nth 1 period)))
offset1 (nth 1 (getPerOff (nth 0 period)))
```

```
offset2 (nth 1 (getPerOff (nth 1 period)))
spread1 (nth 0 spread)
spread2 (nth 1 spread)
Pratio (nth 2 period))
  (cond ((= orient 0)
 (setq spaceLeft (* (- (cdr topL) (cdr bottomL)) Pratio))
 (setq current (cdr bottomL))
 (while (> spaceLeft period1)
   (setq verts (findVerts offset1 0 (car bottomL) (car bottomR)
    current period1 spread1))
   (setq vertices (nth 0 verts)
 vArea (nth 1 verts))
   (areaAdd devNum vArea)
   (m:draw vertices)
   (setq spaceLeft (- spaceLeft period1))
   (setq current (+ current period1)))
 (setq spaceLeft (- (cdr topL) current))
 (divMark devNum current)
 (while (> spaceLeft period2)
   (setq verts (findVerts offset2 0 (car bottomL) (car bottomR)
    current period2 spread2))
   (setq vertices (nth 0 verts)
 vArea (nth 1 verts))
   (areaAdd devNum vArea)
   (m:draw vertices)
   (setq spaceLeft (- spaceLeft period2))
   (setq current (+ current period2))))
((= orient 1)
 (setq spaceLeft (* (- (car topR) (car topL)) Pratio))
 (setq current (car topL))
 (while (> spaceLeft period1)
   (setq verts (findVerts offset1 1 (cdr bottomL) (cdr topL)
    current period1 spread1))
   (setq vertices (nth 0 verts)
 vArea (nth 1 verts))
   (areaAdd devNum vArea)
   (m:draw vertices)
   (setq spaceLeft (- spaceLeft period1))
   (setq current (+ current period1)))
 (setq spaceLeft (- (car topR) current))
 (divMark devNum current)
 (while (> spaceLeft period2)
   (setq verts (findVerts offset2 1 (cdr bottomL) (cdr topL)
    current period2 spread2))
   (setq vertices (nth 0 verts)
```

```
 vArea (nth 1 verts))
   (areaAdd devNum vArea)
   (m:draw vertices)
   (setq spaceLeft (- spaceLeft period2))
   (setq current (+ current period2))))))

(defun getPerOff (period / output)
  (if (not (listp period))
  (if (> (- (* 10 (/ period 2))
   (fix (+ 0.0001 (* 10 (/ period 2))))) 0.000001)
          (setq output (list period 0.05))
         (setq output (list period 0.0)))
      (setq output (list (nth 0 period) (nth 1 period)))))

(defun drawStrip (devNum topL topR bottomL bottomR orient / vertices)
  (cond ((= orient 0)
 (setq vertices (list (horAdd topR (- (/ *IGS 2)))
    (horAdd topR (/ *IGS 2))
    (horAdd bottomR (/ *IGS 2))
    (horAdd bottomR (- (/ *IGS 2)))))
 (areaAdd devNum (* *IGS (- (cdr topL) (cdr bottomL))))
 (m:draw vertices))
((= orient 1)
 (setq vertices (list (vertAdd topL (- (/ *IGS 2)))
    (vertAdd topL (/ *IGS 2))
    (vertAdd topR (/ *IGS 2))
    (vertAdd topR (- (/ *IGS 2)))))
 (areaAdd devNum (* *IGS (- (car topR) (car topL))))
 (m:draw vertices))))

(defun drawDivision (origin devWidth devLength location orient /
 left right upper lower)
  (cond ((= orient 0)
 (setq left (cons (- (- (car origin) *PADL) *DIVSPACE) location)
       right (cons (+ (+ (car origin) *PADL devWidth) *DIVSPACE) location))
 (makeMark 0 left)
 (makeMark 0 right))
((= orient 1)
 (setq upper (cons location (+ (+ (cdr origin) *PADL devWidth) *DIVSPACE))
       lower (cons location (- (- (cdr origin) *PADL) *DIVSPACE)))
 (makeMark 0 upper)
 (makeMark 0 lower))))

; to make different types of marks centered at a point
(defun makeMark (tag point)
```

```
  (cond ((= tag 0) (drawMarkD point))
((= tag 1) (+ 0 0))    ; dummy type
((= tag 2) (+ 0 0)))) ; dymmy type

(defun drawMarkD (point / ul ur ll lr)
  (setq ul (horAdd (vertAdd point *DIVSIZE) (- *DIVSIZE)))
  (setq ur (horAdd (vertAdd point *DIVSIZE) *DIVSIZE))
  (setq ll (horAdd (vertAdd point (- *DIVSIZE)) (- *DIVSIZE)))
  (setq lr (horAdd (vertAdd point (- *DIVSIZE)) *DIVSIZE))
  (m:draw (list ul ur lr ll)))


(princ "\n mdrdev loaded")
```

A.2.4 Area calculation code library

This code library contains procedures that are modified versions of the procedures in the device drawing code library. They are run after all of the devices are drawn and their function is to calculate the total area in cm^2 of the clear part of the mask for each device. These numbers represent the electrode area which is used for poling the devices.

```
;;; routines to find area for gratings, contact pads, contact strips;
;;; and any other finnishing tasks

;; draw outer contact pads
;; for device mask if flag is 0,
;; for contact pad mask if flag is 1
(defun ma:pads (flag / indx devList devWidth devLength orient origin pads)
  (setq indx 0)
  (while (< indx (length *DEVICES))
    (setq devList (nth indx *DEVICES))
    (setq devWidth (getDevWidth devList))
    (setq devLength (getDevLength devList))
    (setq origin (getOrigin devList))
    (setq orient (getOrient devList))
    (cond ((and (= orient 0) (= flag 0))
   (setq pads (find00 origin devLength devWidth)))
  ((and (= orient 1) (= flag 0))
   (setq pads (find10 origin devLength devWidth)))
```

```
  ((and (= orient 0) (= flag 1))
   (setq pads (find01 origin devLength devWidth)))
    ((and (= orient 1) (= flag 1))
     (setq pads (find11 origin devLength devWidth))))
    (if (= flag 0)
(areaAdd indx (padsArea pads)))
    (setq indx (1+ indx)))
  (prin1))

;; draw inner contact strips and gratings
(defun ma:gratings ( / indx1 indx2 devList grts devLength origin orient
   grt width period spread topL topR bottomL bottomR)
  (setq indx1 0)
  (while (< indx1 (length *DEVICES))
    (print (list "...adding device" (1+ indx1)))
    (setq devList (nth indx1 *DEVICES))
    (setq grts (getGrts devList))
    (setq devLength (getDevLength devList))
    (setq origin (getOrigin devList))
    (setq orient (getOrient devList))
    (cond ((= orient 0)
   (setq bottomL origin
 topL (vertAdd origin devLength)))
  ((= orient 1)
   (setq bottomL origin
 bottomR (horAdd origin devLength))))
    (setq indx2 0)
    (while (< indx2 (length grts))
      (setq grt (nth indx2 grts))
      (setq width (getGrWidth grt))
      (setq period (getPeriod grt))
      (setq spread (getSpread grt))
      (cond ((= orient 0)
     (setq bottomR (horAdd bottomL width)
   topR (horAdd topL width)))
    ((= orient 1)
     (setq topL (vertAdd bottomL width)
   topR (vertAdd bottomR width))))
       (a:drawGrt indx1 topL topR bottomL bottomR period spread orient)
      (if (< indx2 (1- (length grts)))
  (a:drawStrip indx1 topL topR bottomL bottomR orient))
      (cond ((= orient 0)
     (setq bottomL bottomR
   topL topR))
    ((= orient 1)
```

```
     (setq bottomL topL
   bottomR topR)))
      (setq indx2 (1+ indx2)))
    (setq indx1 (1+ indx1)))
  (prin1))

(defun ma:finnish ( / indx devList)
  (setq indx 0)
  (while (< indx (length *DEVICES))
    (print (* 1e-8 (cadr (assoc indx *AREAS))))
    (setq indx (1+ indx))))


%%%%%%%%%%
% other procedures that would have invoked the m:draw procedure:
% a:drawGrt, a:drawStrip
%%%%%%%%%%

(defun a:drawGrt (devNum topL topR bottomL bottomR period spread orient)
  (if (listp period)
      (if (= (length period) 3)
     (a:drawDouble devNum topL topR bottomL bottomR period spread orient)
  (a:drawSingle devNum topL topR bottomL bottomR period spread orient))
      (a:drawSingle devNum topL topR bottomL bottomR period spread orient)))

(defun a:drawSingle (devNum topL topR bottomL bottomR period spread orient /
 period0 offset spaceLeft current verts vertices vArea)
  (setq period0 (nth 0 (getPerOff period)))
  (setq offset (nth 1 (getPerOff period)))
  (cond ((= orient 0)
 (setq spaceLeft (- (cdr topL) (cdr bottomL)))
 (setq current (cdr bottomL))
 (while (> spaceLeft period0)
   (setq verts (findVerts offset 0 (car bottomL) (car bottomR)
    current period0 spread))
   (setq vertices (nth 0 verts)
 vArea (nth 1 verts))
   (areaAdd devNum vArea)
   (setq spaceLeft (- spaceLeft period0))
   (setq current (+ current period0))))
((= orient 1)
 (setq spaceLeft (- (car topR) (car topL)))
 (setq current (car topL))
 (while (> spaceLeft period0)
   (setq verts (findVerts offset 1 (cdr bottomL) (cdr topL)
```

```
    current period0 spread))
   (setq vertices (nth 0 verts)
 vArea (nth 1 verts))
   (areaAdd devNum vArea)
   (setq spaceLeft (- spaceLeft period0))
   (setq current (+ current period0))))))

(defun a:drawDouble (devNum topL topR bottomL bottomR period spread orient /
 offset1 offset2 spaceLeft current verts vertices vArea
 period1 period2 spread1 spread2 Pratio)
  (setq period1 (nth 0 (getPerOff (nth 0 period)))
   period2 (nth 0 (getPerOff (nth 1 period)))
offset1 (nth 1 (getPerOff (nth 0 period)))
offset2 (nth 1 (getPerOff (nth 1 period)))
spread1 (nth 0 spread)
spread2 (nth 1 spread)
Pratio (nth 2 period))
  (cond ((= orient 0)
 (setq spaceLeft (* (- (cdr topL) (cdr bottomL)) Pratio))
 (setq current (cdr bottomL))
 (while (> spaceLeft period1)
   (setq verts (findVerts offset1 0 (car bottomL) (car bottomR)
    current period1 spread1))
   (setq vertices (nth 0 verts)
 vArea (nth 1 verts))
   (areaAdd devNum vArea)
   (setq spaceLeft (- spaceLeft period1))
   (setq current (+ current period1)))
 (setq spaceLeft (- (cdr topL) current))
 (divMark devNum current)
 (while (> spaceLeft period2)
   (setq verts (findVerts offset2 0 (car bottomL) (car bottomR)
    current period2 spread2))
   (setq vertices (nth 0 verts)
 vArea (nth 1 verts))
   (areaAdd devNum vArea)
   (setq spaceLeft (- spaceLeft period2))
   (setq current (+ current period2))))
((= orient 1)
 (setq spaceLeft (* (- (car topR) (car topL)) Pratio))
 (setq current (car topL))
 (while (> spaceLeft period1)
   (setq verts (findVerts offset1 1 (cdr bottomL) (cdr topL)
    current period1 spread1))
   (setq vertices (nth 0 verts)
```

```
 vArea (nth 1 verts))
   (areaAdd devNum vArea)
   (setq spaceLeft (- spaceLeft period1))
   (setq current (+ current period1)))
 (setq spaceLeft (- (car topR) current))
 (divMark devNum current)
 (while (> spaceLeft period2)
   (setq verts (findVerts offset2 1 (cdr bottomL) (cdr topL)
    current period2 spread2))
   (setq vertices (nth 0 verts)
 vArea (nth 1 verts))
   (areaAdd devNum vArea)
   (setq spaceLeft (- spaceLeft period2))
   (setq current (+ current period2))))))

(defun a:drawStrip (devNum topL topR bottomL bottomR orient / vertices)
  (cond ((= orient 0)
 (setq vertices (list (horAdd topR (- (/ *IGS 2)))
    (horAdd topR (/ *IGS 2))
    (horAdd bottomR (/ *IGS 2))
    (horAdd bottomR (- (/ *IGS 2)))))
 (areaAdd devNum (* *IGS (- (cdr topL) (cdr bottomL)))))
((= orient 1)
 (setq vertices (list (vertAdd topL (- (/ *IGS 2)))
    (vertAdd topL (/ *IGS 2))
    (vertAdd topR (/ *IGS 2))
    (vertAdd topR (- (/ *IGS 2)))))
 (areaAdd devNum (* *IGS (- (car topR) (car topL))))))


(princ "\n marea loaded")
```

A.2.5 Auxiliary code library

This code library contains various subroutines that are used for calculations, data structure manipulation, or error handling. One critical subroutine is the one that interfaces with AutoCAD to create the actual data structures that will make up the output DXF file.

```
;;; useful routines which don't access any global variables
```

```
;; stop and produce an error message
(defun err (message)
  (alert message)
  (exit))

;; turn a dotted pair into a list
(defun toList (pair)
  (list (car pair) (cdr pair)))

;; return an association list that is <num> long
;; with all entries set to <val>
(defun alist (val num / idx assoclist tmp)
  (setq idx 1)
  (setq assoclist (list (list 0 val)))
  (while (< idx num)
    (setq assoclist (append assoclist (list (list idx val))))
    (setq idx (1+ idx)))
  (setq tmp assoclist))

;; return the sum of the numerical elements of the list <x>
(defun sum (x / idx output)
  (if (not (listp x))
      (err "warning: argument to sum is not a list"))
  (setq idx 0 output 0.0)
  (while (< idx (length x))
    (setq output (+ output (nth idx x)))
    (setq idx (1+ idx)))
  (+ output 0))

;; return the dotted pair <vec> offset horizontally by <constant>
(defun horAdd (vec constant)
  (cons (+ (car vec) constant) (cdr vec)))

;; return the dotted pair <vec> offset vertically by <constant>
(defun vertAdd (vec constant)
  (cons (car vec) (+ (cdr vec) constant)))

;; draw a polygon from a list of dotted pairs
;; representing sequential vertices
(defun m:draw (vertices / indx vertex)
  (entmake (list '(0 . "POLYLINE")
 '(8 . "LAYERNAME")
 '(66 . 1)
 '(10 0.0 0.0 0.0)
 '(70 . 1)))
```

```
  (setq indx 0)
  (while (< indx (length vertices))
    (setq vertex (nth indx vertices))
    (if (or (> (- (* 10 (car vertex))
       (fix (+ 0.0001 (* 10 (car vertex))))) 0.000001)
     (> (- (* 10 (cdr vertex))
       (fix (+ 0.0001 (* 10 (cdr vertex))))) 0.000001))
(debug vertex))
    (setq vertex (vertAdd (horAdd vertex *HOFFSET) *VOFFSET))
    (entmake (list '(0 . "VERTEX")
   '(8 . "LAYERNAME")
   (list 10 (car vertex) (cdr vertex) 0.0)))
    (setq indx (1+ indx)))
  (entmake '((0 . "SEQEND"))))

;; returns the area of the pads:
(defun padsArea (pads / indx pad total ul ur lr width height)
  (setq total 0.0)
  (setq indx 0)
  (while (< indx 4)
    (setq pad (nth indx pads))
    (setq ul (nth 0 pad)
  ur (nth 1 pad)
  lr (nth 2 pad))
    (setq width (- (car ur) (car ul))
  height (- (cdr ur) (cdr lr)))
    (setq total (+ total (* width height)))
    (setq indx (1+ indx)))
  (setq total (+ total 0.0)))

(defun debug (vertex / x y)
  (setq x (car vertex)
y (cdr vertex))
  (print x)
  (print y)
  (err "warning: there will be grid snapping"))

(princ "\n mutils loaded")
```

Bibliography

[1] I. Newton. *Opticks.* 1704.

[2] A. L. Schawlow and C. H. Townes. Infrared and optical masers. *Physical Review,* **112,** *1940–1949*, 1958.

[3] P. A. Franken, A. E. Hill, C. W. Peters, and G. Weinreich. Generation of optical harmonics. *Physical Review Letters,* **7,** *118–119*, 1961.

[4] M. Bass, P. A. Franken, A. E. Hill, C. W. Peters, and G. Weinreich. Optical mixing. *Physical Review Letters,* **8,** *18*, 1962.

[5] J. A. Giordmaine. Mixing of light beams in crystals. *Physical Review Letters,* **8,** *19–20*, 1962.

[6] P. D. Maker, R. W. Terhune, M. Nisenoff, and C. M. Savage. Effects of dispersion and focusing on the production of optical harmonics. *Physical Review Letters,* **8,** *21–22*, 1962.

[7] J. A. Armstrong, N. Bloembergen, J. Ducuing, and P. S. Pershan. Interactions between light waves in a nonlinear dielectric. *Physical Review,* **127,** *1918–1939*, 1962.

[8] M. Yamada, N. Nada, M. Saitoh, and K. Watanabe. First-order quasi-phase matched $LiNbO_3$ waveguide peodically poled by applying an external field for efficient blue second-harmonic generation. *Applied Phyics Letters,* **62,** *435–436*, 1993.

[9] Y. R. Shen. *The Principles of Nonlinear Optics.* Wiley-Interscience, 1984.

[10] M. Tsunekane, S. Kimura, M. Kimura, N. Taguchi, and H. Inaba. Broadband tuning of a continuous-wave, doubly resonant, lithium triborate optical parametric oscillator from 791 to 1620 nm. *Applied Optics,* **37,** *6459–6462,* 1998.

[11] P. E. Powers, T. J. Kulp, and S. E. Bisson. Continuous tuning of a continuous-wave periodically poled lithium niobate optical parametric oscillator by use of a fan-out grating design. *Optics Letters,* **23,** *159–161,* 1998.

[12] E. V. Kovalchuk, D. Dekorsy, A. I. Lvovsky, C. Braxmaier, J. Mlynek, A. Peters, and S. Schiller. High-resolution Doppler-free molecular spectroscopy with a continuous-wave optical parametric oscillator. *Optics Letters,* **26,** *1430–1432,* 2001.

[13] M. Bode, P. K. Lam, I. Freitag, A. Tünnermann, H.-A. Bachor, and H. Welling. Continuously-tunable doubly resonant optical parametric oscillator. *Optics Communications,* **148,** *117–121,* 1998.

[14] D. Lee and N. C. Wong. Tuning characteristics of a cw dual-cavity KTP optical parametric oscillator. *Applied Physics B,* **66,** *133–143,* 1998.

[15] D. Lee and N. C. Wong. Tunable optical frequency division using a phase-locked optical parametric oscillator. *Optics Letters,* **17,** *13–15,* 1992.

[16] T. Ikegami, S. Slyusarev, S. Ohshima, and E. Sakuma. Accuracy of an optical parametric oscillator as an optical frequency divider. *Optics Communications,* **127,** *69–72,* 1996.

[17] N. C. Wong. Optical-to-microwave frequency chain utilizing a two-laser-based optical parametric oscillator network. *Applied Physics B,* **61,** *143–149,* 1995.

[18] J. Hall, Jun Ye, S. Diddams, L.-S. Ma, S. T. Cundiff, and D. J. Jones. Ultrasensitive spectroscopy, the ultrastable lasers, the ultrafst lasers, and the seriously

nonlinear fiber: A new alliance for physics and metrology. *IEEE Journal of Quantum Electronics,* **37,** *1482–1492*, 2001.

[19] R. Holzwarth, M. Zimmermann, T. Udem, and T. W. Hansch. Optical clockworks and the measurement of laser frequencies with a mode-locked frequency comb. *IEEE Journal of Quantum Electronics,* **37,** *1493–1501*, 2001.

[20] R. Graham and H. Haken. The quantum fluctuations of the optical parametric oscillator I. *Z. Phys.,* **210,** *276*, 1968.

[21] D. Lee and N. C. Wong. Stabilization and tuning of a doubly resonant optical parametric oscillator. *Journal of the Optical Society of America B,* **10,** *1659–1667*, 1993.

[22] C. D. Nabors, S. T. Yang, T. Day, and R. L. Byer. Coherence properties of a doubly resonant monolithic optical parametric oscillator. *Journal of the Optical Society of America B,* **7,** *815–820*, 1990.

[23] E. J. Mason and N. C. Wong. Observation of two distinct phase states in a self-phase-locked type II phase-matched optical parametric oscillator. *Optics Letters,* **23,** *1733–1735*, 1998.

[24] C. Fabre, E. J. Mason, and N. C. Wong. Theoretical analysis of self-phase locking in a type II phase-matched optical parametric oscillator. *Optics Communications,* **170,** *299–307*, 1999.

[25] D.-H. Lee, M. E. Klein, J.-P. Meyn, P. Groβ, R. Wallenstein, and K.-J. Boller. Self-injection-locking of a cw-OPO by intracavity frequency-doubling the idler wave. *Optics Express,* **5,** *114–119*, 1999.

[26] J.-J. Zondy and A. Douillet. Theory of self-phase-locked optical parametric oscillators. *Physical Review A,* **63,** *023814*, 2001.

[27] Z. Y. Ou, S. F. Pereira, H. J. Kimble, and K. C. Peng. Realization of the Einstein-Podolsky-Rosen paradox for continuous variables. *Physical Review Letters,* **68,** *3663–3666*, 1992.

[28] http://kerr.physik.uni-erlangen.de/quicov/.

[29] C. H. Bennett, G. Brassard, C. Cr'epeau, R. Jozsa, A. Peres, and W. K. Wootters. Teleporting an unknown quantum state via dual classical and Einstein-Podolsky-Rosen channels. *Physical Review Letters,* **70,** *1895–1899*, 1993.

[30] P. G. Kwiat, E. Waks, A. G. White, I. Appelbaum, and P. H. Eberhard. Ultrabright source of polarization-entangled photons. *Physical Review A,* **60,** *R773–R776*, 1999.

[31] M. Oberparleiter and H. Weinfurter. Cavity-enhanced generation of polarization-entangled photon pairs. *Optics Communications,* **183,** *133–137*, 2000.

[32] J. H. Shapiro. *Long-distance high-fidelity teleportation using singlet states*, volume 3 of *Quantum Communication, Measurement, and Computing*, pages 367–374. Kluwer, New York, NY, 2001.

[33] S. Lloyd, M. S. Shahriar, J. H. Shapiro, and P. R. Hemmer. Long distance, unconditional teleportation of atomic states via complete Bell state measurements. *Physics Review Letters,* **87,** *167903*, 2001.

[34] J. H. Shapiro and N. C Wong. An ultrabright narrowband source of polarization-entangled photon pairs. *J. Opt. B: Quantum Semiclass. Opt.,* **2,** *L1–L4*, 2000.

[35] K. Sanaka, K. Kawahara, and T. Kuga. New high-efficiency source of photon pairs for engineering quantum entanglement. *Physical Review Letters,* **86,** *5620–5623*, 2001.

[36] S. Tanzilli, H. De Riedmatten, W. Tittel, H. Zbinden, P. Baldi, M. De Micheli, D. B. Ostrowsky, and N. Gisin. Highly efficient photon-pair source using periodically poled lithium niobate waveguide. *Electronics Letters,* **37,** *26–28*, 2001.

[37] S. C. Buchter, T. Y. Fan, V. Liberman, J. J. Zayhowski, M. Rothschild, E. J. Mason, A. Cassanho, H. P. Jenssen, and J. H. Burnett. Periodically poled $BaMgF_4$ for ultraviolet frequency generation. *Optics Letters,* **26,** *1693–1695*, 2001.

[38] C. Fabre, P. F. Cohadon, and C. Schwob. CW optical parametric oscillators: single mode operation and frequency tuning properties. *Quantum Semiclass. Opt.*, **9**, *165–172*, 1997.

[39] J. Y. Courtois, A. Smith, C. Fabre, and S. Reynaud. Phase diffusion and quantum noise in the optical parametric oscillator: a semiclassical approach. *Journal of Modern Optics,* **38**, *177-191*, 1991.

[40] K. C. Rustagi, S. C. Mehendale, and S. Meenakshi. Optical frequency conversion in quasi-phase-matched stacks of nonlinear crystals. *IEEE Journal of Quantum Electronics,* **QE-18**, *1029–1041*, 1982.

[41] M. M. Fejer, G. A. Magel, D. H. Jundt, and R. L. Byer. Quasi-phase-matched second harmonic generation: Tuning and tolerances. *IEEE Journal of Quantum Electronics,* **28**, *2631–2653*, 1992.

[42] W. K. Burns, W. McElhanon, and L. Goldberg. Second harmonic generation in field poled, quasi-phase-matched, bulk $LiNbO_3$. *IEEE Photonics Technology Letters,* **6**, *252–254*, 1994.

[43] J. Webjörn, V. Pruneri, P. St. J. Russell, J. R. M. Barr, and D. C. Hanna. Quasi-phase-matched blue light generation in bulk lithium niobate, electrically poled via periodic liquid electrodes. *Electronics Letters,* **30**, *894–895*, 1994.

[44] Q. Chen and W. P. Risk. Periodic poling of $KTiOPO_4$ using an applied electric field. *Electronics Letters,* **30**, *1516–1517*, 1994.

[45] L. E. Myers, G. D. Miller, R. C. Eckardt, M. M. Fejer, R. L. Byer, and W. R. Bosenberg. Quasi-phasematched 1.064-μm-pumped optical parametric oscillator in bulk periodically poled $LiNbO_3$. *Optics Letters,* **20**, *52–54*, 1995.

[46] L. E. Myers, R. C. Eckardt, M. M. Fejer, R. L. Byer, and W. R. Bosenberg. Multigrating quasi-phase-matched optical parametric oscillator in periodically poled $LiNbO_3$. *Optics Letters,* **21**, *591–593*, 1996.

[47] P. T. Nee and N. C. Wong. Optical frequency division by 3 of 532 nm in periodically poled lithium niobate with a double grating. *Optics Letters,* **23,** *46–48,* 1998.

[48] G. Miller. *Periodically poled lithium niobate: modeling, fabrication, and nonlinear-optical performance.* PhD thesis, Stanford University, 1998.

[49] L. Myers. *Quasi-phasematched optical parametric oscillators in bulk periodically poled lithium niobate.* PhD thesis, Stanford University, 1995.

[50] P. T. Nee. *Optical Frequency Division via Periodically-Poled-$LiNbO_3$-Based Nonlinear Optics.* PhD thesis, Massachusetts Institute of Technology, 1999.

[51] Robert Batchko, private communication.

[52] R. G. Batchko, V. Y. Shur, M. M. Fejer, and R. L. Byer. Backswitch poling in lithium niobate for high-fidelity domain patterning and efficient blue light generation. *Applied Physics Letters,* **75,** *1673–1675,* 1999.

[53] V. Pruneri. *Electric field periodically inverted $LiNbO_3$ for optical frequency conversion.* PhD thesis, University of Southampton, 1996.

[54] J. G. Bergman, G. R. Crane, and H. Guggenheim. Linear and nonlinear optical properties of ferroelectric $BaMg_4$ and $BaZn_4$. *Journal of Applied Physics,* **46,** *4645–4646,* 1975.

[55] M. Eibschütz, H. J. Guggenheim, S. H. Wemple, I. Camlibel, and M. DiDomenico Jr. Ferroelectricity in $BaM^{2+}F_4$. *Physics Letters,* **29A,** *409–410,* 1969.

[56] V. Liberman, M. Rothschild, J. H. C. Sedlacek, R. S. Uttaro, A. K. Bates, and K. Orvek. In C. J. Progler, editor, *Optical Microlithography XIII,* SPIE 4000, page 488, 2000.

[57] J. H. Burnett, R. Gupta, and U. Griesmann. In C. J. Progler, editor, *Optical Microlithography XIII,* SPIE 4000, page 1503, 2000.

[58] C. Kurtsiefer, M. Oberparleiter, and H. Weinfurter. High-efficiency entangled photon pair collection in type-II parametric fluorescence. *Physical Review A,* **64,** *023802,* 2001.

[59] J. Volz, C. Kurtsiefer, and H. Weinfurter. Compact all-solid-state source of polarization-entangled photon pairs. *Applied Physics Letters,* **79,** *869–871,* 2001.

[60] G. J. Edwards and M. Lawrence. A temperature-dependent dispersion equation for congruently grown lithium niobate. *Optical and Quantum Electronics,* **16,** *373–374,* 1998.

[61] M. Albota. Single-photon detection of 1.55 μm entangled light and frequency upconversion in periodically poled lithium niobate for quantum communication. Master's thesis, Massachusetts Institute of Technology, 2002.

[62] Friedrich Koenig, private communication.

[63] D. C. Hanna. Introduction to $\chi^{(2)}$ processes. *Quantum Semiclass. Opt.,* **9,** *131–138,* 1997.